SYNTHESES AND CHARACTERIZATION
OF
COMPOSITE ULTRAFINE PARTICLES
BY A LASER-INDUCED GAS-PHASE REACTION METHOD
AND
A RADIO-FREQUENCY PLASMA METHOD

MASAAKI SUZUKI

1985

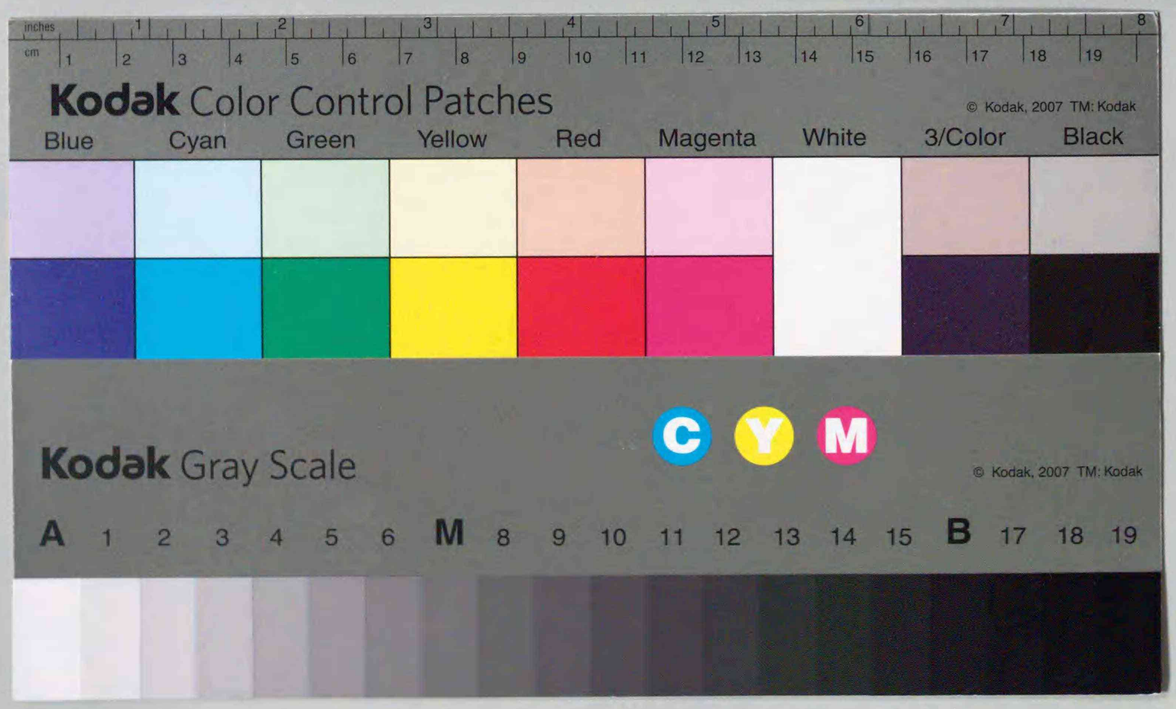

SYNTHESES AND CHARACTERIZATION
OF
COMPOSITE ULTRAFINE PARTICLES
BY A LASER-INDUCED GAS-PHASE REACTION METHOD
AND
A RADIO-FREQUENCY PLASMA METHOD

MASAAKI SUZUKI

1995

CONTENTS

ACKNOWLEDGEMENT

I wish to express my sincerest thanks to Dr. T. Okutani and Mr. Y. Nakata for their invaluable suggestions, instructions and discussions during the period of this work.

I would like to thank Prof. K. Uosaki for his helpful guidance and encouragement as well as acting as a examiner of this thesis. Hearty thanks are made to Prof. T. Yokokawa and Prof. M. Ichikawa and Prof. Y. Nakamura, who acted as examiners of this dissertation, for their helpful and useful suggestion.

Grateful acknowledgement is made to Prof. A. Kato and Prof. J. Hojo for their useful discussions and critical comments.

Thanks are also due to Dr. X.-G. Li and Dr. H. Nagai and Miss. M. Akaike for their technical support and assistance for completing the thesis. I am also thankful to the staffs of Hokkaido National Industrial Research Institute for their support.

Masaaki SUZUKI

Sapporo

December, 1994

CHAPTER 1

INTRODUCTION

CHAPTER 1

INTRODUCTION

1.1 Background of the present work

1.1.1 Advantages of composite ultrafine particles

As a size of solid materials is reduced and reaches to the range of about 1 μm to 1 nm, the number of atoms consisting one particles is reduced and the fraction of the atoms existing on the surface greatly increase. The ultrafine particles with such a small size have been attracting great attentions of many researchers from the viewpoints of fundamental and practical research, as they are chemically active and exhibit different properties from those of the bulk materials. For instance, ultrafine particles are expected to be used as starting powders for ceramics synthesis and catalysts due to their high chemical activities. As mentioned above, ultrafine particles are very interesting materials in aspects of various application, even if they consist of monolithic component. For instance, when we consider to apply ultrafine particles as catalysts, monolithic ultrafine particles such as a nickel particle could exhibit interesting catalytic activity. However, if composite particles such as silica–alumina are used, they have many variations in composition and structure and may be expected some additional effects due to the composite structure. The composite ultrafine particles can be extensively applied in many fields. In addition, when we use ultrafine particles as catalysts, it is necessary to support them on some stable materials, because the fine particles catalysts are very active and are easily sintered. Composite fine particles of catalysts and support materials may be advantageous for stabilizing fine particle catalysts.

In the field of ceramics, ultrafine particles are expected to be used as starting powders for sintering, since they are easily sintered due to their high surface energy. In this field, ceramics products are usually fabricated by making the molding from

starting ceramics powders and subsequently by sintering the molding. In the case of highly heat resistant ceramics such as silicon carbide (SiC) and silicon nitride (Si_3N_4), they are difficult to sinter, since they exhibit covalent bond natures. In general, some sintering aids such as alumina (Al_2O_3) and boron (B) are added when they are sintered. The sintering aids make it easy to sinter, however, they affect on the properties of the final ceramics products and usually make the high temperature strength lower. If we use the surface active ultrafine particles of ceramics, we can sinter them without sintering aids or with a minimum quantity of them and obtained superior heat resistant ceramics as a result. Thus ultrafine particles of ceramics may be effective as starting powders of ceramics products.

Recently it was found that the nano-composite ceramics may have better properties than monolithic ceramics. For instance, the alumina - silicon carbide composite ceramics, in which nano-meter-sized silicon carbide particles are dispersed in the alumina matrix, exhibits superior high temperature mechanical properties than alumina matrix alone [1]. Most nano-composite ceramics are fabricated by sintering the molding made of powder mixture of nano-size powder and matrix powder. In this case, the properties of the produced nano-composite ceramics would be greatly affected by the homogeneity of the mixed powders. If we used the composite fine powders as the starting powders, it is expected to be more favorable suitable for the fabrication of superior nano-composite ceramics, in which nano-size particles are dispersed uniformly in the matrix.

Silicon carbide (SiC) and silicon nitride (Si_3N_4) are well known to have superior properties in high temperature strength. If the composite fine powders of SiC and Si_3N_4 can be synthesized, they are expected to be the excellent starting powders of SiC-Si_3N_4 nano-composite ceramics, which exhibit superior properties than SiC or Si_3N_4 alone. Composite ultrafine particles having composite composition or structure are suitable for the production of high performance materials. Thus, the syntheses of composite ultrafine particles has important significance in applications.

1.1.2 Brief summary of production methods of ultrafine particles

There are many methods to synthesize ultrafine particles. Since it is difficult to make small particles with a size of less than 1 μm by mechanical grainding of bulk materials, ultrafine particles are synthesized generally by physical evaporation of atoms or chemical reactions of molecules (building up process). The building up processes are generally classified into two groups; liquid-phase method and vapor-phase method. The representative methods are listed as follows.

A. Vapor-phase method

A-1. Evaporation method

In these methods, starting bulk materials are heated and evaporated, then the vapor are quenched and condensed to ultrafine particles.

A-1-1. Low pressure evaporation method

Metals are heated and evaporated at low pressure inert atmosphere (1 - 100 Torr, He or Ar), then the metal vapors are condensed to ultrafine particles in gas-phase. The ultrafine particles of almost all the metals and their alloy can be synthesized by this method.

A-2. Vapor-phase reaction method

In this method, ultrafine particles are synthesized by the chemical reaction of metal compound vapor.

A-2-1 Furnace method

In this method, the reaction vessel is heated by the outside electric furnace. It is relatively easy to manipulate and control the process. Ultrafine particles of oxides, carbides and nitrides are synthesized by this method.

A-2-2 Chemical flame method

In this method, particles are synthesized by supplying the metal compound vapor

into chemical flames such as H_2–O_2, or C_xH_y–O_2. Oxide ultrafine particles such as SiO_2, Al_2O_3 and TiO_2 can be synthesized.

A–2–3 Plasma method

In this method, source gases or powders are introduced into the thermal plasmas such as D. C. arc plasma or radio frequency plasma (R.F. plasma). Then, the source materials are heated at the high temperature zone of the plasma. Ultrafine particles are synthesized by evaporation and chemical reaction at high temperature zone of the plasma and subsequently quenching process. Ultrafine particles of metals, oxides, carbides and nitrides are synthesized by this method.

A–2–4 Laser–induced gas–phase reaction method

Reactant gases are irradiated with a laser light and are heated by laser light absorption of the reactant gases themselves. Ultrafine particles are synthesized by decomposition and chemical reaction of the reactants, which are caused by laser light absorption. Ultrafine particles such as SiC, Si_3N_4, Si, TiO_2 and B_4C are derived by this method.

B. Liquid phase method

B–1. Precipitation method

B–1–1. Homogeneous precipitation method

In this method, precipitation reagents are gradually produced in solutions by chemical reactions, then, high purity fine particles are precipitated by formation of homogeneous precipitation reagents. If the production rate of precipitation reagent is sufficiently low, single crystalline particles are derived. Hydroxides of Fe, Al, Sn, Ga, Th and Zr or basic salts are possibly precipitated.

B–1–2. Co–precipitation method

Homogeneous precipitates are produced by adding precipitants into a mixed metallic salts solution. Fine particles are derived subsequently by thermal decomposition of these precipitates. Compound oxides containing more than two

metallic component, such as $BaTiO_3$, can be obtained.

B–1–3. Alkoxides hydrolysis method

In this method, monolithic or compound oxide fine particles are derived by hydrolysis of metal alkoxides (M(OR)n). Most alkoxides are easily purified due to their volatility, and it is not necessary to add any ionic additives during hydrolysis. High purity fine particles can be derived by this method.

B–2. Solvent evaporation method

B–2–1. Freeze drying method

Droplets of metallic salts solution are sprayed onto low temperature liquid such as liquid nitrogen and are instantaneously freezed, then, they are freeze–dried. Fine particles are derived by pyrolysis of the freeze–dried powders. These powders exhibit high surface area, because freezed droplets do not shrink during freeze–drying process.

B–2–2. Spray drying method

A solution is sprayed into a hot air wind of several hundreds Kelvins and dried instantaneously.

B–2–3. Spray thermal decomposition method

A solution is sprayed into a high temperature atmosphere. Then evaporation of the solvent and thermal decomposition of metallic salts occur. Oxides powders are derived in one step by this method.

Most liquid phase methods do not require the large scale facilities or expensive apparatus. The product powders can be easily collected. However, it is extremely difficult to synthesize non–oxide fine particles, such as nitrides and carbides, because most liquid phase method uses hydrolysis reaction of alkoxides and it is difficult to remove oxygen from the solution or the atmosphere.

In Vapor phase methods, rather expensive apparatus, such as vacuum chambers and plasma equipments are needed. However, not only oxides fine particles but also

non–oxide, metal and their composite particles can be synthesized by these methods. For this reason, most carbide and nitride ultrafine particles are synthesized by vapor–phase methods.

Vapor–phase methods are generally classified into two groups; evaporation method and gas–phase reaction method. In evaporation method, source materials are heated and evaporated, then they are quenched and condense to ultrafine particles. Particles are basically produced by physical processes of evaporation and condensation. This method is suitable especially for the production of metal and alloy particles. Gas–phase reaction methods include also physical heating and quenching process, moreover they take advantage of chemical reaction for production of particles. This method is suitable especially for the production of non–oxide particles.

1.1.3 Characteristic of laser–induced gas–phase reaction method and R. F. plasma method

There are four representative methods in gas–phase reaction methods as mentioned above. In furnace method, relatively simple equipments are used and the process is easy to control among those methods. The problems are contamination from the reactor wall and reactions between reactant gases and reactor wall, since the reaction vessel are heated by the outside electric furnace. In addition, the maximum reaction temperature can be around 2000 K.

In chemical flame method, particles are synthesized by supplying metal compound vapor to the high temperature chemical flame, such as H_2–O_2 flame. In this case, the chemical flame does not contact directly with the reactor wall, and the reactor wall is kept relatively low temperature, so contamination from the reactor wall could be suppressed. Metallic ultrafine particles, such as W and Mo are synthesized by reduction of metallic fluoride using a reductive flame, such as H_2–F_2 flame. However, most particles produced by this method are limited to only oxides, and

nitride and carbide particles cannot be produced.

In plasma method usually two kinds of plasma, D.C. arc and R. F. plasma are used, and both plasma can generate extremely high temperature around several thousand Kelvins. Ultrafine particles are produced by supplying source materials to the high temperature zone. D. C. plasma is stable, but contamination of impurities from electrodes may occur, because electrodes are placed in the reaction vessel. On the contrary, R. F. plasma is relatively unstable and weak at disturbance, such as injection of solid materials. But, in the case of R. F. plasma, contamination of impurities from electrodes does not occur, because R. F. plasma can be generated by non–electrode discharge and plasma flame does not contact directly with the reaction vessel. Moreover it has many characteristic features as follows;

(1) The size of R. F. plasma flame is larger compared to D. C. plasma.
(2) The gas velocities can be kept low and residence time of reactant at high temperature zone can be made longer compared to D. C. plasmas.
(3) Oxidative, reductive and corrosive atmospheres are available and it is possible to produce oxide, nitride and carbide particles.

In laser–induced gas–phase reaction method, ultrafine particles are synthesized by chemical reactions, which are caused by irradiating with a laser light to reactant gases having absorption to the wavelength of the laser. Since only reactant gases are heated by the irradiation with a laser light, this method have several advantages as follows;

(1) Since the reaction vessel remains at low temperature, contamination of impurities from the reaction vessel wall does not occur.
(2) Reactions occur within a restricted area and reaction process is uniform.
(3) Because of the easy operation of the laser beam, the synthesis conditions are controlled precisely and reproducibly.
(4) It can be a very fast heating and cooling process under a certain condition.

In laser–induced gas–phase reaction method, at least one reactant gas must absorb laser light, so a kind of reactant gases are restricted. In most cases, CO_2 laser is used in this method, because high output power is derived and energy efficiency is high. As a reactant gas, monosilane (SiH_4) is used in many cases since it strongly absorbs CO_2 laser light. Ultrafine particles of Si, SiC, Si_3N_4, TiO_2, B_4C etc, are synthesized by this method.

As mentioned above, there are many kind of method to synthesize ultrafine particles. From the view point of synthesis of composite ultrafine particles, only oxide composite particles can be synthesized by liquid phase methods. In vapor–phase methods, non–oxide particles as well as oxide can be synthesized. Vapor–phase methods can be applied in various materials and more suitable to produce composite particles than liquid–phase methods.

Among vapor–phase methods, laser–induced gas–phase reaction method is suitable for production of composite ultrafine particles, since it has many advantages as mentioned above, even though reactant gases available are restricted to those having absorption of laser light. Moreover, production of ultrafine particles by laser is relatively new method and was started by Haggerty et al. [2,3] at the beginning of the 1980s. At the present time, $Fe_xSi_yC_z$ composite ultrafine particles were synthesized from $SiH_4/C_2H_4/Fe(CO)_5$ [4] and SiC–Si_3N_4 composite ultrafine particles were synthesized from $(Me_3Si)_2NH$ [5–7] or from SiH_4/CH_3NH_2 [8] or from $SiH_4/CH_3NH_2/NH_3$ [9] by laser–induced gas–phase reaction. They showed that it was possible to synthesize composite ultrafine particles by laser–induced gas–phase reaction method, but no precise investigation has been reported regarding the structure of composite particles.

1.1.4 Structural analysis of composite ultrafine particles

It is very important to study the structure of composite ultrafine particles for the synthesis and application of fine particles, because the properties and functions of

composite fine particles strongly depend on the structure.

Recently, the MAS–NMR is finding new applications in solid inorganic systems such as silicate and zeolite [10]. In addition, this technique is also useful for the study of non–oxide materials [11,12]. In last few years, a number of NMR investigations about the structure of SiC and Si_3N_4 have been reported. Most of them were concerned with well–known structures such as α– and β–SiC and α– and β–Si_3N_4 and their polytypes. [11–19]. These investigations revealed that different Si configurations in the crystals can be clearly distinguished by ^{29}Si–MAS–NMR, since it is very sensitive to the local structure around Si atom. Even though there are a few NMR studies about practical commercial powders, they showed that information about the crystallinity and defects of the powders can be obtained by MAS–NMR at some extent. In the case of inorganic solid it is rather difficult to get standard inorganic materials for solid NMR and the solid NMR spectra are sometimes broadened by their poor crystallinity or defects, which make their analysis somewhat complex. However, information about the local structure, which cannot be obtained by other method, can be obtained by MAS–NMR. It is expected to be more important method for structural analysis of ceramics ultrafine particles in future.

ESR also provides the information about the local structure, even though the object of study is limited to paramagnetic defects. There are few ESR study of ceramics, because conventional ceramics usually contain much paramagnetic impurities such as Fe and Mn, which contaminate during the process such as grainding. In addition, most ceramic materials is not transparent like glass or single crystalline materials, therefore ceramics is not so interesting in optical applications than glasses or single crystals. At the present there are many ESR studies on CVD Si_3N_4 films for integrated circuit, but, ESR studies on Si_3N_4 powders and SiC are still few. In the field of ceramics, the purity of ceramics are getting higher using highly pure powders to improve the properties. ESR is expected to become important method for the characterization of ceramics in near future.

1.2 Objectives and outline of the present work

In this research, the syntheses of composite ultrafine particles by laser–induced gas–phase reaction method and plasma method were studied. In laser–induced gas–phase reaction method, the syntheses of silicon carbide (SiC) and silicon carbide – silicon nitride composite ultrafine particles ($SiC–Si_3N_4$) were studied. The syntheses of SiC particles were studied as the first stage of the study on the syntheses conditions of composite ultrafine particles. The $SiC–Si_3N_4$ composite ultrafine particles were chosen, because they are expected as superior starting powders for ceramics composites. The $SiC–Si_3N_4$ composite ultrafine particles were syhthesized and their structures were studied in order to study what composite particles could be synthesized by laser–induced gas–phase reaction method.

R. F. plasma method is also suitable for the production of non–oxide or oxide composite ultrafine particles, since it provides interesting conditions such as ultrahigh temperature for reactions. Such a unique condition may result in unique structure or property of the composite particles. The syntheses of $SiC–Si_3N_4$ composite ultrafine particles by R. F. plasma were studied in this research. Moreover, the syntheses of silica–alumina ($SiO_2 \cdot Al_2O_3$) ultrafine particles by plasma method and its catalytic activity were studied as a fundamental study on the catalytic application of ultrafine particles.

The structure and composition of the particles are very important in application of the particles, and especially in the case of composite particles their composite structure greatly affect on their properties. In this research the structure and composition of the composite particles were studied by usual method such as X–ray diffraction (XRD), transmission electron microscope (TEM) and X–ray photoelectron spectroscopy (XPS). Moreover, the local structure of $SiC–Si_3N_4$ particles were studied by magic angle spinning nuclear magnetic resonance spectroscopy (MAS–NMR) and electron spin resonance spectroscopy (ESR) to clarify the local structure of composite

particles.

The outline of the present thesis is as follows.

Chapter 2 describes the syntheses of SiC ultrafine particles using a CO_2 laser as a first stage of the study on the synthesis conditions of composite particles. SiC particles were synthesized from dichlorosilane (SiH_2Cl_2) and monosilane (SiH_4). The difference of synthesis processes between SiH_2Cl_2 and SiH_4 was considered thermodynamically.

Chapter 3 describes the syntheses of $SiC–Si_3N_4$ composite ultrafine particles using CO_2 laser. $SiC–Si_3N_4$ composite particles were synthesized from SiH_4, C_2H_4, NH_3 gases and their structures were studied by XRD, TEM and XPS. It was found that the composite powders were not the simple mixture of SiC and Si_3N_4.

In Chapter 4, the local structure of $SiC–Si_3N_4$ composite particles were studied by $^{29}Si–MAS–NMR$ and ESR.

Chapter 5 describes the synthesis of $SiC–Si_3N_4$ composite particles by R.F. plasma. The structure of composite particles produced by the plasma were studied by $^{29}Si–MAS–NMR$.

In chapter 6, The syntheses of silica–alumina ultrafine particles by a R. F. plasma were studied. The catalytic activity of the particles was investigated as a model case of catalytic application of ultrafine particles.

Finally, **Chapter 7** summarizes the present results.

REFERENCES

1. K. Niihara, " New Design Concept of Structural Ceramics – Ceramics Nanocomposites–", J. Ceram. Soc. Jpn., 99(10) 947–982 (1991)
2. W. R. Cannon, S. C. Danforth, J. H. Haggerty and R. A. Marra, "Sinterable Ceramic Powders from Laser–driven Reactions: 1, Process description and Modeling" J. Am. Ceram. Soc., 65 324 (1982)
3. W. R. Cannon, S. C. Danforth, J. H. Haggerty and R. A. Marra, "Sinterable Ceramic Powders from Laser–driven Reactions: 2, Powder characteristics and Process Variables", J. Am. Ceram. Soc., 65 330 (1982)
4. A. Gupta, J. T. Yardley,"Production of Light Olefins from Synthesis Gas using Catalysts prepared by Laser Pyrolysis" SPIE, Vol.458, "Applications of Lasers to Industrial Chemistry" (1984) pp131–39
5. G. W. Rice and R. L. Woodin,"Laser Synthesis of Powders from Large Molecules" SPIE, Vol.458 "Applications of Lasers to Industrial Chemistry" (1984) pp98–107
6. G. W. Rice,"Laser Synthesis of Si/C/N Powders from 1,1,1,3,3,3–Hexamethyldisilazane" J. Am. Ceram. Soc., 69, C183–85 (1986)
7. G. W. Rice, "Laser Synthesis of Powders", "Adv. in Ceramics" Vol.21, Am. Ceram. Soc., (1987) pp229–36
8. R. Alexandrescu, I. Morjan, E. Borsella, S. Botti, R. Fantoni, T. Dikonimos–Makris, R. Giorge and S. Enzo,"Composite Ceramic Powders obtained by Laser Induced Reactions of Silane and Amines" J. Mater. Res., 6(11) 2442–51 (1991)
9. M. Cauchetier, O. Croix, M. Luce, M. I. Baraton, T. Merle and P. Quinted,"Nanometric Si/C/N Composite Powders: Laser Synthesis and IR Characterization" J. European Ceram. Soc., 8, 215–19 (1991)
10. E. Oldfield and R. J. Kirkpatrick, "High–Resolution Nuclear Magnetic Resonance of Inorganic Solids", Science, 227, 1537–44 (1985)
11. G. R. Hatfield and K. R. Carduner, "Review, Solid State NMR: Applications in High Performance Ceramics.", J. Mater. Sci., 24, 4209–19 (1989)

12. G. L. Turner, R. J. Kirkpatrick, S. H. Risbud and E. Oldfield, "Multinuclear Magic–Angle Sample–Spinning Nuclear Magnetic Resonance Spectroscopic Studies of Crystalline and Amorphous Ceramic Materials." Am. Ceram. Soc. Bull., 66(4), 656–63 (1987)
13. D. C. Apperley, R. K. Harris, G. L. Marshall and D. P. Thompson, "Nuclear Magnetic Resonance Studies of Silicon Carbide Polytypes." J. Am. Ceram. Soc., 74(4), 777–82 (1991)
14. K. R. Carduner, R. O. Carter , M. E. Milberg and G. M. Crosbie, "Determination of Phase Composition of Silicon Nitride Powders by Silicon–29 Magic Angle Spinning Nuclear Magnetic Resonance Spectroscopy.", Anal. Chem. 59, 2794–97 (1987)
15. K. R. Carduner, C. S. Blackwell, W. B. Hammond, F. Reidinger and G. R. Hatfield, "^{29}Si NMR Characterization of α– and β –Silicon Nitride.", J. Am. Chem. Soc., 112, 4676–79 (1990)
16. N. R. Dando and M. A. Tadayyoni, "Characterization of Polyphasic Silicon Carbide Using Surface–Enhanced Raman and Nuclear Magnetic Resonance Spectroscopy.", J. Am. Ceram. Soc., 73(8), 2242–46 (1990)
17. G. R. Finlay, J. S. Hartman, M. F. Richardson and B. L. Williams, "^{29}Si and ^{13}C Magic Angle Spinning N.M.R. Spectra of Silicon Carbide Polymorphs.", J. Chem. Soc., Chem. Commun., 1985, 159–61 (1985)
18. J. R. Guth and W. T. Petuskey, "Silicon–29 Magic Angle Sample Spinning Nuclear Magnetic Resonance Characterization of SiC Polytypes.", J. Phys. Chem., 91, 5361–64 (1987)
19. J. S. Hartman, M. F. Richardson, B. L. Sherriff and B. G. Winsborrow, "Magic Angle Spinning NMR Studies of Silicon Carbide: Polytypes, Impurities, and Highly Inefficient Spin–Lattice Relaxation.", J. Am. Chem. Soc., 109, 6059–67 (1987)

CHAPTER 2

SYNTHESES OF SIC ULTRAFINE PARTICLES BY LASER-INDUCED GAS-PHASE REACTION METHOD

CHAPTER 2

SYNTHESES OF SiC ULTRAFINE PARTICLES BY LASER-INDUCED GAS-PHASE REACTION METHOD

2.1. Introduction

The laser-induced gas phase reaction is an excellent method of obtaining ultrafine particles of very pure and uniform in composition and size. Ultrafine particles of Si [1,2], SiC [1-7], Si_3N_4 [1,2,9,10], Si/C/N [11-13], B_4C [14], and Fe/Si/C [15] have been synthesized by laser-induced gas phase reaction. A CO_2 laser [1-5,16] was used in most investigations, while an excimer laser [17] or a YAG laser [18] has been used in some investigations. Most researcher synthesized SiC and Si_3N_4 particles using CO_2 lasers with SiH_4 as the starting material under reduced pressure.

In laser-induced gas phase reaction, reactant gas must absorb laser light. There are a few gaseous Si source absorbing CO_2 laser such as SiH_4 and SiH_2Cl_2. SiH_4 strongly absorbs CO_2 laser light and has only silicon and hydrogen atoms, so it is suitable for the production of highly pure ultrafine particles. However, SiH_4 is expensive and difficult to handle because of its spontaneous ignition in air. The process would be more economical if a compound other than SiH_4 was available as the silicon source and could be reacted at atmospheric pressure. Bauer et al. [16,19] have reported the syntheses of Si and Si_3N_4 powder from SiH_2Cl_2 and $SiCl_4$ which are cheaper and less dangerous than SiH_4.

In this chapter the synthesis of ultrafine SiC particles from SiH_2Cl_2 and C_2H_4 at atmospheric pressure was studied as a first stage of the study on the synthesis of SiC-Si_3N_4 composite particles. In addition, SiC particles were also synthesized from SiH_4 and C_2H_4 to compare their reaction processes. In laser-induced gas-phase reaction method, the gaseous sources were irradiated with laser light and heated up to about 3000 K. The reaction zone was luminous like a flame and that was called "reaction

flame". The absorption of laser light and the decomposition of source gases and production of particles occurred within this restricted area. The behavior of the laser light absorption and the reaction flame temperature is quite important to elucidate the reaction mechanism and to control the reaction during powder synthesis by laser-induced gas-phase reaction. Nevertheless, there are few reports on the behavior of the laser light absorption during powder synthesis. In this research, the relationship between the reaction flame temperature and the extent of laser light absorption was studied and the difference between the behavior of SiH_4-C_2H_4 and that of SiH_2Cl_2-C_2H_4 was considered thermodynamically.

2.2 Experimental procedures

Figure 2.1 shows the schematic diagram of the CO_2 laser reactor. After the reactor had been evacuated, argon gas was introduced. Then, a gas mixture of SiH_2Cl_2 and C_2H_4 or of SiH_4 and C_2H_4 was introduced through a 1 mm i.d. stainless steel pipe and irradiated with a CO_2 laser beam at right angles at atmospheric pressure. The wavelength of the CO_2 laser was 10.6 μm and the maximum laser power was 150 W. The laser beam, diameter of 10 mm, was focused by a ZnSe lens. The laser beam diameter at the reaction zone was changed by varying the distance between the lens and the reaction zone. A beam diameter at the reaction zone of 2 or 4 mm was used in this experiment. The temperature of the reaction flame was measured using a pyroscope having a measurable range from 1273 to 3073 K. In the case of the powder synthesized from SiH_2Cl_2, the powder gave off a strong HCl odor, and was dried at about 373 K for at least 2 h in a nitrogen flow until no odor remained.

The powders were subsequently analyzed by X-ray diffraction (XRD) for the crystalline phase, and by the one-point BET method for the specific surface area. The oxygen content of the powders was determined by N, O analyzer (HORIBA EMGA-550) , and carbon content was determined by coulometry or by C analyzer (HORIBA EMIA-510). Particle morphology and structure were observed by

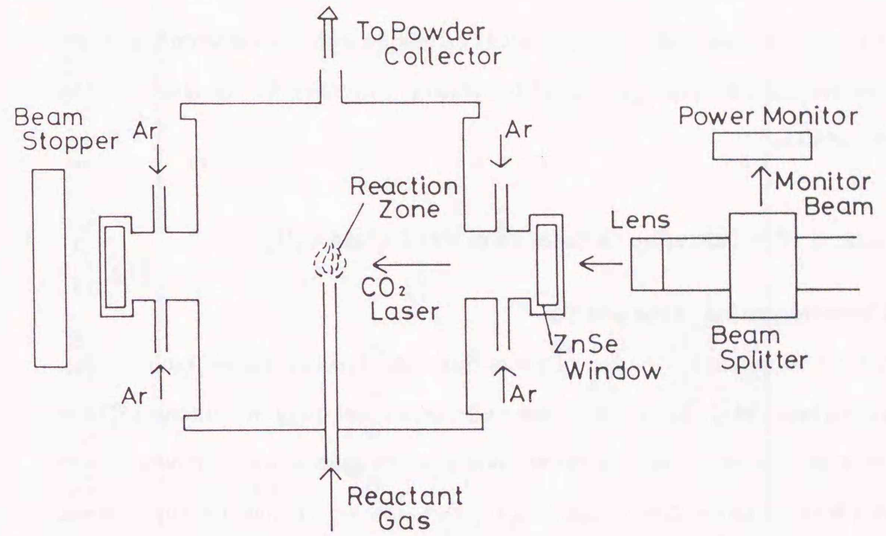

Fig. 2.1 Schematic diagram of CO_2 laser reactor.

transmission electron microscopy (TEM, HITACHI, H800–NA) and selected–area electron diffraction (SAED). The samples for TEM were prepared using a dispersion method. A dilute dispersion of the powder in reagent–grade ethanol was homogenized by an ultrasonic probe. Then a drop of dispersion was placed on a microgrid 3–mm–diameter, followed by drying at room temperature. Chlorine present in the powder as an impurity was determined by atomic absorption analysis indirectly to measure silver. Fourier transform photoacoustic emission (PAS) spectra were taken for several powders using FTS–65 (Bio–Rad). PAS spectra were obtained at a resolution on 4.0 cm^{-1}.

The amount of laser light absorption was estimated from the difference of laser power before and after passage through the reactor, correcting for the absorption by the ZnSe windows.

2.3 Synthesis of SiC ultrafine particles from SiH_2Cl_2 and C_2H_4

2.3.1 Characterization of the powder

Table 2.1 summarizes the reactant gas flow rate, reaction flame temperature, specific surface area, crystalline phase and carbon and oxygen contents. These powders were synthesized at different reactant gas flow rates at a laser power density of 3.66 kW/cm^2. In the case of the SiH_2Cl_2 flow rate of 10 standard cm^3/min (st. cm^3/min), the reaction flame temperature was less than 1273 K at a low C_2H_4/SiH_2Cl_2 flow ratio, but increased rapidly to over 3073 K as the C_2H_4/SiH_2Cl_2 ratio exceeded 0.5. The specific surface area became maximum near C_2H_4/SiH_2Cl_2 = 0.5. TEM observation showed that the particle size of the powder became minimum near C_2H_4/SiH_2Cl_2 = 0.5. The same trend was observed at a SiH_2Cl_2 flow rate of 20 st. cm^3/min. The total carbon content of the powder increased linearly with a rise in the C_2H_4/SiH_2Cl_2. (Fig. 2.2) These powders contained a large amount of oxygen, especially when the powders were synthesized with SiH_2Cl_2 only or at a low C_2H_4/SiH_2Cl_2 ratio. It was thought that these powders oxidized in air because they

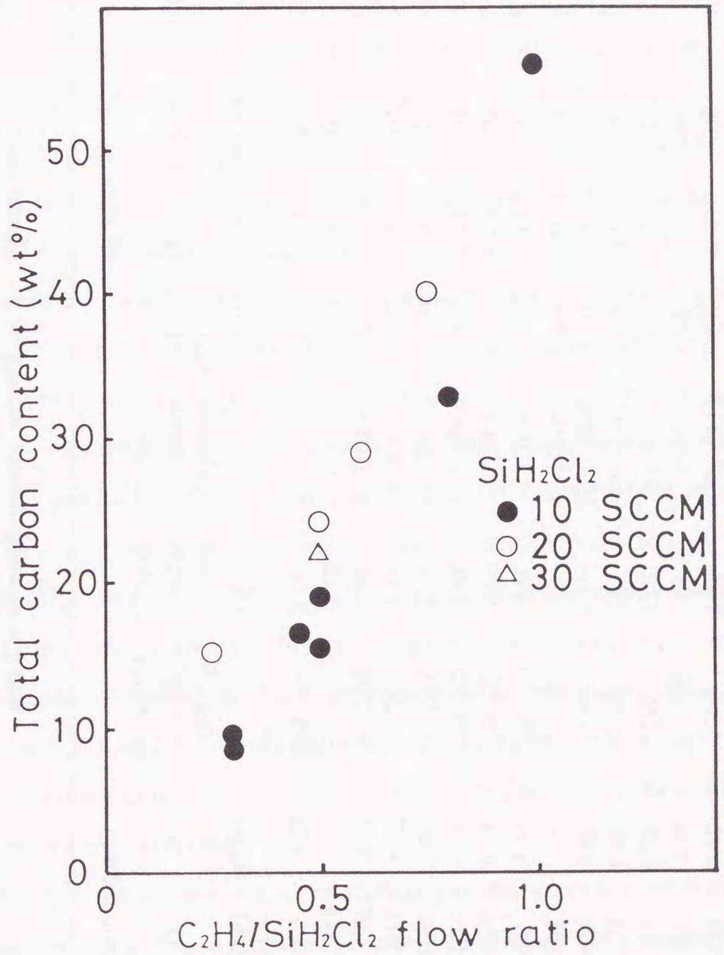

Fig. 2.2 Effect of C_2H_4/SiH_2Cl_2 flow ratio on total carbon content of powder.
SCCM = standard cm^3/min

Table 2.1 Synthesis conditions and properties of the SiC ultrafine powders synthesized using a CO_2 laser with SiH_2Cl_2 and C_2H_4 power density = 3.66 kW/cm^2, beam diameter = 2 mm

Sample no.	Reactant gases			Reaction flame temp.(K)	Specific surface area (m^2/g)	Crystalline phase by XRD	Composition	
	SiH_2Cl_2 (st.cm^3/min)	C_2H_4	C_2H_4/SiH_2Cl_2 ratio				C (wt%)	O (wt%)
1	4	15	3.75	---	57.4	C, SiC	72.4	5.4
2	10	0	0.0	<1273	14.1	Si	--	42.3
3	10	3	0.3	<1273	44.9	SiC, Si	19.2	36.1
4	10	5	0.5	>3073	153.3	SiC	21.5	21.2
5	10	8	0.8	>3073	111.8	SiC, C	32.1	16.7
6	10	10	1.0	>3073	78.1	C, SiC	44.4	14.1
7	10	13	1.3	>3073	67.0	C, SiC	53.0	14.4
8	10	15	1.5	>3073	72.9	C, SiC	56.8	9.6
9	20	0	0.0	<1273	8.6	Si	--	20.0
10	20	5	0.25	2823-2933	104.9	SiC	18.0	24.6
11	20	10	0.5	2573-2693	79.8	SiC	25.7	13.2
12	20	12	0.6	>3073	61.9	SiC	29.3	17.7
13	20	15	0.75	>3073	88.1	SiC, C	36.4	13.4
14	30	15	0.5	2113-2193	86.1	SiC	24.0	19.2

were handled in air. The powders contained a small amount of chlorine: 0.23 wt% in sample 10, 0.26 wt% in sample 11 and 0.24 wt% in sample 13. Based on the results of composition analysis, the amounts of free carbon and SiC were calculated by assuming that the powders consisted of carbon, silicon and oxygen, and oxygen present as SiO_2, and silicon other than SiO_2 present as SiC. The amount of free carbon became minimum (about 5 wt%) near $C_2H_4/SiH_2Cl_2 = 0.5$, which was the stoichiometric ratio for SiC formation. ($SiH_2Cl_2(g) + 1/2C_2H_4 \rightarrow \beta$-SiC(s) + $2HCl(g) + H_2(g)$). Free carbon increased rapidly as the C_2H_4/SiH_2Cl_2 ratio increased. The amount of SiC became maximum (about 70 wt%) near $C_2H_4/SiH_2Cl_2 = 0.5$, and then decreased as C_2H_4/SiH_2Cl_2 increased. These results show that the free carbon formed easily and the amount of free carbon increased as C_2H_4/SiH_2Cl_2 increased.

Figure 2.3 shows the TEM photographs of particles synthesized by using a CO_2 laser. When the powder was synthesized from SiH_2Cl_2 only (Fig. 2.3(A)), the powder consisted of two types of particles; large (0.1 to 0.7 μm) spherical particles and smaller ones agglomerated into secondary particles. With increasing the C_2H_4 flow rate, the particle size decreased to around 0.3 μm at a C_2H_4/SiH_2Cl_2 ratio = 0.3 (Fig. 2.3(B)). Many of these particles were agglomerated strongly to each other. At a C_2H_4/SiH_2Cl_2 ratio = 0.5 (Fig. 2.3(C)), the particles were generally spherical, 0.04 to 0.07 μm in size, although still partly agglomerated. Some of them had radial projections, as shown in the lower left portion of the photograph. At a C_2H_4/SiH_2Cl_2 ratio = 1.3 (Fig. 2.3(D)), the particles were increased in size, and tended to be agglomerated more. Flake-shape particles, in addition to those having radial projections were observed.

Selected area electron diffraction (SAED) patterns were obtained to determine the crystalline phase of each particles. Figure 2.4 shows a TEM photograph and SAED patterns of the particles synthesized with SiH_2Cl_2 only. This powder consisted of two kinds of particle: large spherical particles whose size was in the 0.1 – 0.7 μm range, and smaller particles agglomerated into secondary particles. From the electron

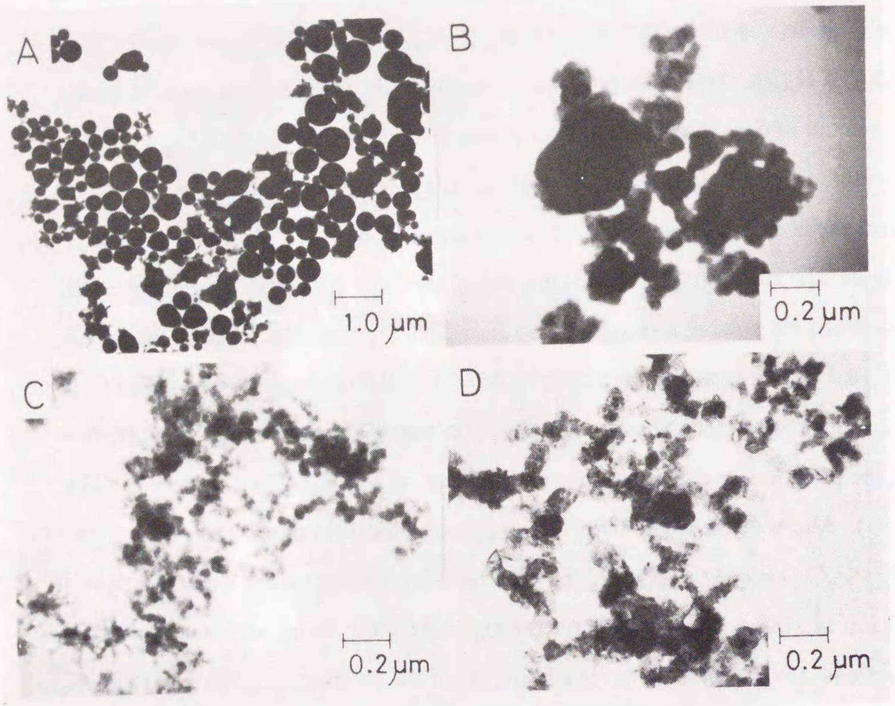

Fig. 2.3 TEM photographs of the particles synthesized using a CO_2 laser from SiH_2Cl_2 and C_2H_4.

(A) SiH_2Cl_2 = 20 standard cm^3/min, C_2H_4 = 0 standard cm^3/min

(B) SiH_2Cl_2 = 10 standard cm^3/min, C_2H_4 = 3 standard cm^3/min

(C) SiH_2Cl_2 = 10 standard cm^3/min, C_2H_4 = 5 standard cm^3/min

(D) SiH_2Cl_2 = 10 standard cm^3/min, C_2H_4 = 13 standard cm^3/min

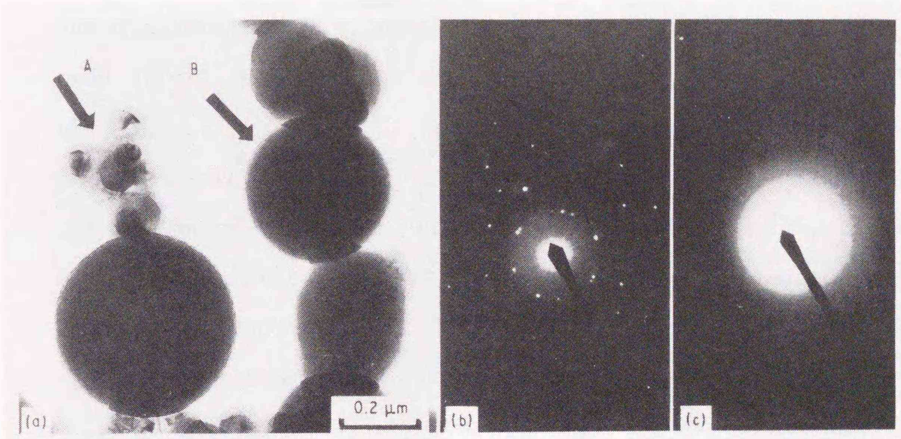

Fig. 2.4 TEM photographs of the particles synthesized using the CO_2 laser with SiH_2Cl_2 = 20 standard cm^3/min, and SAED patterns of part A and B.

diffraction results, it was found that the large spherical particles were amorphous and the smaller agglomerated particles were crystalline silicon.

Figure 2.5 shows TEM photographs and SAED patterns of the various kinds of particles observed in the powders synthesized from a gas mixture of C_2H_4 and SiH_2Cl_2. From the results of TEM observations, the powder synthesized at a low C_2H_4/SiH_2Cl_2 ratio (0.3) consisted of strongly agglomerated particles (Fig. 2.5(a)) with a size of 0.3 μm. The powder synthesized at C_2H_4/SiH_2Cl_2 = 0.5 consisted of basically spherical particles (Fig. 2.5(b)), whose size was in the 0.04–0.07 μm range, and the particles (Fig. 2.5(c)) which had radial projections. The powders at a high C_2H_4/SiH_2Cl_2 ratio (1.3) consisted of particles as in Fig. 2.5(c) and particles as in Fig. 2.5(d) with a shape close to hexagonal, and a film–like material (Fig. 2.5(e)). From the results of SAED, it was found that particles in Fig. 2.5(a) were a mixture of silicon and SiC; particles in Fig. 2.5(b) and (c) were SiC; particles in Fig. 2.5(d) were mostly carbon including a small amount of SiC; and the film–like material (Fig. 2.5(e)) was carbon. The formation mechanism of the particles in Fig 2.5(c) was not clearly understood, but it was speculated that SiH_2Cl_2 or chlorine might play a role in the formation of these particles, because they could not be observed in other SiH_4–C_2H_4 systems [3].

Figure 2.6 shows the typical photoacoustic spectra (PAS) of the powders. SiC (around 800 cm^{-1}) and SiO_2 (around 1100 cm^{-1}) were observed in all the samples. A small peak of the Si–H bond (2150 cm^{-1}) was observed in the powder synthesized with SiH_2Cl_2 = 20 st. cm^3/min and C_2H_4 = 5 st. cm^3/min at a reaction flame temperature of 2823–2933 K.

2.3.2 Reaction mechanism

2.3.2.1 Silicon formation

Silicon particles were produced by irradiating SiH_2Cl_2 with a CO_2 laser. In the case of SiH_2Cl_2 only, the reaction flame temperature was less than 1273 K. In this

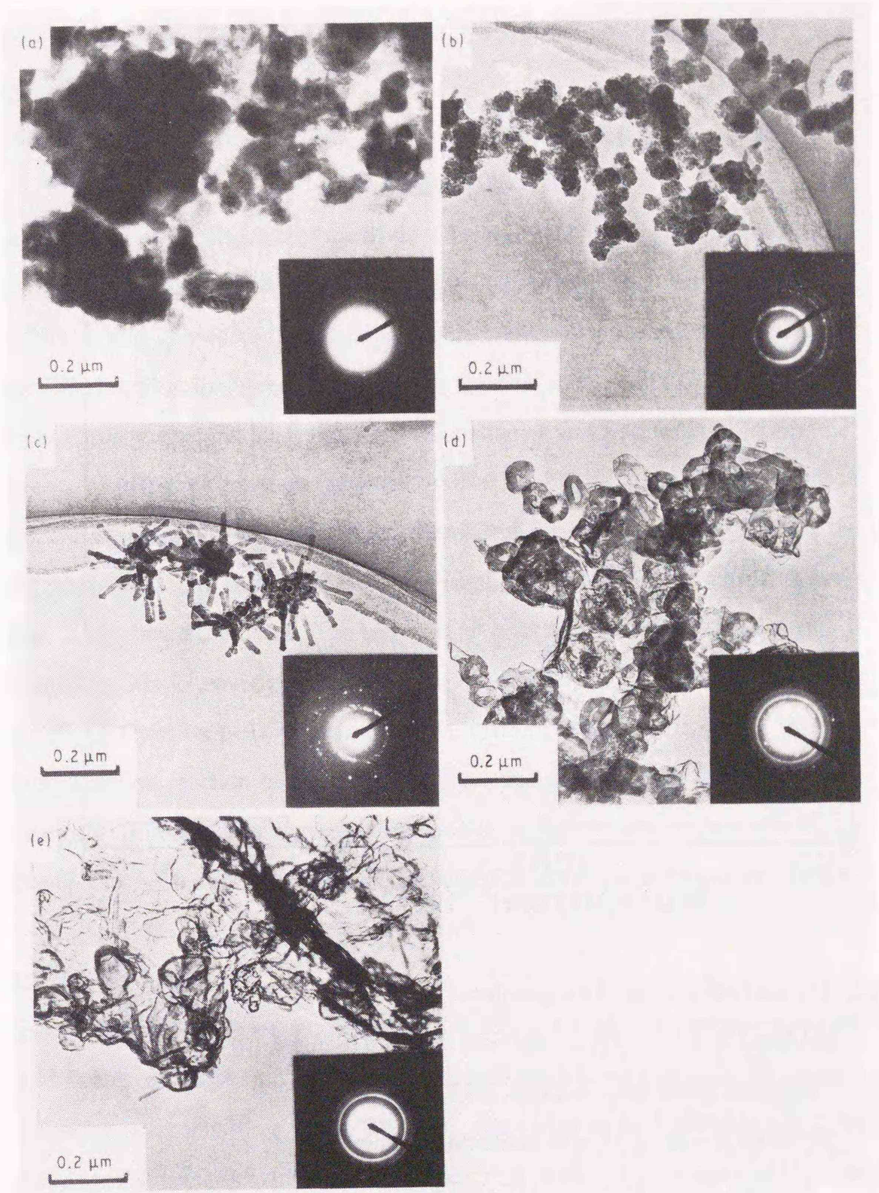

Fig. 2.5 TEM photographs and SAED patterns of the various type of particles observed in the powders synthesized with SiH_2Cl_2 and C_2H_4 using the CO_2 laser.

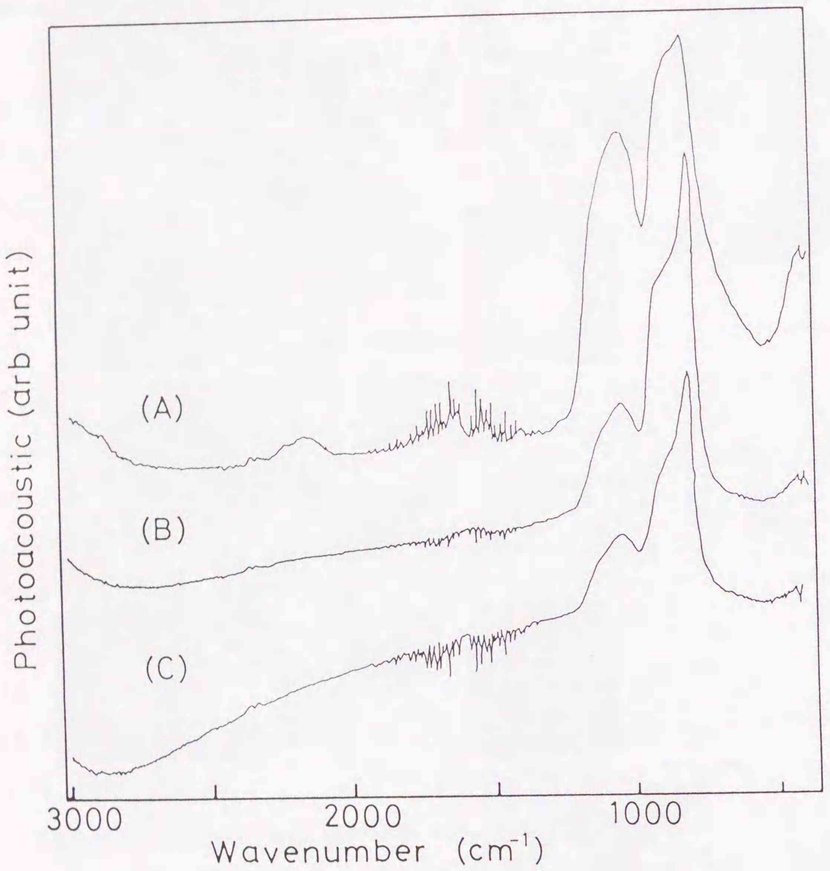

Fig. 2.6 Typical PAS spectra of the powders.

(A) SiH_2Cl_2 = 20, C_2H_4 = 5 standard cm^3/min (Sample 10)

Reaction flame temp. = 2823–2933 K

(B) SiH_2Cl_2 = 20, C_2H_4 = 10 standard cm^3/min (Sample 11)

Reaction flame temp. = 2573–2693 K

(C) SiH_2Cl_2 = 20, C_2H_4 = 15 standard cm^3/min (Sample 13)

Reaction flame temp. = >3073 K

temperature range, silicon particles formation by direct decomposition of SiH_2Cl_2 was difficult because the equilibrium constant of direct decomposition of SiH_2Cl_2 was small.

$$SiH_2Cl_2(g) \rightarrow Si(s) + 2HCl(g),\ \log Kp = 0.237,\ 1300\ K\ [20] \qquad (2.1)$$

$$\Delta H = 135.1\ kJ/mol\ (1300\ K)$$

The equilibrium phase diagram of the Si–H–Cl system [21] shows that $SiCl_4$, $SiHCl_3$, SiH_2Cl_2, $SiHCl_3$, $SiCl_2$, and $SiCl_3$ are present in a gaseous phase below 1273 K. Therefore, it was considered that SiH_2Cl_2 underwent a disproportionation reaction during CO_2 laser irradiation and more reactive species, such as SiH_3Cl were formed.

A gas chromatographic analysis of the chlorosilanes was performed to check the occurrence of disproportionation reaction of SiH_2Cl_2. Figure 2.7 shows the result of the gas chromatographic analysis of the chlorosilanes in the exhausted gas from the reactor when 30 st. cm^3/min of SiH_2Cl_2 was irradiated with a 3.2 kW/cm^2 CO_2 laser having a 2 mm beam diameter. The large argon peak as a carrier gas, and peaks of $SiCl_4$, $SiHCl_3$, SiH_2Cl_2 were observed. Moreover, a trace peak, which was speculated to be SiH_3Cl from its peak position, was observed. This result shows that the disproportionation reaction of SiH_2Cl_2 took place and various kinds of chlorosilanes were formed. Silicon particles were considered to be formed mainly from the highly reactive species such as SiH_3Cl and SiH_4 produced by the disproportionation reaction.

2.3.2.2 SiC formation

Figure 2.8 shows the laser absorption of SiH_2Cl_2 and C_2H_4 reactant gases, where the laser beams of 100W and 10.6 μm wavelength were irradiated onto the reactant gases flowing at various flow rates. The laser absorption of both SiH_2Cl_2 and C_2H_4 increased almost linearly with increasing their flow rates. This suggested that the laser beam was absorbed in proportion to the quantity of the reactant gas passing through the beams per unit time, since the laser beam was absorbed very fast. It was further observed that SiH_2Cl_2 and C_2H_4 gases absorbed the laser beam to almost the

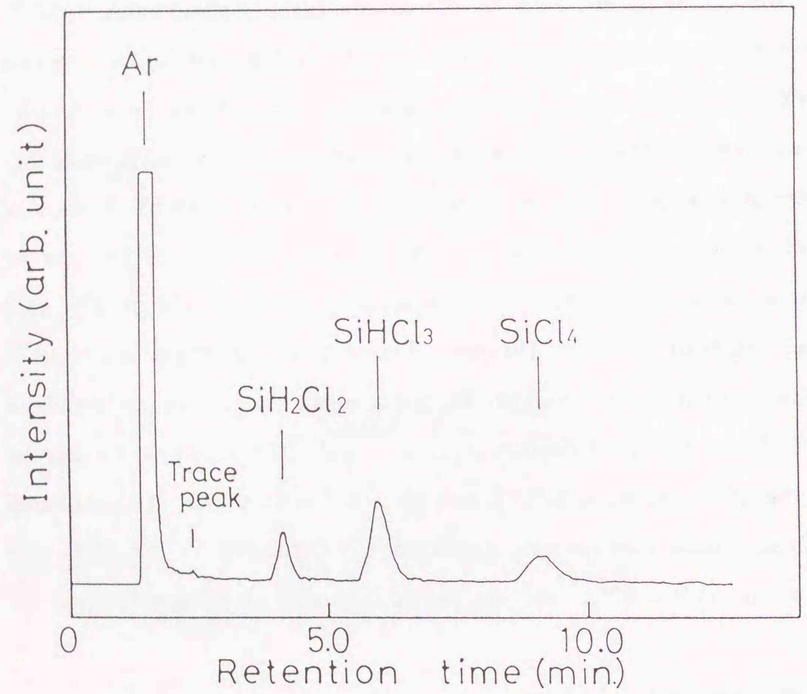

Fig. 2.7 The results of the gas chromatographic analysis of the chlorosilanes in the exhausted gas from the reactor when 30 standard cm^3/min SiH_2Cl_2 was irradiated by a CO_2 laser of power 3.2 kW/cm^2 and diameter 2 mm.
Sampling gas 1.0 ml, column DC550 (15%) supported Serite 545, SUS 3 mm diameter, 5 m, Column temperature 323 K, detector temperature 353 K, carrier gas He 30 ml/min.

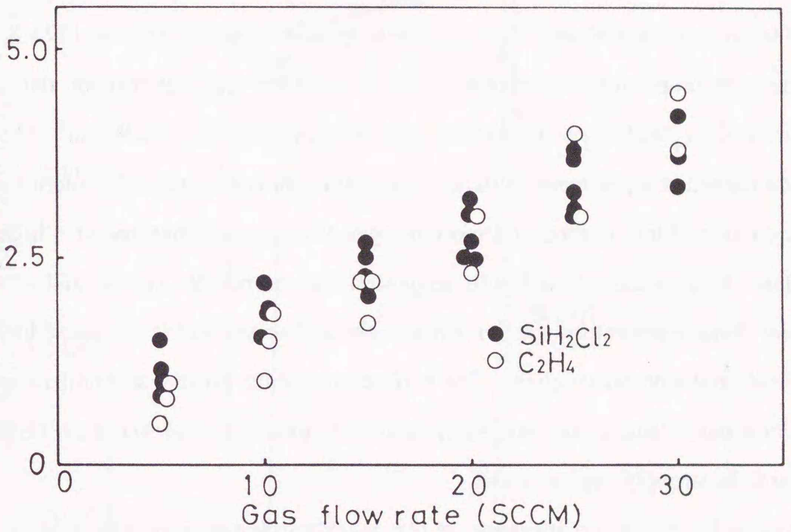

Fig. 2.8 The extent of laser light absorption by SiH_2Cl_2 and C_2H_4 as a function of reactant gas flow rate at irradiation of 100 W laser beam.
SCCM = standard cm^3/min

same extent.

The change of the reaction flame temperature with laser power density was studied to clarify the reaction mechanism. When the CO_2 laser was used to irradiate a mixture of SiH_2Cl_2 and C_2H_4 at C_2H_4/SiH_2Cl_2 = 0.5 and 0.6, hysteresis was observed between the reaction flame temperature and the laser power density (Fig. 2.9). After increasing the laser power gradually, the reaction flame temperature was low (<1237 K) until the laser power density reached about 3.3 kW/cm^2. Then it suddenly increased and reached around 3000 K. Once the reaction flame temperature reached around 3000 K, it maintained the high temperature until the laser power density decreased to around 2.0 kW/cm^2. Then, it abruptly decreased to less than 1273 K. Table 2.2 lists the properties of the powder synthesized at low and high reaction flame temperature at C_2H_4/SiH_2Cl_2 = 0.5 and a laser power density of 2.87 kW/cm^2. The powder synthesized at a low reaction flame temperature showed broad SiC pattern by XRD, but contained less carbon and more oxygen than that synthesized at a high reaction flame temperature. This results suggested that the powder synthesized at a low reaction flame temperature was not sufficiently carbonized and it contained low crystalline SiC and amorphous phase. The surface area of the powder synthesized at a low reaction flame temperature was small, and these particles were found by TEM observation to be strongly agglomerated.

The reason for the steep increase in the reaction flame temperature was assumed to be that two exothermic reactions, which were a decomposition of C_2H_4

$$1/2C_2H_4(g) \rightarrow C(s) + H_2(g), \quad \Delta H = -18.1 \text{ kJ/mol (1300 K) [20]} \quad (2.2)$$

and carbonization of silicon

$$Si(s) + C(s) \rightarrow \beta\text{-}SiC(s), \quad \Delta H = -72.8 \text{ kJ/mol (1300 K) [20]} \quad (2.3)$$

were started by increasing the laser power density, and the reaction flame temperature was increased due to their heats of reaction. Assuming that SiH_2Cl_2 was decomposed into Si(s) and 2HCl(g) at 1300 K by using absorbed laser energy, the reaction

$$Si(s) + 2HCl(g) + 1/2C_2H_4(g) \rightarrow \beta\text{-}SiC(s) + 2HCl(g) + H_2(g), \quad (2.4)$$

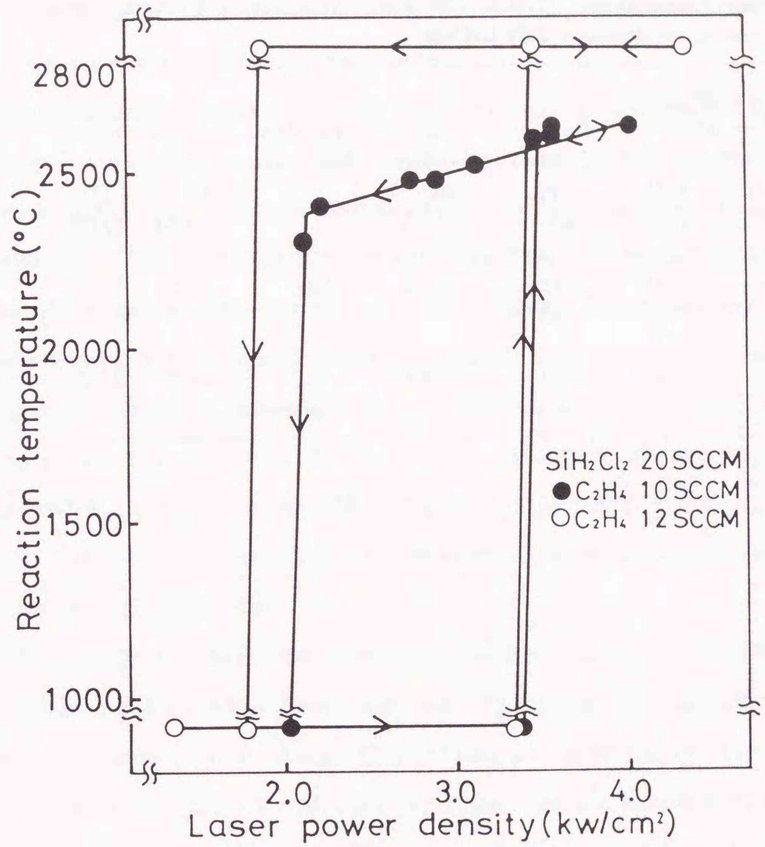

Fig. 2.9 Reaction flame temperature change as a function of laser power density. 20 standard cm^3/min SiH_2Cl_2, and (●) 10 and (○) 12 standard cm^3/min C_2H_4. SCCM = standard cm^3/min

Table 2.2 The properties of the powder synthesized at high and low reaction flame temperatures. SiH_2Cl_2 = 20 st.cm^3/min, C_2H_4 = 10 st.cm^3/min, laser power density = 2.87 kW/cm^2

Sample no.	Reactant gas flow rate SiH_2Cl_2 (st. cm^3/min)	Reactant gas flow rate C_2H_4 (st. cm^3/min)	Reaction flame temp. (K)	Specific surface area (m^2/g)	Crystalline state	Composition C (wt%)	Composition O (wt%)
15	20	10	2773 –3073	213.2	SiC	26.5	15.8
16	20	10	<1273	4.4	SiC (broad)	18.2	23.2

$$\Delta H = -90.8 \text{ kJ/mol (1300 K)}$$

proceeded quantitatively, and the heat of reaction was used entirely to heat all the products, the calculated reaction temperature was about 1900 K (heat capacity Cp (1300 K), 51.0 J/mol K, for SiC(s); 33.1, for HCl(g); 31.4 for H_2(g) were used) [20]. The actual reaction flame temperature was more than 2600 K (Fig. 2.9), so the steep increase in the reaction flame temperature could not be explained solely due to the contribution of the heat of the exothermic reactions.

Figure 2.10 shows the extent of laser light absorption when laser power density was changed. Hysteresis was observed between the extent of laser light absorption and laser power density, similar to the case of the reaction flame temperature and laser power density. When the laser power density was increased gradually, the amount of laser absorption was about 4 W until the laser power density reached about 3.0 kW/cm^2 which was almost equal to the power density at which the reaction temperature abruptly increased. Then, the amount of laser absorption abruptly increased. The degree of the laser light absorption change depended on C_2H_4/SiH_2Cl_2 ratio, becoming 2 W at C_2H_4/SiH_2Cl_2 = 0.5, 6 W at C_2H_4/SiH_2Cl_2 = 0.75. The increase in laser light absorption could be explained by solid particles formation as discussed later.

Assuming that the laser light absorption increase was all spent to heat the products, the increase in the reaction flame temperature by the laser light absorption increase could be calculated (heat capacity Cp (1300 K), 5.5 cal/mol K for C(s) were used) [20]. In the case of SiH_2Cl_2 = 20 and C_2H_4 = 10 st. cm^3/min, the temperature increase by the 2 W laser power was about 900 K and in the case of SiH_2Cl_2 = 20 and C_2H_4 = 15 st. cm^3/min, the temperature increase by 6 W laser power was about 2300 K. In the latter case, the increase in laser light absorption was enough to explain the steep increase in the reaction flame temperature. However, in the former case, the increase in laser light absorption was insufficient to cause a steep increase in the reaction flame temperature by itself, although a steep increase of more than 1800 K took place.

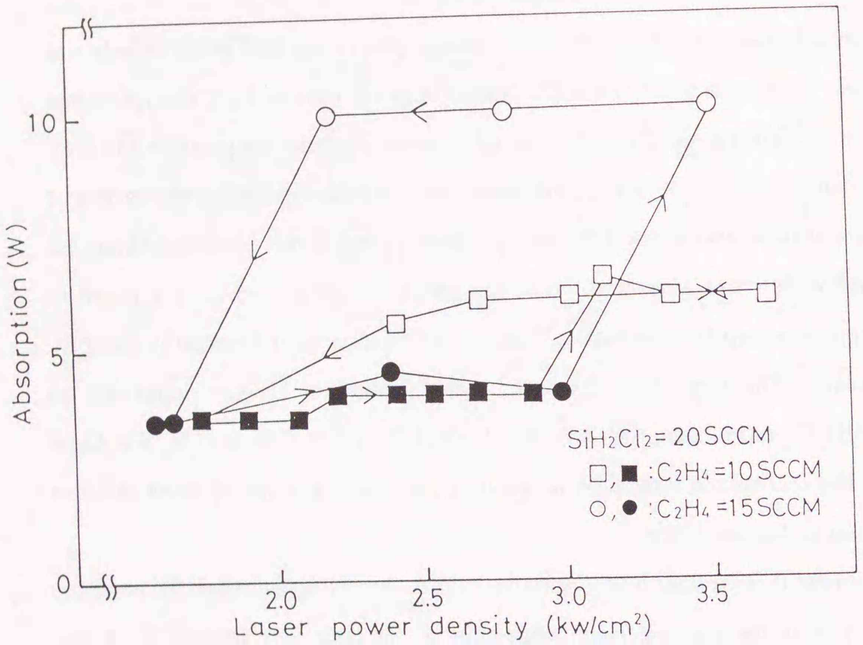

Fig. 2.10 Laser power absorption change as a function of laser power density.

(○, □) High flame temperature (>2753 K), (●, ■) low flame temperature (<1273 K).

20 st. cm^3/min SiH_2Cl_2,

(□, ■) 10 st. cm^3/min C_2H_4, (○, ●) 15 st. cm^3/min C_2H_4.

SCCM = standard cm^3/min (st. cm^3/min)

Therefore, it was considered that the steep increase in the reaction flame temperature was caused by both the initiation of exothermic reactions and the increase in laser light absorption which took place simultaneously.

Solid particles, having a strong absorption band near 10.6 μm (943 cm^{-1}), were considered as a reason for the laser light absorption increase. However, silicon did not have an absorption band near 10.6 μm. SiC had a strong absorption band near 10.6 μm [22]. Carbon had a strong absorption in the wide region ranging from 25 – 2.5 μm, that was confirmed by measuring the infrared transmittance of the carbon black (2 wt%) in the KBr pellet. Therefore, SiC and carbon particles, which were formed in the reaction flame, were considered to contribute to the laser light absorption increase. In particular, the formation of carbon particles was considered to have a more important role than SiC, for the following reasons.

1. A steep increase in the reaction flame temperature could not be observed at the low C_2H_4/SiH_2Cl_2 ratio (<0.3), even though SiC particles were formed at that ratio.

2. The degree of laser light absorption increase was larger at C_2H_4/SiH_2Cl_2 = 0.75 than at C_2H_4/SiH_2Cl_2 = 0.5. In the former case, the product powder showed a high carbon content (36.4 wt%) and free carbon was observed by XRD. However, in the latter case, the carbon content of the powder was 25.7 wt% and free carbon was not observed by XRD.

The hysteresis between the reaction flame temperature and laser power density (Fig. 2.9) could be explained as follows: when a gas mixture of SiH_2Cl_2 and sufficient C_2H_4 was irradiated with a CO_2 laser, whose power was gradually increased, the laser absorption and the reaction flame temperature could gradually increased, even though the increase in the reaction flame below 1273 K could not be observed by the pyroscope used in this experiment. As the reaction flame temperature increased, the endothermic reaction of the decomposition of SiH_2Cl_2 (Eq. 2.1) and exothermic reaction of the decomposition of C_2H_4 (Eq. 2.2) would proceed depending

exponentially on the reaction flame temperature. While the decomposition of SiH_2Cl_2 is endothermic, the decomposition of C_2H_4 and the carbonization of silicon are exothermic. The decomposition of SiH_2Cl_2 would proceed by absorbing laser energy. Then, as the exothermic reaction of the decomposition of C_2H_4 and the carbonization of Si proceed the heat of the reactions was liberated and was allowed to increase the reaction flame temperature. The increase in the reaction flame temperature accelerated these reactions more. Moreover, if the carbon particles were formed by the decomposition of C_2H_4, carbon particles could absorbed more laser light and the increase in laser absorption by carbon particles would cause the rapid increase in the reaction flame temperature. As the results, these process happen in very short region of laser power density and caused a steep increase in the reaction flame temperature. Once the reaction flame temperature became high enough, the carbon particle formation was continued to some extent by the high flame temperature itself, even if the laser power was decreased. So a high laser light absorption and a high flame temperature were maintained at a certain laser power density.

It was found by XRD that SiC was formed both at high and low reaction flame temperature. However, the mechanism of SiC formation could be different in each case.

In the case of low reaction flame temperature (<1273 K), $SiCl_4$, $SiHCl_3$, SiH_2Cl_2 and a trace peak speculated to be SiH_3Cl, were observed in the exhausted gas from the reactor by gas chromatographic analysis. SiH_2Cl_2 underwent a disproportionation reaction during laser irradiation and various kind of chlorosilanes and silane were formed. Therefore, the mechanism of SiC formation was very complex, but highly reactive species such as SiH_4 and SiH_3Cl were considered to play a very important role, especially at low temperature. Some SiH_2Cl_2, $SiHCl_3$ and $SiCl_4$ were exhausted outside without any further reaction.

In the case of the high reaction flame temperature (>3073 K), all the products of the disproportionation reaction, even the least reactive $SiCl_4$, could react with C_2H_4

forming SiC. However, small amounts of $SiCl_4$, $SiHCl_3$ and a trace of SiH_2Cl_2 were observed in the exhausted gas from the reactor by gas chromatographic analysis in spite of the high reaction flame temperature (>3073 K). This result indicated that small part of $SiCl_4$ and $SiHCl_3$ were exhausted outside without any further reaction. Some part of these compounds might form a polymeric compound, because Si–H bond was observed in the PAS spectra (Fig. 2.6) and in most experiments, a small amount of liquid material was observed near the gas outlet of the reactor. This liquid material was transparent and emitted a strong HCl odor and solidified in air within several tens of minutes. In addition, the polymeric compound might be formed at a low reaction temperature. In this experiment, the laser beam diameter was so small (2 mm) that the laser power density might be insufficient at the edge of the beam or that the residence time of reactant might be too short to complete the reaction. To complete the reaction, an increase in laser power or enlargement of the beam diameter would be needed.

2.4 Synthesis of SiC ultrafine particles from SiH_4 and C_2H_4

2.4.1 Characterization of the powder

Table 2.3 shows the preparation conditions, the composition, the specific surface area and the crystalline state of the SiC powders synthesized from SiH_4–C_2H_4 and SiH_2Cl_2–C_2H_4. In the case of SiH_4–C_2H_4, when the laser beam diameter was 4 mm and the power density was 0.4 kW/cm^2, the product powder contained much Si and XRD showed Si and amorphous phase. The reaction flame temperature was very unstable and it sometimes changed between just below 1273 K and 2200 K. TEM observations showed that the powder synthesized at a 4 mm beam diameter and a 0.4 kW/cm^2 power density (sample no. 17), consisted of mainly amorphous particles, with a particle size ranging from 20 to 60 nm. The SAED pattern showed a Si ring and an amorphous halo. The laser power density of 0.4 kW/cm^2 was not sufficient to form SiC powder.

Table 2.3 Synthesis conditions and properties of the SiC ultrafine powders synthesized using a CO_2 laser from SiH_4–C_2H_4 and SiH_2Cl_2–C_2H_2

Sample no.	Beam dia. (mm)	Power dens. (kW/cm^2)	Reactant gas flow rate (st.cm^3/min) SiH_4	SiH_2Cl_2	C_2H_2	Composition C (wt%)	O	Specific surface area (m^2/g)	Reaction flame temp. (K)	Crystalline state
17	4	0.40	32	–	20	9.9	2.1	85.2	<1273–2253*	Si(w**),Amorph.
18	4	0.92	32	–	10	13.9	2.4	32.7	1873	Si>SiC
19	4	0.92	32	–	15	21.1	2.4	42.6	2233–2353	SiC>Si
20	4	0.92	32	–	20	28.5	1.2	56.0	2173–2313	SiC>Si
21	4	0.92	32	–	22	30.5	0.8	80.3	2473	SiC
22	2	3.66	32	–	10	22.0	1.2	43.6	2073	SiC>Si
23	2	3.66	32	–	20	30.5	0.5	63.1	2713–2753	SiC
24	2	3.66	32	–	30	29.8	0.5	74.0	2573–2673	SiC
10	2	3.66	–	20	5	18.0	24.6	104.9	2823–2933	SiC
11	2	3.66	–	20	10	25.7	13.2	79.8	2573–2693	SiC
12	2	3.66	–	20	12	29.3	17.7	61.9	>3073	SiC
13	2	3.66	–	20	15	36.4	13.4	88.1	>3073	SiC,C

*unstable, **weak

In the case of laser power densities of 0.92 and 3.66 kW/cm^2, the carbon content of the powder increased and the crystalline phase changed from the mixture of Si and SiC to SiC, as the C_2H_4 flow rate increased. The carbon content of the powder reached 30.5 wt% at a C_2H_4/SiH_4 flow ratio of 0.69. The carbon content did not increase, when the C_2H_4 flow rate increased and the C_2H_4/SiH_4 flow ratio reached 0.97. In the case of the powder synthesized from SiH_2Cl_2–C_2H_4, the carbon content of the powder increased up to 36.4 wt% as the C_2H_4 flow rate increased. Figure 2.11 shows the TEM photographs of the particles synthesized at a 3.66 kW/cm^2 from SiH_4 and C_2H_4. When the C_2H_4 flow rate was 10 st. cm^3/min (A), a particle size from 10 to 120 nm was obtained and the SAED pattern showed Si and SiC rings. When the C_2H_4 flow rate increased to 20 st. cm^3/min (B), particle size ranged from 10 to 100 nm and the SAED pattern showed a SiC ring. When the C_2H_4 flow rate was 30 st. cm^3/min (C), the particle size ranged from 10 to 80 nm and the SAED pattern again showed a SiC ring. The same tendency was observed in the case of a laser power of 0.92 kW/cm^2, but at a low C_2H_4 flow rate larger particles, around 300 nm in size, were observed at a laser power density of 0.92 kW/cm^2. These particles were basically spherical. In the case of SiH_2Cl_2–C_2H_4, SiC particles having radial projections were obtained, but such particles could not be observed in the case of SiH_4–C_2H_4.

Figure 2.12 shows the bright–field and dark–field (SiC_{111}) images of the particles synthesized from SiH_4 (32 st. cm^3/min) and C_2H_4 (22 st. cm^3/min) at 0.92 kW/cm^2 (sample no. 21). The dark field image was taken by adjusting object iris to the diffraction of SiC (111) plane. The dark field image showed that the SiC particles contained very small SiC crystals (1–15nm). The mean diameter of these SiC crystals was almost equal to 4.4 nm, which was estimated from Scherrer's method by measuring the half width of SiC_{111} diffraction line.

The powders were handled in air. The oxygen content of the powder synthesized from SiH_4 and C_2H_4 varied between from 0.5 to 2.4 wt%, and decreased as the carbon

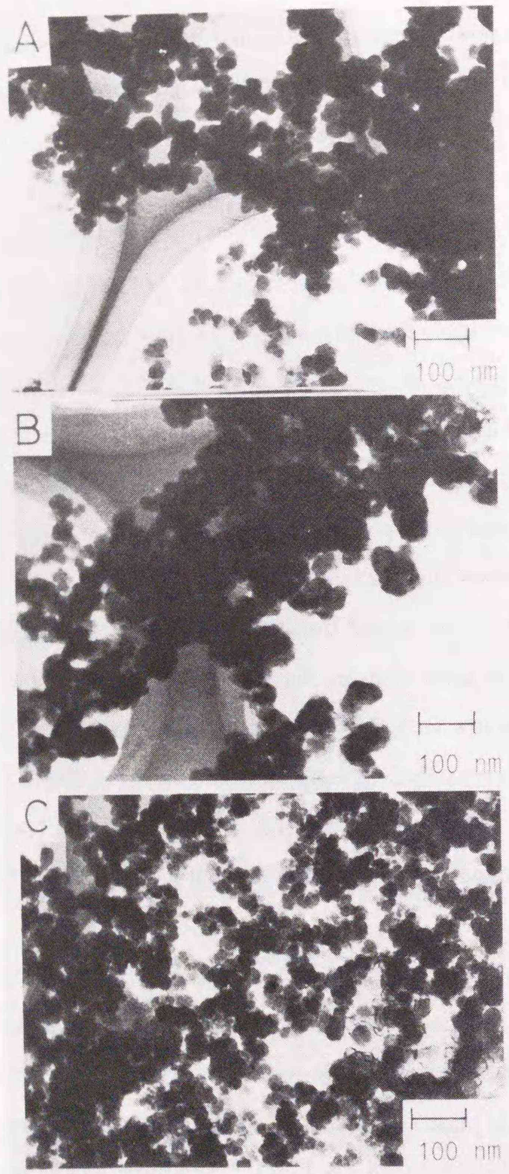

Fig. 2.11 TEM photographs of SiC particles synthesized from SiH_4–C_2H_4 at various reactant gas flow rates. Beam diameter 2 mm; Laser power density 3.66 kW/cm^2; SiH_4 32 standard cm^3/min; (A) C_2H_4; 10 (B) C_2H_4; 20 (C) C_2H_4; 30 standard cm^3/min

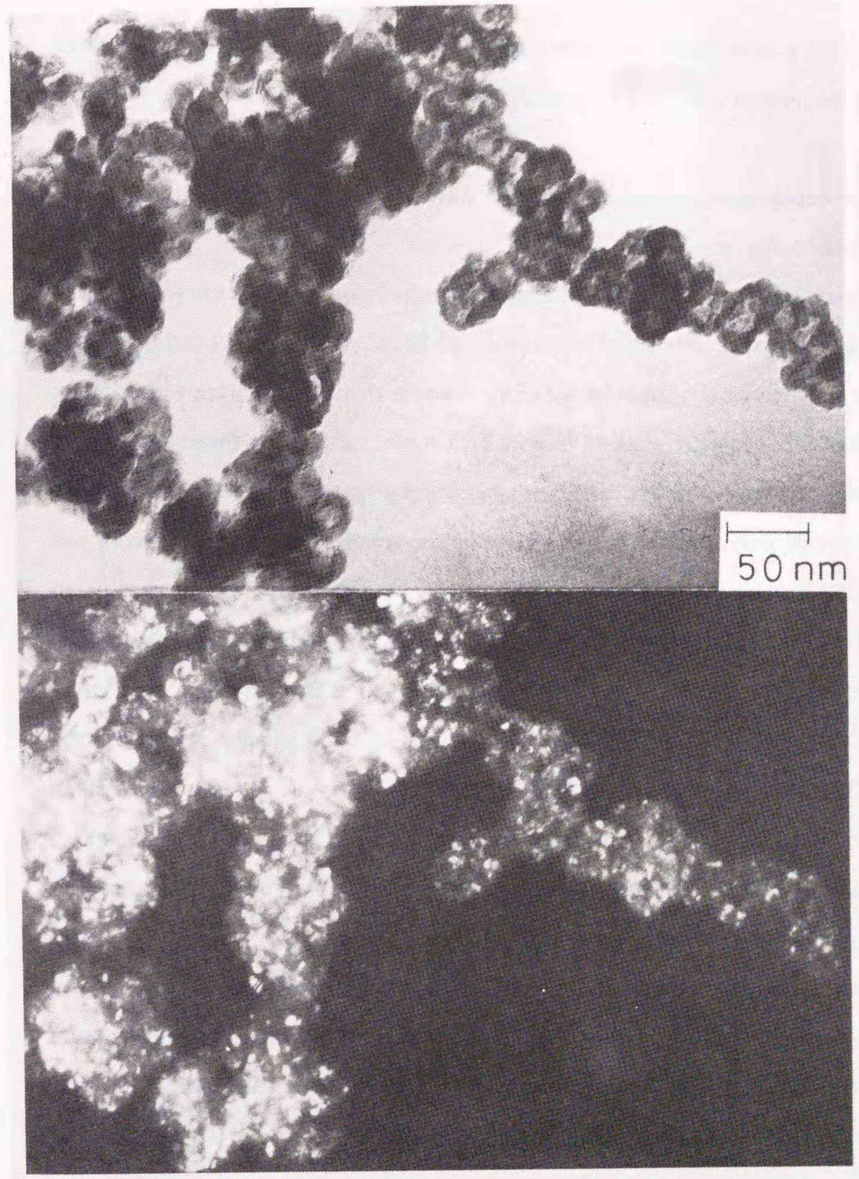

Fig. 2.12 Bright–field and dark–field (SiC_{111}) images of SiC ultrafine particles. SiH_4 32 standard cm^3/min, C_2H_4 22 standard cm^3/min, laser power density 0.92 kW/cm^2, beam diameter 4 mm.

content of the powder increased. The oxygen content was extremely small compared to that of the powder from SiH_2Cl_2 and C_2H_4.

2.4.2 The relationship between reaction flame temperature and the extent of laser light absorption

The reaction flame temperature depended on the laser power density and on the reactant gas flow rate and tended to become high as the power density and C_2H_4 flow rate increased. However, the behavior of the reaction flame temperature was different from that of SiH_2Cl_2–C_2H_4 system. Figure 2.13 shows the reaction flame temperature dependence on the laser power density at a beam diameter of 2 mm. With a increase in laser power density, the reaction flame temperature abruptly increased from just below 1273 K to around 2000 K at a certain laser power density. It was speculated that the temperature increase occurred near 1273 K, based on the temperature range of the pyrometer between 1273 to 3073 K. Then, the reaction flame temperature slightly increased in the case of SiH_4=32, C_2H_4=10 st. cm^3/min, but gradually increased in the case of SiH_4 (32 st. cm^3/min)+ C_2H_4 (20 and 30 st. cm^3/min), as the power density increased. The critical laser power density, at which an abrupt temperature increase occurred, depended on the total reactant gas flow rate, and became larger as the total reactant gas flow rate increased.

Figure 2.14 shows the extent of laser light absorption by the reaction flame, when the laser power density changed. The amount of laser light absorption increased linearly until the laser power density reached a value of about 0.8 kW/cm^2. In this region, the reaction flame temperature was low (<1273K). Above 0.8 kW/cm^2, the absorption gradually increased and a saturation was observed at about 9 W in the case of C_2H_4 (10 st. cm^3/min), but in the case of C_2H_4 (20 and 30 st. cm^3/min) it remained almost unchanged until 2 kW/cm^2, then increased again with the increase of power more than 2 kW/cm^2. An abrupt increase in the reaction flame temperature occurred at which

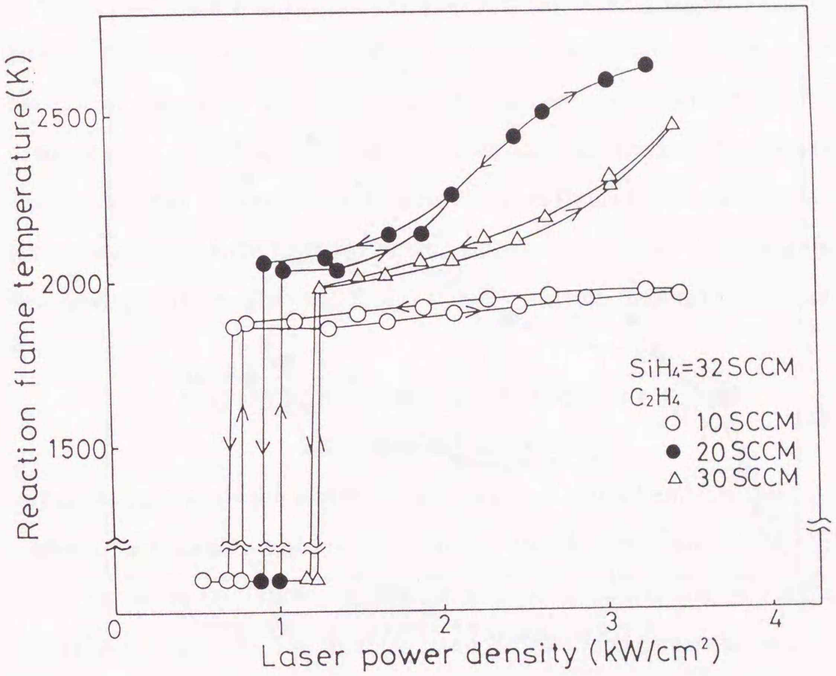

Fig. 2.13 Reaction flame temperature change versus laser power density:
Beam diameter 2 mm
SCCM = standard cm^3/min

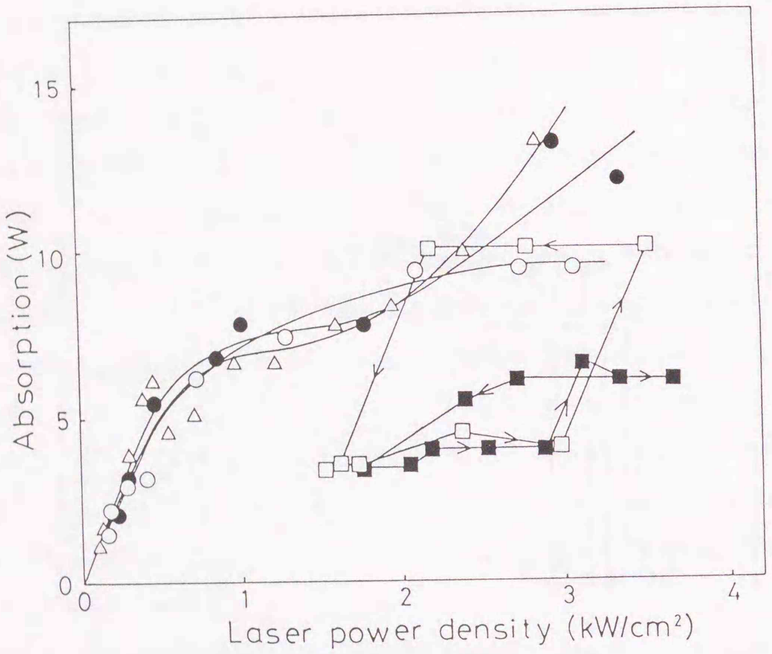

Fig. 2.14 The extent of the laser light absorption by reactant gases versus laser power density: Beam diameter 2 mm

SiH_4 (32 standard cm^3/min) + C_2H_4 (10(●), 20(○), 30(▲) standard cm^3/min)

SiH_2Cl_2 (20 standard cm^3/min) + C_2H_4 (10(■), 15(□) standard cm^3/min)

the increase rate of the laser absorption was reduced (around 1 kW/cm^2). An abrupt laser light absorption change corresponding to the abrupt increase of the reaction flame temperature could not be observed. The rapid increase in the reaction flame temperature was not caused by the change of the laser light absorption. The gradual increase in the reaction flame temperature above 0.8 kW/cm^2 corresponded to the gradual increase in laser light absorption. A hysteresis was not found, unlike the case of SiH_2Cl_2–C_2H_4.

When the laser power density was low, Si particles were mainly formed as the result of the decomposition of SiH_4 and the amount of carbon was low as shown in the case of sample no. 17 in Table 2.3. As the laser power density increased, the decomposition of C_2H_4 and carbonization of Si occurred. Because these reactions are exothermic, the abrupt increase in the reaction flame temperature takes place simultaneously with the initiation of the exothermic reactions. Assuming that SiH_4 was decomposed into Si(s) and $2H_2$(g) at 1300 K by the absorbed laser energy, then the reaction

$$Si(s) + 1/2C_2H_4(g) + 2H_2(g) \rightarrow \beta\text{–}SiC(s) + 3H_2(g),$$

$$\Delta H = -90.9 \text{ kJ/mol (1300K)}$$

proceeds quantitatively, and if the reaction heat is used entirely to heat all the products, the calculated reaction temperature is 1930 K in the case of SiH_4/C_2H_4=2:1. (Heat capacities Cp(1300K) of 50.8 J/K mol for β–SiC(s) and 94.3 J/K mol for $3H_2$(g) were used) [20] The observed reaction flame temperatures immediately after the abrupt increase were 1800, 2030, 1970 K for SiH_4 (32 st. cm^3/min) and C_2H_4 (10, 20, 30 st. cm^3/min), respectively. The calculated value was considered to be almost equal to the observed reaction flame temperature.

Sawano et al. [4] reported a similar abrupt increase in the reaction flame temperature in the SiH_4–CH_4 system. They observed the abrupt increase in the reaction flame temperature, when they changed the total reactant gas flow rate at a constant CH_4/SiH_4 flow ratio of 1:1, at 9.6 x 10^4 Pa (0.95 atm), at a power density of

4 kW/cm^2. They called that phenomenon 'Ignition'. They thought that the reaction proceeded through a two-stage mechanism and 'Ignition' was caused by the initiation of the exothermic reaction Si(s) + C(s) → SiC(s). However, they did not report the extent of laser light absorption.

2.5 Comparison of SiH_4–C_2H_4 with SiH_2Cl_2–C_2H_4

In this section the behaviors of the reaction flame temperature in relation to the laser light absorption were compared in the two systems. In the case of the synthesis of SiC powder from SiH_2Cl_2–C_2H_4 by a CO_2 laser, the abrupt increase in reaction flame temperature and the abrupt increase in the laser light absorption occurred simultaneously at a certain laser power density. (Fig. 2.9, 2.10) In addition, a hysteresis was found between the reaction flame temperature and the laser power density and between the extent of laser light absorption and the laser power density. In the case of the system SiH_2Cl_2–C_2H_4, it was concluded that the abrupt increase in the reaction flame temperature was caused by both the initiation of the exothermic reaction and the increase in the extent of laser light absorption. The increase in the laser light absorption was caused by the solid carbon particles formed in the reaction flame, because carbon is a good absorber of CO_2 laser light.

The behavior of the reaction flame temperature and the extent of the laser light absorption in the system SiH_4–C_2H_4 was different from SiH_2Cl_2–C_2H_4, even though the exothermic reactions played an important role in both cases.

Thermodynamic calculation was made to consider the difference between SiH_2Cl_2–C_2H_4 and SiH_4–C_2H_4 by the chemical thermodynamic computation (CTC) system [23]. CTC system has been designed to facilitate the application of chemical thermodynamic considerations to practical problems in the material science and constructed in Tsukuba Research Center of Agency of Industry and Science Technology. Figures 2.15 and 2.16 show the equilibrium composition of the SiH_4–C_2H_4 and SiH_2Cl_2–C_2H_4 reactions calculated at a C/Si ratio of 1:1. In the case of the

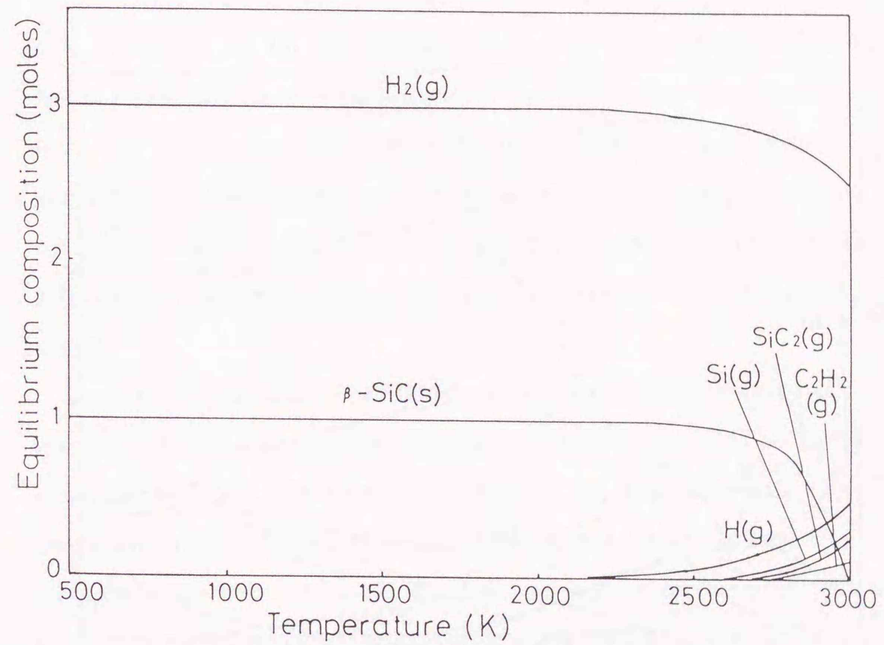

Fig. 2.15 Equilibrium composition of the SiH_4–C_2H_4 reaction calculated by CTC [23]: SiH_4 1.0 mol, C_2H_4 0.5 mol, 1 atm. Small amounts (<0.05 mol) of SiC_2(g) and SiH(g) present above 2600K were ignored.

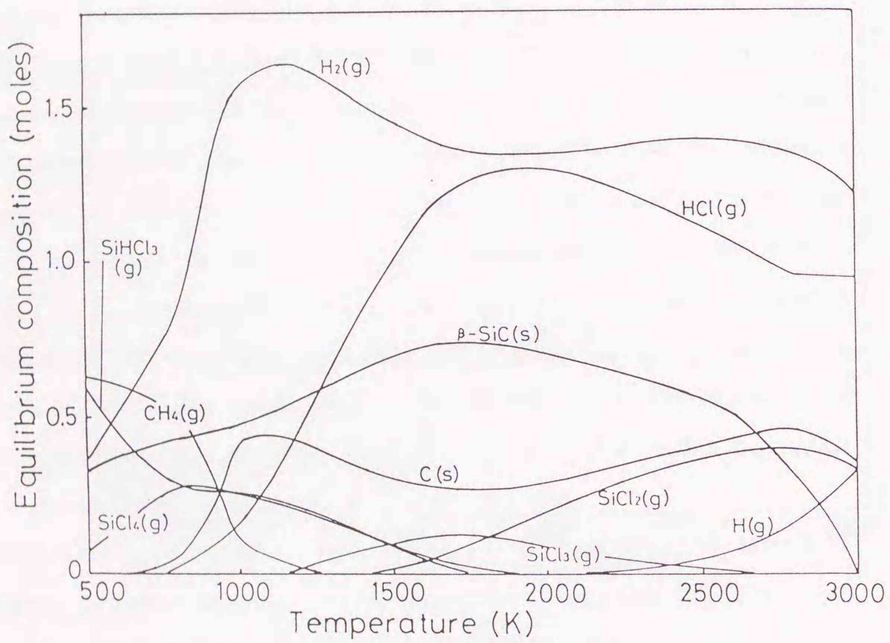

Fig. 2.16 Equilibrium composition of the SiH_2Cl_2–C_2H_4 reaction calculated by CTC [23]: SiH_2Cl_2 1.0 mol, C_2H_4 0.5 mol, 1 atm. Small amounts (<0.2 mol) of Si(g), Cl(g), SiCl(g), C_2H_2(g), SiC_2(g) present above 2400K were ignored.

SiH_4–C_2H_4 system, only H_2(g) and β–SiC(s) are present below 2000K. In contrast, in the SiH_2Cl_2–C_2H_4 reaction many species are present; especially, much C(s) is found even though the C/Si ratio was stoichiometric (C/Si=1:1). This result suggested that C(s) particles are formed easily in the SiH_2Cl_2–C_2H_4 system and not easily in the SiH_4–C_2H_4 system. In fact, in the case of the SiH_2Cl_2–C_2H_4, C was detected by XRD in the powder synthesized with an excess of C_2H_4 (Table 2.3, no. 28), but C was not found by XRD in the powder synthesized with an excess of C_2H_4 in the case of SiH_4–C_2H_4. (Table 2.3, no. 13) The difference in tendency to form C(s) particles was the reason for the difference of the behavior of the reaction flame temperature and the laser light absorption in the SiH_4–C_2H_4 and the SiH_2Cl_2–C_2H_4 system. It was suggested that the hysteresis of the reaction flame temperature and the laser absorption found in the SiH_2Cl_2–C_2H_4 system is connected with the formation of solid carbon particles, because such hysteresis was not found in the SiH_4–C_2H_4 system.

The major disadvantages of SiH_2Cl_2 as a source for laser–induced gas–phase reaction were poor absorption of the laser light (10.6 μm) and poor reactivity compared with SiH_4. In the case of SiH_2Cl_2–C_2H_4, high laser light absorption, comparable with the SiH_4–C_2H_4 mixture was achieved due to the formation of solid black carbon particle. (Fig. 2.14) The low laser light absorption of SiH_2Cl_2 could possibly be overcome by taking advantage of the formation of solid black carbon particles.

2.6 Conclusion

(1) SiC ultrafine particles were synthesized by a CO_2 laser at atmospheric pressure from C_2H_4 and SiH_2Cl_2. The composition of the powder changed with the C_2H_4/SiH_2Cl_2 ratio. The reaction flame temperature was low (<1273 K) at low C_2H_4/SiH_2Cl_2 ratio, and rapidly increased to around 3000 K when the C_2H_4/SiH_2Cl_2 exceeded 0.3. This rapid temperature increase was caused by initiation of exothermic

reactions and the rise in laser light absorption caused mainly by the carbon particles formation and partly due to SiC particles formation. It was found that SiH_2Cl_2 underwent a disproportionation reaction on CO_2 laser irradiation, and that SiC was formed through the various products of the disproportionation reaction.

(2) SiC ultrafine particles were synthesized by irradiating the SiH_4–C_2H_4 gas mixture with a CO_2 laser at atmospheric pressure. An abrupt increase in the reaction flame temperature was observed at a certain laser power density, as the laser power density gradually increased. This was caused by the exothermic reactions of the decomposition of C_2H_4 and the carbonization of Si.

(3) The behavior of the reaction flame temperature and the extent of laser light absorption in the SiH_4–C_2H_4 system with increasing laser power density was different from that in the SiH_2Cl_2–C_2H_4 system. This difference resulted from the fact that solid black carbon particles were easily formed in the case of SiH_2Cl_2–C_2H_4, but not as easily in the case of SiH_4–C_2H_4. Because of the formation of black solid carbon particles, high laser light absorption, comparable with that in the SiH_4–C_2H_4 system, occurred in the SiH_2Cl_2–C_2H_4 system.

References

1. W.R. Cannon, S.C. Danforth, J.H. Flint, J.S. Haggerty and R.A. Marra, "Sinterable Ceramic Powders from Laser–Driven Reactions: Process Description and Modeling", J. Am. Ceram. Soc., 65(7), 324–30 (1982).
2. W.R. Cannon, S.C. Danforth, J.S. Haggerty and H.K. Bowen, "Sinterable Ceramic Powders from Laser–Driven Reactions: Powder Characteristics and Process Variables", ibid, 65(7), 330–35 (1982)
3. Y. Suyama, R.A. Marra, J.S. Haggerty and H.K. Bowen, "Synthesis of Ultrafine SiC Powders by Laser–Driven Gas Phase Reactions", Am. Ceram. Soc. Bull., 64(10), 1356–59 (1985).
4. K. Sawano, J.S. Haggerty and H.K. Bowen, "Formation of SiC Powder from Laser Heated Vapor Phase Reactions", Yogyo Kyokai–shi 95(1), 64–69 (1987).
5. Y. Kizaki, T. Kandori and Y. Fujitani, "Synthesis and Characterization of Si_3N_4 Powder Produced by Laser–Induced Chemical Reactions", Jpn J. Appl. Phys. 24, 800–805 (1985)
6. M. Cauchetier, O. Croix and M. Luce, "Laser Synthesis of Silicon Carbide Powders from Silane and Hydrocarbon Mixtures", Adv. Ceramic Mater., 3, 548–52 (1988).
7. M. Suzuki, Y. Nakata, T. Okutani and A. Kato, "Preparation of SiC Ultrafine Particles by Using CO_2 Laser", Seramikkusu Ronbunshi, 97, 972–75 (1989)
8. M. Suzuki, Y. Nakata, T. Okutani and A. Kato, "Preparation of SiC Ultrafine Particles from SiH_2Cl_2 and C_2H_4 Gas Mixtures by a CO_2 Laser", J. Mater. Sci., 27, 6091–97 (1992)
9. W. Symons and S.C. Danforth, "Synthesis and Characterization of Laser–Synthesized Silicon Nitride Powders", pp249–56 in Advances in Ceramics, Vol.21, Edited by G.L. Messing, K.S. Mazdiyasni, J.W. McCauley and R.A. Haber, Am. Ceram. Soc., Westerville, OH., 1987
10. M. Aoki, J.H. Flint and J.S. Haggerty, "Synthesis of Non–Agglomerated Si_3N_4

Powder", pp253–60 in Ceramic Transactions, Vol.1, Ceramic Powder Science– , Edited by G.L. Messing, E.R. Fuller Jr. and H. Hausner, Am. Ceram. Soc., Westerville, OH., 1988

11. G.W. Rice, "Laser Synthesis of Si/C/N Powder from 1,1,1,3,3,3–Hexamethyldisilazane", J. Am. Ceram. Soc., 69(8), C183–C185 (1986)
12. R. Alexandrescu, I. Morjan, E. Borsella, S. Botti, R. Fantoni, T. Dikonimos–Makris, R. Giorgi and S. Enzo, "Composite Ceramic Powders Obtained by Laser Induced Reactions of Silane and Amines", J. Mater. Res., 6(11), 2442–51 (1991)
13. M. Suzuki, Y. Maniette, Y. Nakata and T. Okutani, "Synthesis of Silicon Carbide–Silicon Nitride Composite Ultrafine Particles using a CO_2 Laser", J. Am. Ceram. Soc., 76(5), 1195–200 (1993)
14. A.K. Knudsen "Laser Driven Synthesis and Densification of Ultrafine Boron Carbide Powders", pp237–47 in Advances in Ceramics, Vol.21, Edited by G.L. Messing, J.S. Mazdiyasni, J.W. McCauley and R.A. Haber, Am. Ceram. Soc., Westervillelle, OH., 1987
15. A. Gupta and J.T. Yardley, "Production of Light Olefins from Synthesis Gas Using Catalysts Prepared by Laser Pyrolysis", pp131–39 in SPIE 458, Applications of Lasers to Industrial Chemistry, 1984
16. R.A. Bauer, J.G.M. Becht, F.E. Kruis, B. Scarlett and J. Schoonman, "Laser Synthesis of Low–Agglomerated Submicrometer Silicon Nitride Powders from Chlorinated Silanes", J. Am. Ceram. Soc., 74(11), 2759–68 (1991)
17. J. A. O'Neill, M. Horsburgh, J. Tann, K. J. Grant and G. L. Paul, "Production of Fine Ceramic Powders from Chloromethylsilanes Using Pulsed Excimer Radiation" J. Am. Ceram. Soc., 72, 1130–35 (1989)
18. T. Okutani, Y. Nakata, M. Suzuki, M. Yamaguchi, M. Kikuchi, J. Watanabe and N. Iwamoto, "YAG Laser Synthesis of SiC Powder from Mixture of SiO_2 and C" Seramikkusu Ronbunnshi 97, 1537–42 (1989)
19. R.A. Bauer, R. Smulders, E.R. Geus, P.J. van der Put, J.G.M. Becht and J. Schoonman, "Laser Vapor Phase Synthesis of Submicron Silicon and Silicon Nitride Powders from Halogenated Silanes" Ceram. Eng. Sci. Proc., 9, 949–956 (1988).
20. JANAF Thermochemical Tables, 3rd ed. Edited by Chase et al., J. Phys. Chem. Ref. Data 14 Suppl. 1 (1985)
21. R. S. Roth, T. Negas and L. P. Cook, "Phase diagrams for Ceramists" , American Ceramic Society, Westerville OH., p370, 1983
22. G. Ramis, P. Quinted, M. Cauchetier, G. Busca and V. Lorenzelli, "Surface Chemistry and Structure of Ultrafine Silicon Carbide: An FT–IR Study" J. Am. Ceram. Soc., 72(9), 1692–97 (1989)
23. H. Yokokawa, M. Fujishige, S. Ujiie and M. Dokiya, "Construction of Thermodynamic Database and Its Utilization", J. of the National Chemical Laboratory for Industry, 83, Special issue, (1988)

CHAPTER 3

SYNTHESES OF SILICON CARBIDE– SILICON NITRIDE COMPOSITE ULTRAFINE PARTICLES BY LASER–INDUCED GAS–PHASE REACTION METHOD

CHAPTER 3

Synthesis of Silicon Carbide–Silicon Nitride Composite Ultrafine Particles by laser–induced gas–phase reaction

3.1. Introduction

In the case of laser–induced gas phase reactions, only the reaction gas is heated, whereas the reaction vessel remains at room temperature. The reaction proceeds uniformly within this restricted heat zone, and heating and cooling process can be very fast. Moreover, because of the easy operation of the laser beam, the synthesis conditions are easily controlled precisely and reproducibly. For all of these reasons, the laser method is one of the best methods to obtain ultrafine particles of very pure and uniform in composition and particle size. Ultrafine particles of Si [1,2], SiC [1–6], Si_3N_4 [1,2,7,8], Si/C/N [9,10], B_4C [11], and Fe/Si/C [12] have been synthesized by a laser–induced gas–phase reaction.

Composite ceramics having a "composite composition" may have better properties than monolithic ceramics. Such ceramics composites have been attracting the attention of many researchers. As it is thought that the particle size and the composition and structure of starting powders have a great influence on the properties of composite ceramics [13], it is necessary to synthesize fine particles having a precisely controlled structure and composition.

There have been a few reports [9,10,14] on the preparation of SiC–Si_3N_4 composite fine particles by a laser–induced gas–phase reaction. Rice et al. [9,14] synthesized amorphous Si/C/N fine particles from $((CH_3)_3Si)_2NH$ and studied the reaction kinetics. Cauchetier et al. [10] reported the synthesis of amorphous Si/C/N fine particles from SiH_4–CH_3NH_2 and SiH_4–C_2H_2–NH_3. They reported the IR spectra of powders and the effect of heat treatment. But no precise investigation has been reported regarding the structure of the composite particles. In this chapter, the

synthesis conditions and the structure of SiC–Si_3N_4 composite ultrafine particles were studied. SiH_4, C_2H_4 and NH_3 were employed as the reactant gases. They absorb CO_2 laser light and it was expected that the powder composition could be extensively controlled by changing the gas flow ratio of three reactant gases. The structure and morphology of the composite particles and chemical state of the element of the composite particles have been investigated by X–ray diffraction (XRD), transmission electron microscope (TEM), X–ray photoelectron spectroscopy (XPS) and electron energy loss spectroscopy (EELS).

The very unique SiC–Si_3N_4 composite particles were derived by this laser–induced gas–phase reaction method. While composite particles derived by other method showed amorphous phase [10], or a mixture of SiC and Si_3N_4 [22], these composite particles in this research showed a broad β–Sic pattern in XRD, even though they contained several wt% nitrogen. The results of structural analysis showed that a large amount of nitrogen dissolved into β–SiC lattice, even though the amount of dissolving nitrogen could not be quantified. It was said that nitrogen can dissolve into β–SiC as an electron donor, but the amount of dissolved nitrogen was usually too small to detect. These composite particles having unique structure has not been reported yet and a quick heating and quenching process of laser–induced gas–phase reaction make it possible to realize such a unique structure.

3.2. Experimental procedures

The CO_2 laser reactor has been described in chapter 2. After the reactor was evacuated, argon gas was introduced into it. Then, the reactant gases were introduced through a 1–mm–internal–diameter stainless steel pipe, and were irradiated at a right angle with a CO_2 laser beam with a wavelength of 10.6 μm. Composite ultrafine particles were synthesized by irradiating a gas mixture of SiH_4, C_2H_4 and NH_3 with a

CO_2 laser at atmospheric pressure. The purity of reactant gases was 99.99% for SiH_4, 99.5% for C_2H_4, and 99.9% for NH_3. The laser beam having a diameter of 10 mm was focused with a ZnSe lens to 2 and 4 mm at the reaction zone. The reaction flame temperature was measured using a pyroscope having a measurable range from 1273 to 3073 K. The production rate of the composite powders was in the range of 1.5 to 4.8 g/h.

The powders were subsequently analyzed by X–ray diffraction (XRD) for the crystalline phase, the one–point BET method for the surface area. The composition of the powder was determined with an N, O analyzer (Horiba, EMGA–550) for the oxygen and nitrogen content, and C analyzer (Horiba, EMIA–510) for the carbon content. The lattice constants of β–SiC were measured from the β–SiC (311) line and were corrected by highly pure Si (99.99%) that was mixed with the SiC–Si_3N_4 composite powder as an internal standard. The lattice constants of Si_3N_4 were measured from the α–Si_3N_4 (411) and (004) lines for α–Si_3N_4 and from the β–Si_3N_4 (212) and (002) lines for β–Si_3N_4. They were corrected by highly pure Si as an external standard, since Si and Si_3N_4 diffraction lines overlapped each other. The particle morphology and structure was observed by transmission electron microscopy (TEM, Hitachi, H800–NA) and selected area electron diffraction (SAED). The samples for TEM were prepared using a dispersion method. A dilute dispersion of the powder in reagent–grade ethanol was homogenized with an ultrasonic probe. Then, a drop of dispersion was deposited on a 3–mm–diameter microgrid, followed by drying at room temperature. The composition of the particles was analyzed by electron energy loss spectroscopy (EELS). The chemical state of the elements was measured by X–ray photoelectron spectroscopy (XPS, Kratos, XSAM800). XPS spectra were taken in the fixed analyzer transmission (FAT) mode and the pass energy was 20.0 eV. The X–ray source was Al Kα irradiation. The full width at half maximum (FWHM) of 1.1 eV was derived for Au4f7/2 peak under these conditions. A charge shift was observed for all of the samples because of their low electric

conductivity and was corrected by the Au4f7/2 peak from the small quantity of gold evaporated onto the sample surface. The binding energy of Au4f7/2 (83.8eV) was employed as the reference energy in XPS.

3.3. Results and Discussion

Table 3.1 shows the synthesis conditions and the composition, the specific surface area, the crystalline state of the composite ultrafine particles, and the reaction flame temperature. In the case of a 4–mm laser beam and a 0.4 kW/cm^2 power density, the results of the composition analysis and XRD showed that the powder contained a large amount of Si. The carbon content did not change significantly, even if the C_2H_4 flow rate increased. Apparently the laser power of 0.4 kW/cm^2 was not sufficient for C and SiC formation.

Figure 3.1 shows the XRD patterns of the composite powders with their compositions, using a 4–mm–diameter laser beam and a power density of 0.92 kW/cm^2. The crystalline state of the powder which contained 25.3 wt% carbon and 5.8 wt% nitrogen was β–SiC [15]. As the carbon content of the powder decreased, Si and amorphous phase appeared. At the same time SiC peaks slightly shifted toward high 2–Theta positions. This shift showed the change in lattice constants, which is discussed later. (Fig. 3.8) Furthermore, crystalline Si_3N_4 [16] appeared when the nitrogen content exceeded 19.5 wt%. The same tendency was observed at a laser power of 3.66 kW/cm^2.

The reaction flame temperature depended on the laser power density, the beam diameter, and the reactant gas flow rate. At the same beam diameter and the reactant gas flow rate, the reaction flame temperature was higher at 0.92 kW/cm^2 than at 0.40 kW/cm^2. Even though the total laser power was the same, the reaction flame temperature was higher at a 4–mm beam diameter and 0.92 kW/cm^2 than at 2 mm and 3.66 kW/cm^2. The residence time of the reactant in the laser beam was longer with

Table 3.1 Synthesis conditions and composition, specific surface area and the crystalline state of SiC–Si_3N_4 composite ultrafine powders synthesized using a CO_2 laser

Sample no.	Beam dia. (mm)	Power dens. (kW/cm^2)	Reactant gas flow rate (sccm) SiH_4	C_2H_4	NH_3	Composition (wt%) C	N	O	Specific surface area (m^2/g)	Reaction flame temp. (K)	Crystalline state
9	4	0.40	32	20	27	8.4	13.5	3.0	79.9	2073	Si, SiC, Amo.
10	4	0.40	32	10	27	8.5	18.2	2.9	63.9	2133	Si, SiC, Amo.
11	4	0.40	32	10	54	5.4	24.7	3.3	68.4	2213	Si,SiC, Amo.
12	4	0.92	32	20	7	25.3	5.8	1.0	95.4	2233	SiC
13	4	0.92	32	15	14	18.6	11.0	2.1	72.1	2333	SiC>>Si, Amo.
14	4	0.92	32	15	17	17.9	13.1	1.9	65.6	2333	SiC, Amo.
15	4	0.92	32	20	27	16.9	14.5	1.7	71.3	2393–2453	SiC>>Si, Amo.
16	4	0.92	32	10	27	11.5	19.5	2.2	46.0	2873	SiC>>Si, Si_3N_4, Amo.
17	4	0.92	32	10	54	6.7	28.0	2.3	59.8	>3073	SiC, Si_3N_4, Amo.
18	4	0.92	32	6	35	6.5	27.6	0.8	33.6	3073	Si_3N_4>Si, SiC
19	4	0.92	32	5	41	4.5	29.5	1.3	27.9	>3073	Si_3N_4>>Si, SiC
20	4	0.92	32	3	41	2.8	30.9	0.8	25.6	>3073	Si_3N_4, Si>>SiC
21	4	0.92	16	10	27	11.3	20.4	3.2	81.9	2873	SiC
22	2	3.66	32	20	27	15.8	14.1	2.5	78.8	2283	SiC>Si, Amo.
23	2	3.66	32	10	27	11.2	20.1	2.5	58.2	2473–2513	SiC>Si, Si_3N_4, Amo.
24	2	3.66	32	10	54	6.9	27.7	3.0	78.7	2493	SiC, Si_3N_4, Amo.

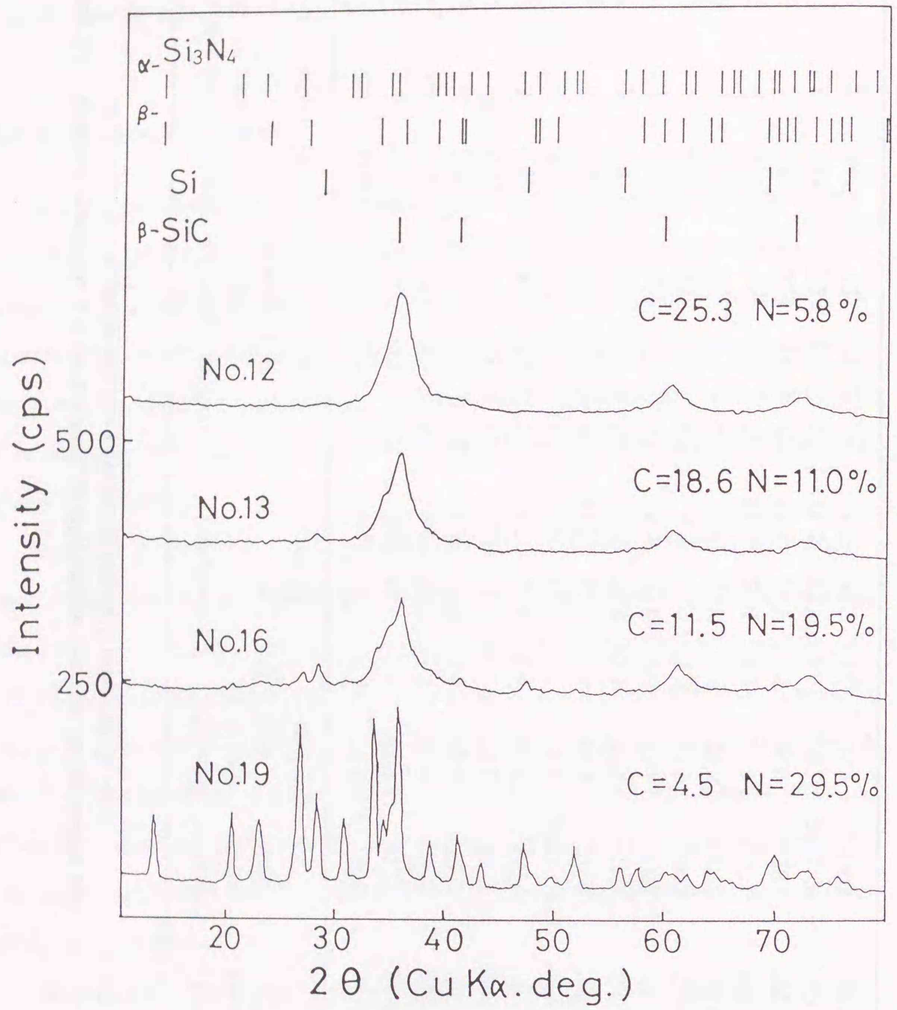

Fig. 3.1 X–ray diffraction patterns of SiC–Si_3N_4 composite ultrafine powders synthesized using a CO_2 laser (Beam diameter, 4 mm; laser power density, 0.92 kW/cm^2).

the 4–mm beam diameter, so the laser beam was absorbed more by the reactant or the fine particles produced. The reaction flame temperature increased as the NH_3 flow rate increased.

Figure 3.2 shows the change in the carbon and nitrogen content with the reactant gas flow rate. At the power densities of 0.92 and 3.66 kW/cm^2, a linear relationship was observed between the carbon, nitrogen content and the carbon atomic ratio in the gas mixture of C_2H_4 and NH_3 ($2[C_2H_4]/(2[C_2H_4]+[NH_3])$). The results show that the composition of the powder could be controlled by the reactant gas flow rate.

Figure 3.3 shows TEM photos of the powders prepared at 4 mm, 0.92 kW/cm^2 with various reactant gas flow rates. The powders with a high carbon content (A,B) consisted of uniform particles, whose sizes were around 0.02 μm. Selected area electron diffraction (SAED) of these powders showed broad rings of SiC and a trace of Si. These results show that the powders with a high carbon content consisted of very uniform particles having a SiC structure. Figure 3.4 shows the bright– and dark–field images of sample 12 (Fig. 3.3 (A)). The dark–field image (SiC_{111}) shows that these particles were made of very small SiC crystals (3–10 nm). The mean crystalline size estimated by Scherrer's method was in the range of 2.4 to 5.4 nm, which agreed with the dark–field observation.

As the nitrogen content increased (C,D), particles having diameter of 0.1 to 0.2 μm appeared and the SAED pattern showed a Si_3N_4 diffraction spot besides broad SiC rings.

Figure 3.5 shows the XPS spectra of the composite powders and mechanical mixtures of commercial SiC and Si_3N_4 powders in the Si2p region. The mixtures were prepared using a alumina mortar by mixing SiC and Si_3N_4 powders with different mixing ratios. Two kinds of SiC (0.1 and 7.1 m^2/g) and a Si_3N_4 (2.1 m^2/g) were used. Comparisons of mechanically mixed powders and composite powders were made at a similar area intensity ratio of N1s/Si2p of XPS spectra. The XPS Si2p spectra of the mixed powders consisted of SiC and Si_3N_4 peaks, and their peak

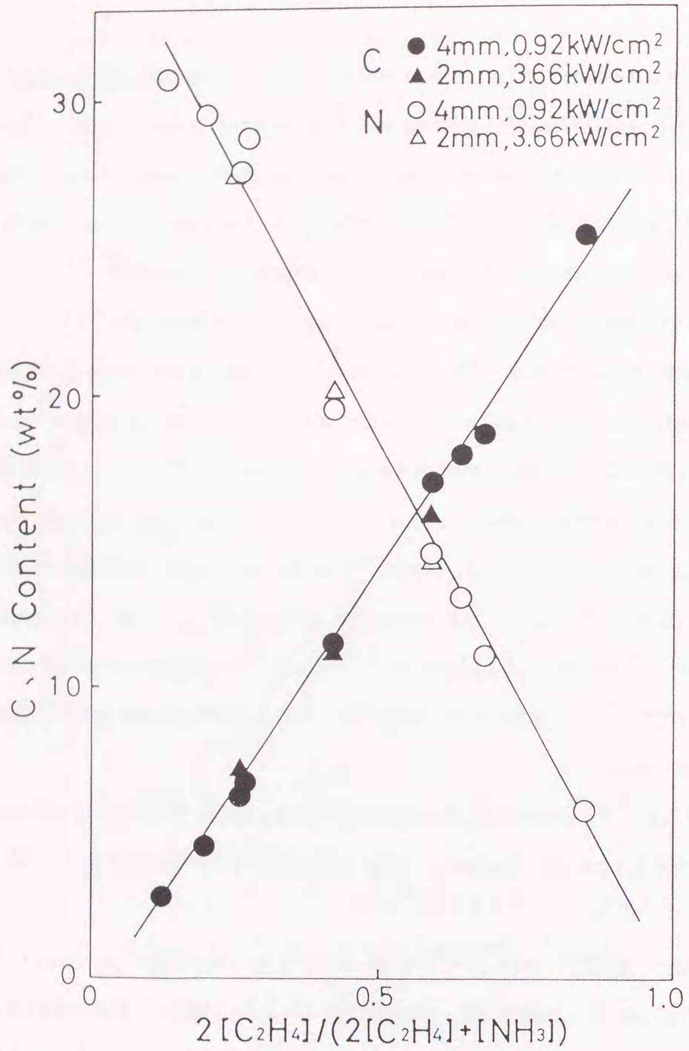

Fig. 3.2 Composition change of SiC–Si_3N_4 composite powder with C atomic ratio in the reactant gases ($2[C_2H_4]/(2[C_2H_4]+[NH_3])$).

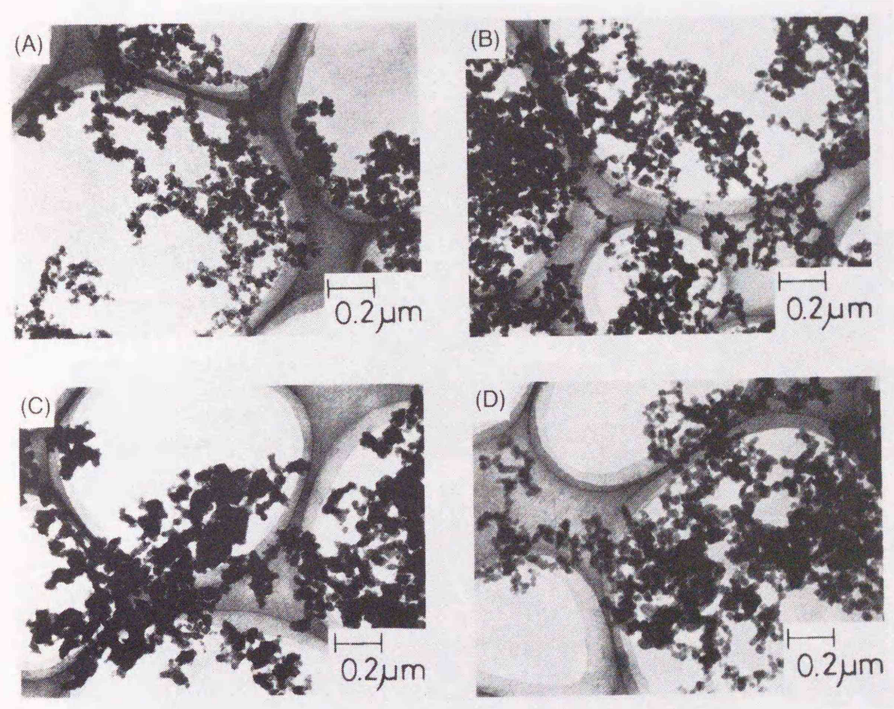

Fig. 3.3 TEM photos of SiC–Si_3N_4 composite ultrafine particles prepared by CO_2 laser (Beam diameter, 4 mm; laser power density, 0.92 kW/cm²).

(A) C_2H_4, 20 st. cm³/min, NH_3, 7 st. cm³/min (C, 25.3 wt%; N, 5.8 wt%)

(B) C_2H_4, 20 st. cm³/min, NH_3, 27 st. cm³/min (C, 16.9 wt%; N, 14.5 wt%)

(C) C_2H_4, 10 st. cm³/min, NH_3, 27 st. cm³/min (C, 11.5 wt%; N, 19.5 wt%)

(D) C_2H_4, 10 st. cm³/min, NH_3, 54 st. cm³/min (C, 6.7 wt%; N, 28.0 wt%)

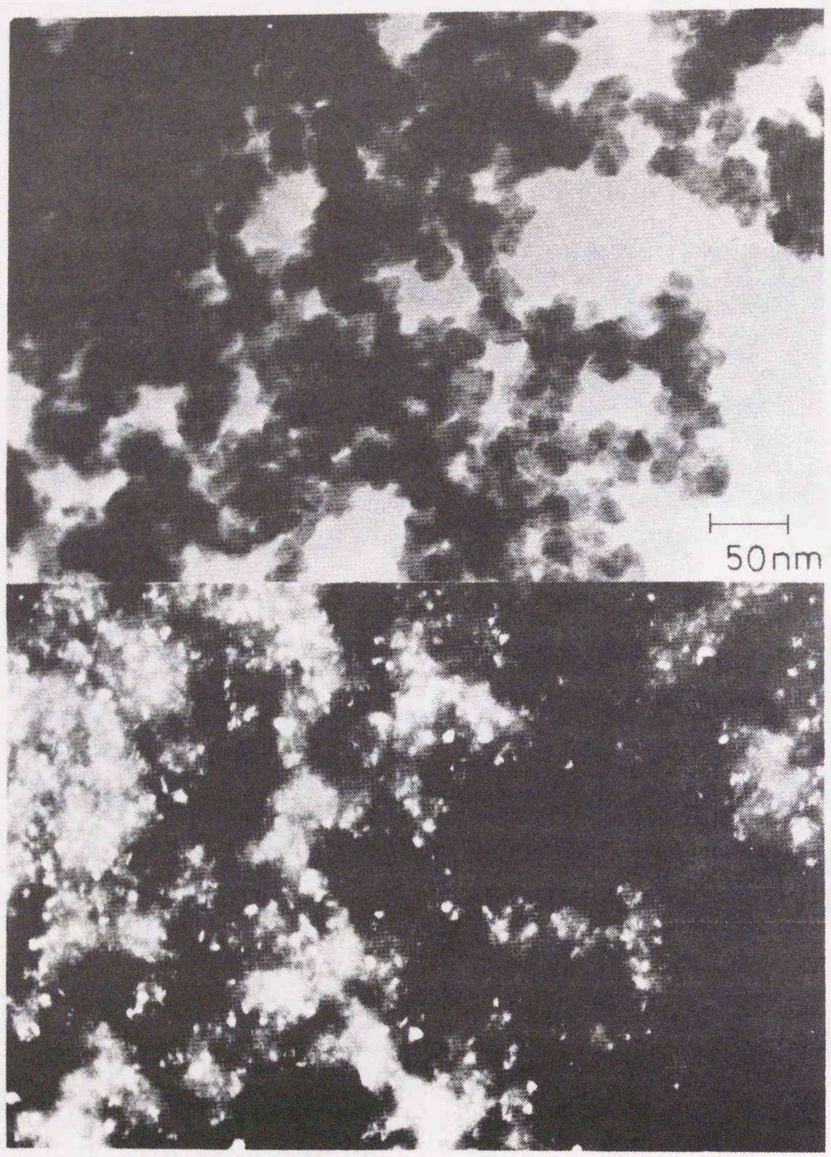

Fig. 3.4 Bright–field and dark–field images (SiC_{111}) of SiC–Si_3N_4 composite ultrafine particles: C, 25.3 wt%; N, 5.8 wt%, (Sample no. 12)

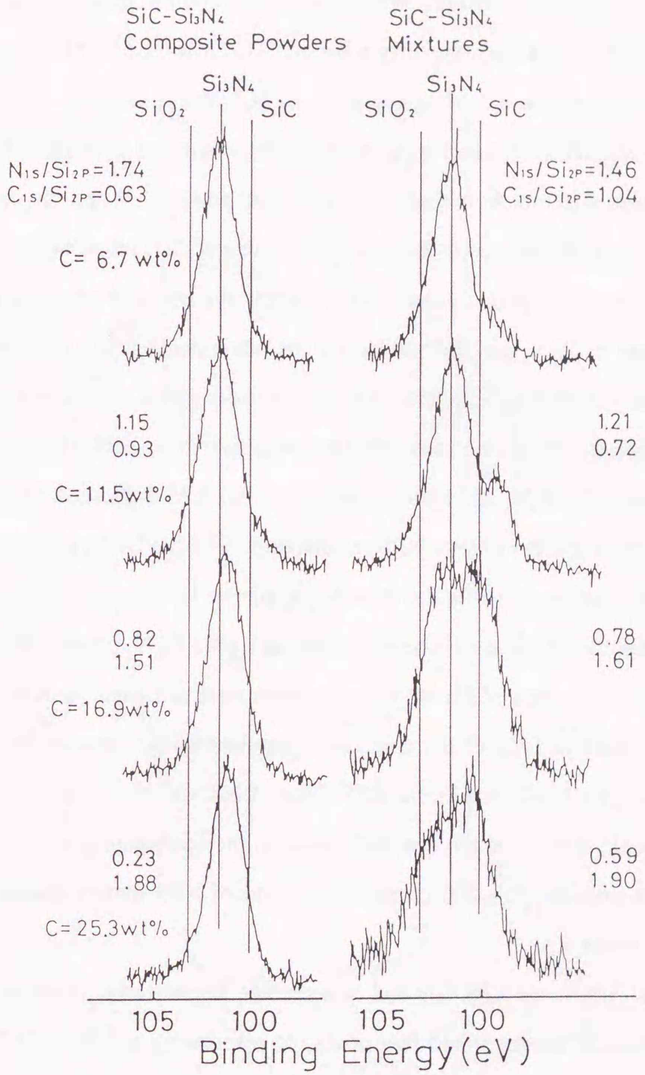

Fig. 3.5 Si2p XPS spectra of SiC–Si_3N_4 composite ultrafine powders prepared with a CO_2 laser and SiC–Si_3N_4 mixtures with different compositions.

heights depended on their compositions. In the case of SiC–Si_3N_4 composite powders synthesized with a laser, the XPS Si2p peak was a single peak, having a Si_3N_4 binding energy, irrespective of its composition. When the carbon content of the composite powder was 25.3 wt%, XRD showed only a broad SiC pattern, but XPS spectra showed a single Si2p peak with a binding energy of Si_3N_4, even if the binding energy slightly shifted toward SiC. This fact suggested that the chemical state of Si in the composite powder was different from that in the pure SiC powder. When the carbon content was 11.5 wt%, XRD showed that the powder contained SiC phase and a small amount of Si, Si_3N_4 and amorphous phase. XPS spectra showed a single Si2p peak with a binding energy of Si_3N_4 and did not have a SiC shoulder, while a mechanical mixture having similar XPS N1s/Si2p and C1s/Si2p intensity ratios exhibited a Si_3N_4 peak and a SiC shoulder. When the carbon content was 6.7 wt%, XRD showed that the powder contained SiC, Si_3N_4 and amorphous phase, and XPS Si2p showed only a Si_3N_4 peak. It was not clear from these XPS results alone whether Si_3N_4 phase in the composite powders was the same as the pure Si_3N_4 phase, because a Si_3N_4 phase including carbon might have the same chemical shift as a pure Si_3N_4 phase. Also the composition and chemical state of the amorphous phase were not clear by XPS. The fact that the XPS spectra of Si2p of the composite powders hardly showed the peak for the binding energy of SiC, while the XPS Si2p of SiC–Si_3N_4 mixture clearly included the SiC peak, suggested that the SiC phase in the composite powders was completely different from the pure SiC phase. Si2s peaks of XPS spectra showed the same trend as Si2p peaks.

Figure 3.6 and 3.7 show the XPS C1s and N1s spectra, respectively. XPS spectra of C1s of the mechanical mixtures had two peaks, corresponding to SiC (282.7 eV) and the contamination on the sample surface (graphite, 284.4 eV). When the carbon content of the powder was low, XPS C1s spectra of the composite powders were broad and consisted of two components of SiC and surface contamination (graphite). When the carbon content increased, XPS C1s was a broad peak situated at 283.9–

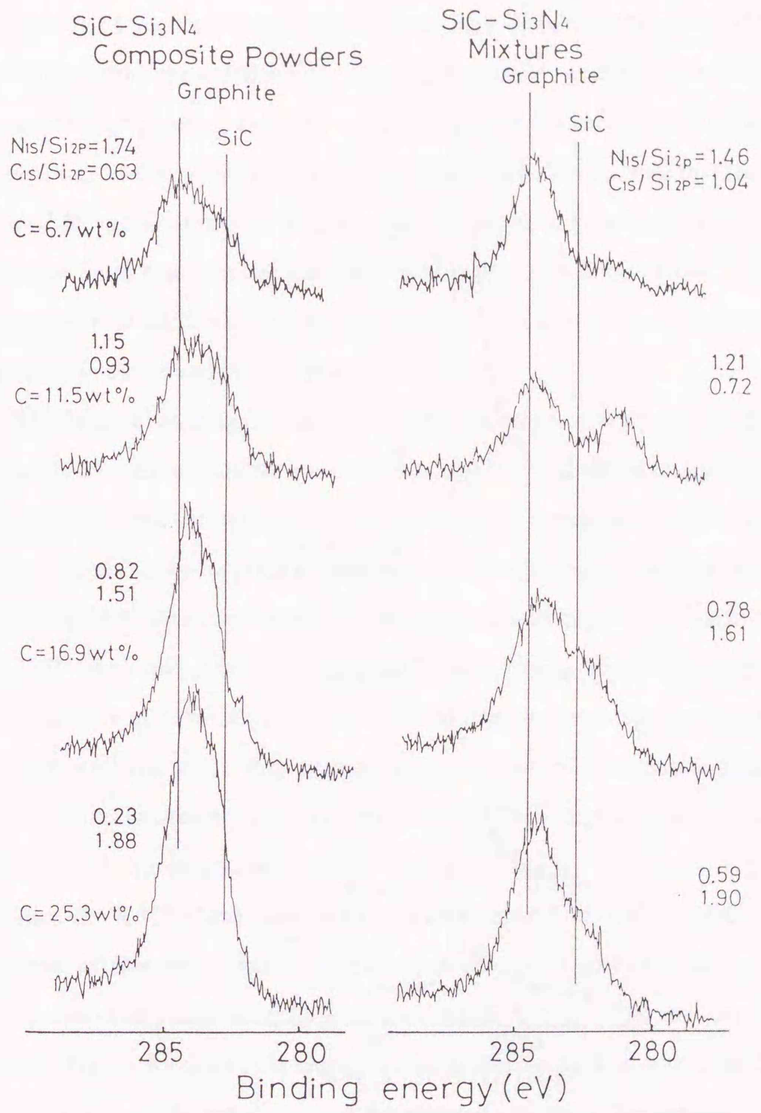

Fig. 3.6 C1s XPS spectra of SiC–Si_3N_4 composite ultrafine powders prepared with a CO_2 laser and SiC–Si_3N_4 mixtures with different compositions.

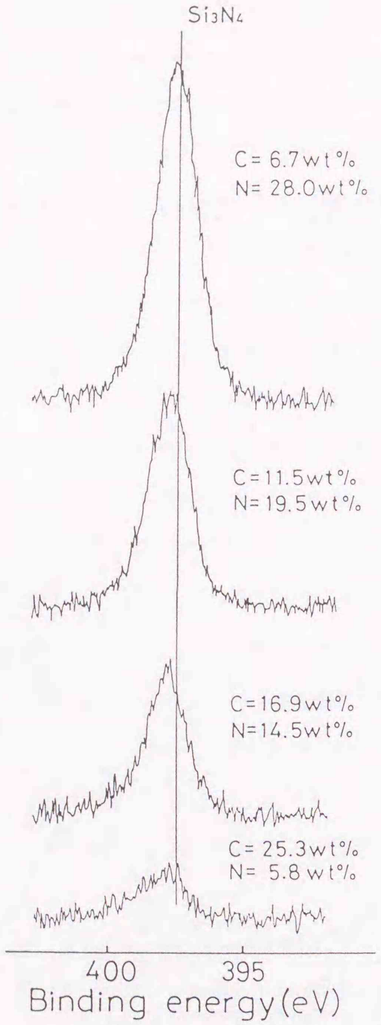

Fig. 3.7 N1s XPS spectra of $SiC–Si_3N_4$ composite ultrafine powders prepared with a CO_2 laser.

284.5 eV, which was closer to graphite than SiC. It was difficult to analyze the XPS C1s spectra, because they were greatly affected by surface contamination. The XPS N1s spectra of the composite powders were single peak at 397.6–397.7 eV, showing no variation with the composition. This peak position agreed well with the binding energy of Si_3N_4 (397.4 eV). XPS N1s spectra of the mechanical mixtures also showed the binding energy of Si_3N_4. The results of XPS showed that the chemical state of Si and C atoms in the $SiC–Si_3N_4$ composite powders were completely different from those in the mechanically mixed powders. These XPS results suggested that Si, C and N were intimately mixed in the composite powders, especially in the crystalline SiC phase.

The chemical shift appearing in the XPS spectra is mainly due to the electric charge distribution around the atoms. It was assumed that, in the composite powders, silicon atoms were surrounded by both nitrogen and carbon atoms, and the chemical shift of XPS Si2p was greatly affected by nitrogen atoms, which have higher electronegativity than carbon and silicon atoms. (electronegativity, C, 2.5; N, 3.0; Si, 1.8) [17] Therefore, XPS Si2p was a single peak having a binding energy of Si_3N_4. As for the N1s of XPS spectra, it was assumed that nitrogen atoms were bonded more strongly to silicon atoms than carbon atoms and that the peak positions of the XPS N1s were unchanged with the carbon content. This implied that nitrogen atoms occupied C sites substitutionally.

Since the XRD of the composite powders showed crystalline SiC and Si_3N_4 patterns, lattice constants can be determined. Lattice constants provide the information concerning the crystalline state, while XPS provides that concerning the surface. Figure 3.8 shows the change in the lattice constant of crystalline SiC in the $SiC–Si_3N_4$ composite powder versus the nitrogen content of the powder. The lattice constant of ultrafine SiC powder (4.356 Å), which was synthesized from SiH_4 and C_2H_4 by laser, agreed well with the data obtained from the literature (4.359 Å) [15]. As the nitrogen content increased, the lattice constant decreased rapidly and linearly.

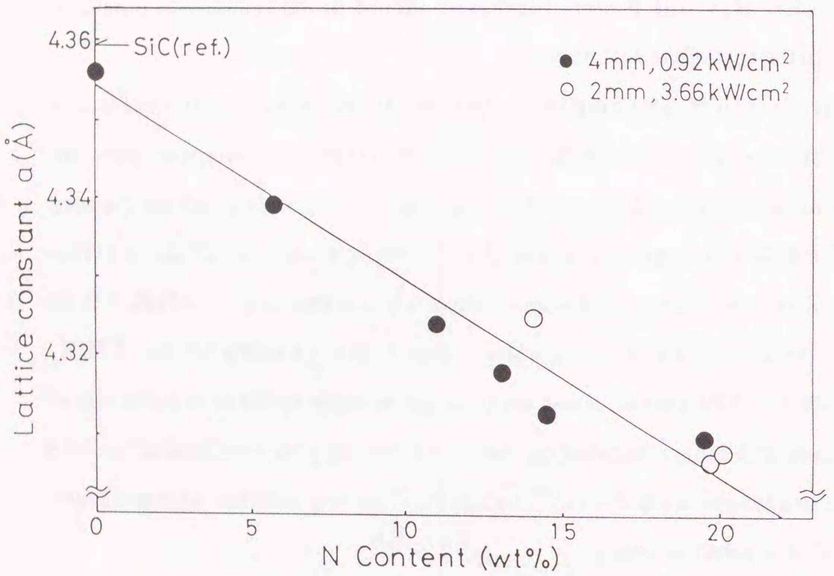

Fig. 3.8 Change of the lattice constant of crystalline SiC in the SiC–Si_3N_4 composite powder versus N content of the powder. The lattice constant was calculated from the (311) line and was corrected by highly pure Si (99.99%) as an internal standard.

It is well known that nitrogen can exist in SiC as a solid solution [18,19], and nitrogen atoms are considered to occupy carbon site [20]. Seo et al. [21] reported that the lattice constant of SiC decreased by solubilization of nitrogen into SiC. They reported that the lattice constant of β–SiC powder decreased from 4.359 A to 4.358 A by annealing β–SiC powder at 2173K for 0.5 h in N_2 atmosphere. However, the relationship between the amount of dissolved nitrogen and the lattice constant has been unclear. The decrease of the lattice constant in this report was extremely large compared to that reported by Seo et al. The atomic radii of nitrogen, carbon and silicon are 0.070, 0.077 and 0.117 nm, respectively [17]. The representative bond length was 0.188 nm for the Si–C bond and 0.173 nm for Si–N. Nitrogen atoms have smaller atomic radii and shorter bond length to silicon atoms than carbon atoms. The contraction of the SiC lattice might be explained by the formation of substitutional solid solution of nitrogen in SiC.

When the nitrogen content became higher than 20 wt%, the crystalline SiC decreased and crystalline Si_3N_4 appeared. It became impossible to define the SiC lattice constant, because XRD peaks of SiC and Si_3N_4 overlapped each other. The lattice constants of crystalline Si_3N_4 in the SiC–Si_3N_4 composite powders with the nitrogen content above 20 wt% are shown in Table 3.2. The lattice constants of the c–axis were almost the same as those in the reference [16] in the case of both α– and β–Si_3N_4. However, the lattice constants of the a–axis of the composite powders were larger than those in the reference. The expansion of Si_3N_4 lattice implied that carbon atoms dissolved into the crystalline Si_3N_4, since the atomic radius of carbon is larger than that of nitrogen.

Figure 3.9 shows an EELS spectrum for particles having a crystalline SiC structure. We can know the composition of the particles EELS measurements. If one particle could exist solely in the field of a few microns, which was corresponding to the space resolution of EELS, we could know the composition of one particle by EELS measurement. However, these particles had smaller particle size than the space

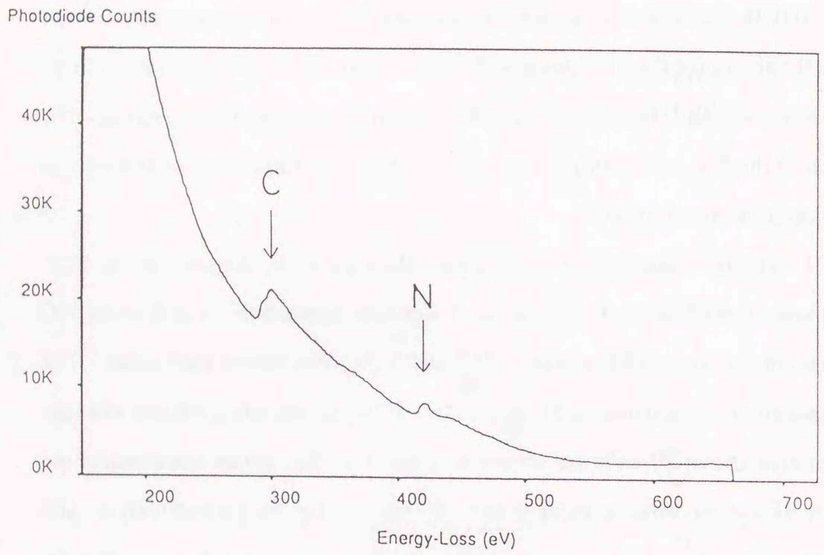

Fig. 3.9 EELS spectrum of particles having a crystalline SiC structure in a SiC–Si_3N_4 composite ultrafine powder.

Table 3.2 Lattice constants of crystalline Si_3N_4 in the SiC–Si_3N_4 composite powder. Lattice constants were calculated from the (411) and (004) lines for α–Si_3N_4 and from the (212) and (002) lines for β–Si_3N_4 and were corrected by highly pure Si (99.99%) as an external standard.

Sample no.	Lattice constant (Å)				Composition		
	α–Si_3N_4		β–Si_3N_4		C	N	O
	a	c	a	c		(wt%)	
18	7.779	5.624	7.607	2.911	6.5	27.6	0.8
19	7.780	5.624	7.628	2.910	4.5	29.5	1.3
20	7.780	5.624	7.632	2.909	2.8	31.0	0.8
ref.[16]	7.758	5.623	7.6044	2.9075	–	–	–

resolution of EELS and were always agglomerated each other. It was impossible to analyze the composition of one particle by EELS. Therefore, EELS spectra were taken for the field, in which similar particles having the SiC structure were gathered. These EELS spectra had both carbon and nitrogen peaks. It was confirmed that nitrogen existed inside a particles having the SiC structure. In addition, small amounts of amorphous particles were found in several composite powders by TEM observation and EELS spectra of these amorphous particles showed that they contained Si, C and N.

The amount of dissolved nitrogen in a SiC–N solid solution has not been studied precisely, but Kamath [19] has reported that the nitrogen content of solid solution is at most about 0.3 wt%. In this research, nitrogen dissolved in cubic SiC crystals was obtained, when a composite powder contained a great deal of carbon and less nitrogen. The exact amount of nitrogen inside the SiC crystals has not been clearly measured, but considering the change of the lattice constant and the total nitrogen content and the particle homogeneity (for example, sample no. 12 contained 25.3 wt% C and 5.8 wt% N and consisted of uniform particles having a SiC structure) it was likely that the amount of dissolved nitrogen was larger than that reported [19]. In this experiment, the reaction flame was 5–7 mm, and a typical residence time of the reactant in the flame was 10–30 msec. This laser method involved a very quick heating and quenching process. Such a quick heating and quenching process make it possible to obtain SiC microcrystals dissolving a great deal of nitrogen.

3.4. Conclusion

(1) SiC–Si_3N_4 composite ultrafine particles were synthesized by irradiating a SiH_4, C_2H_4, NH_3 gas mixture with a CO_2 laser at atmospheric pressure. The composition of the composite powder could be controlled by changing the C_2H_4, NH_3 flow rate.

(2) The crystalline state of the composite powder changed with its composition. The composite powder, which contained much carbon, was β–SiC. As the nitrogen

content of the powder increased, β–SiC decreased and the amorphous phase and α –Si_3N_4, β–Si_3N_4, Si appeared.

(3) The results of XPS, lattice constant and EELS measurements showed that Si, C, N atoms were intimately mixed in the composite particles. The SiC phase in the composite powder dissolved much nitrogen. The Si_3N_4 phase in the composite powder also dissolved carbon. This mutual solubility was caused by the rapid–heat and rapid–quench process of the laser–induced gas phase reaction.

References

1. W.R. Cannon, S.C. Danforth, J.H. Flint, J.S. Haggerty and R.A. Marra, "Sinterable Ceramic Powders from Laser-Driven Reactions: Process Description and Modeling", J. Am. Ceram. Soc., 65(7), 324-30 (1982).
2. W.R. Cannon, S.C. Danforth, J.S. Haggerty and H.K. Bowen, "Sinterable Ceramic Powders from Laser-Driven Reactions: Powder Characteristics and Process Variables", ibid, 65(7), 330-35 (1982).
3. Y. Suyama, R.A. Marra, J.S. Haggerty and H.K. Bowen, "Synthesis of Ultrafine SiC Powders by Laser-Driven Gas Phase Reactions", Am. Ceram. Soc. Bull., 64(10), 1356-59 (1985).
4. K. Sawano, J.S. Haggerty and H.K. Bowen, "Formation of SiC Powder from Laser Heated Vapor Phase Reactions", Yogyo Kyokai-shi 95(1), 64-69 (1987).
5. M. Cauchetier, O. Croix and M. Luce, "Laser Synthesis of Silicon Carbide Powders from Silane and Hydrocarbon Mixtures", Adv. Ceramic Mater., 3, 548-52 (1988).
6. M. Suzuki, Y. Nakata, T. Okutani and A. Kato, "Preparation of SiC Ultrafine Particles by Using CO_2 Laser", Seramikkusu Ronbun-shi, 97, 972-75 (1989).
7. W. Symons and S.C. Danforth, "Synthesis and Characterization of Laser-Synthesized Silicon Nitride Powders", pp 249-56 in Advances in Ceramics, Vol. 21, Edited by G.L. Messing, K.S. Mazdiyasni, J.W. McCauley and R.A. Haber, Am. Ceram. Soc., Westerville, OH., 1987.
8. M. Aoki, J.H. Flint and J.S. Haggerty, "Synthesis of Non-Agglomerated Si_3N_4 Powder", pp253-60 in Ceramic Transactions, Vol. 1, Ceramic Powder Science II, Edited by G.L. Messing, E.R. Fuller Jr. and H. Hausner, Am. Ceram. Soc., Westerville, OH., 1988.
9. G.W. Rice, "Laser Synthesis of Si/C/N Powder from 1,1,1,3,3,3-Hexamethyldisilazane", J. Am. Ceram. Soc., 69(8), C183-C185 (1986).
10. M. Cauchetier, O. Croix, M. Lance, C. Robert and M. Luce, "Laser Synthesis and Characterization of Ultrafine Si/C/N Powders", Proceedings of 1st. European Ceramic Society Conf. pp18-22, (1989).
11. A.K. Knudsen "Laser Driven Synthesis and Densification of Ultrafine Boron Carbide Powders", pp 237-47 in Advances in Ceramics, Vol. 21, Edited by G.L. Messing, J.S. Mazdiyasni, J.W. McCauley and R.A. Haber, Am. Ceram. Soc., Westerville, OH., 1987.
12. A. Gupta and J.T. Yardley, "Production of Light Olefins from Synthesis Gas Using Catalysts Prepared by Laser Pyrolysis", pp 131-39 in SPIE 458, Applications of Lasers to Industrial Chemistry, 1984.
13. F.F. Lange, "Effect of Microstructure on Strength of Si_3N_4-SiC Composite System" J. Am. Ceram. Soc., 56(9), 445-50 (1973).
14. G.W. Rice and R.L. Woodin, "Kinetics and Mechanism of Laser-Driven Powder Synthesis from Organosilane Precursors", J. Mater. Res., 4(6), 1538-48 (1989).
15. JCPDS Card No. 29-1129, International center for diffraction data, Swarthmore, PA.
16. JCPDS Card No. 9-250, No. 33-1160, International center for diffraction data, Swarthmore, PA.
17. L. Pauling, "The Nature of Chemical Bond", 3rd Ed., Cornell University Press (1960).
18. R.F. Davis, "Interrelationships among Nonstoichiometry, Impurity Substitution, and Polytypism in Silicon Carbide" pp477-97 in Advances Ceramics, Vol.23, Am. Ceram. Soc., Westerville, OH., 1987.
19. G.S. Kamath, "Some Observation on Silicon Carbide Single Crystal Growth", Mat. Res. Bull., 4, S57-S66 (1969).
20. G.E.G. Hardeman, "Electron and Nuclear Spin Resonance in n-Type Silicon Carbide", J. Phys. Chem. Solids, 24, 1223-31 (1963).
21. W-S. Seo, C-H. Pai, K. Koumoto and H. Yanagida, "Microstructure Development and Stacking Fault Annihilation in β-SiC Powder Compact",

Seramikkusu Ronbun-shi, 99, 443-47 (1991).

22. J. Hojo, M. Nakamine and A. Kato,"Preparation of SiC-Si_3N_4 Composite Particles by Plasma Gas Phase Reaction", Ceramic Transactions I, Am. Ceram. Soc. Inc., 277-84, (1988)

CHAPTER 4

SILICON-29 MAGIC ANGLE SPINNING NMR AND ESR STUDIES ON THE LOCAL STRUCTURE OF SILICON CARBIDE - SILICON NITRIDE COMPOSITE ULTRAFINE PARTICLES SYNTHESIZED BY LASER-INDUCED GAS-PHASE REACTION METHOD

Chapter 4

Silicon–29 Magic Angle Spinning NMR and ESR Studies on the Local Structure of Silicon Carbide – Silicon Nitride composite Ultrafine Particles Synthesized by Laser–Induced Gas–Phase Reaction Method

4.1 Introduction

High–resolution solid–state magic angle spinning nuclear magnetic resonance (MAS–NMR) spectroscopy has become a powerful and popular tool for investigating the local structures of solid materials. Most of the applications to date have been in organic systems such as polymers. Recently, the MAS–NMR has found new applications in solid inorganic systems such as silicate and zeolite [1]. In addition, this technique is also useful for the study of non–oxide materials [2,3].

In the last few years, a number of NMR investigations about the structure of SiC and Si_3N_4 have been reported. Most of them were concerned with well–known structures such as α– and β–SiC and α– and β–Si_3N_4 and their polytypes [4–10]. Other studies were done to characterize the commercial products [5,11,12] and to investigate the behavior of boron used as a sintering aid for SiC [13]. These studies revealed that high resolution solid state NMR was a powerful and useful method for the study of ceramic materials, because of its high sensitivity to the local structure. Moreover, NMR is a bulk analysis technique. Information can be obtained with regard to the local structure over the entire sample under study, which is notably different from other surface analysis methods such as X–ray photoelectron spectroscopy (XPS).

In chapter 3, the synthesis of silicon carbide–silicon nitride (SiC–Si_3N_4) composite ultrafine particles was studied. The results of XPS, lattice constant measurement and electron energy loss spectroscopy (EELS) have indicated that Si, C and N atoms were intimately mixed in the composite powder. In this chapter, the ^{29}Si MAS–NMR technique was applied to clarify the local structure of the SiC–Si_3N_4 particles and

ESR was applied to get the information of paramagnetic defects in the particles.

4.2 Experimental Procedure

The powders were synthesized by irradiating SiH_4, C_2H_4, NH_3 gas mixtures with CO_2 laser at atmospheric pressure. The synthesis of the powders was described in chapter 3 in detail. In this study, NMR spectra were taken for the powders prepared at a laser power density of 0.92 kW/cm^2 and beam diameter of 4 mm.

The crystalline phases of the powders were analyzed by X-ray diffraction (XRD) and the mean crystalline sizes were determined by the line width of diffraction line.

Solid-state ^{29}Si MAS-NMR spectra were acquired at 53.7 MHz using a JNM-GX270 spectrometer (JEOL). The samples were packed into 17 mm x 5 mm diameter zirconia rotars with polyimide endcaps. The spinning speed was between 5.7 and 6.2 kHz. The spectra were obtained following 90° pulse (pulse width: 4.5 μs). All the chemical shifts were quoted relative to the signals for tetramethylsilane, although secondary external reference (poly-dimethylsilicone, -22 ppm) was also used. The line width (FWHM) was determined from the spectra without broadening factor, while the spectra with broadening factor were shown in the figures to improve S/N ratio. The spin-lattice relaxation time (T_1) was defined by nonlinear inversion recovery (IR) method [16]. T_1 was measured for the several representative samples, and were in the range from 9.0 to 49.5 s. It was considered that a relaxation delay of 5 times T_1 was long enough for the resulting spectra to be quantitatively representative of the sample [4]. Even though T_1 values for all samples were not measured, it was unlikely that T_1 value of other unmeasured samples showed a much greater than 49.5 s. Therefore, pulse delay (PD) of 300 s was considered to be long enough to get the quantitatively representative spectra. Most NMR spectra were taken at a pulse delay of 400 s to ensure that the spectra represented the information on the entire samples quantitatively. In some cases, PD = 60 and 300 s were used to save measuring time. In any case, the condition of a relaxation delay of 5 times T_1 was

satisfied.

ESR spectra were obtained using JES-FE3X spectrometer (JEOL) with a standard rectangular x-band cavity at 303 K. The samples of 3 to 15 mg were used for ESR measurement. The microwave power was 0.2 mW and it was confirmed that ESR signal was not saturated at 0.2 mW by changing the microwave power. The spin concentrations of the powders were measured using 0.25 mg solid DPPH as a standard.

Fourier transform photoacoustic emission spectra (FT-PAS) of the powders were obtained using FTS-65 (Bio-RAD) spectrometer.

4.3 Results

4.3.1 NMR

4.3.1.1 SiC and composite particles of low N content

Figure 4.1 shows the ^{29}Si NMR spectra of ultrafine SiC powder synthesized using the laser and the change of the spectra by introducing nitrogen into SiC powder. The NMR spectrum of ultrafine SiC powder exhibited one main peak (-15.9 ppm) and two shoulders (-20.3, -24.8 ppm). The main peak position agreed well with that of β-SiC and the positions of two shoulders agreed well with those of α-SiC [9,10]. While X-ray diffraction (XRD) pattern showed only a broad β-SiC pattern (Fig. 4.3), the NMR spectra indicated that the ultrafine SiC powder consisted of mainly β-SiC and small quantity of α-SiC. The line width (FWHM) of the main peak at -15.9 ppm, which was determined without precise peak deconvolution, was approximately 3.0 ppm. The spin-lattice relaxation time, T_1 was estimated to be 18.8 s for the ultrafine SiC powder.

Figure 4.2 shows the ^{29}Si NMR spectra of low nitrogen content SiC-Si_3N_4 powders. Figure 4.3 shows the XRD patterns of these powders. The XRD patterns of these powders were similar and showed broad β-SiC patterns. A very small and

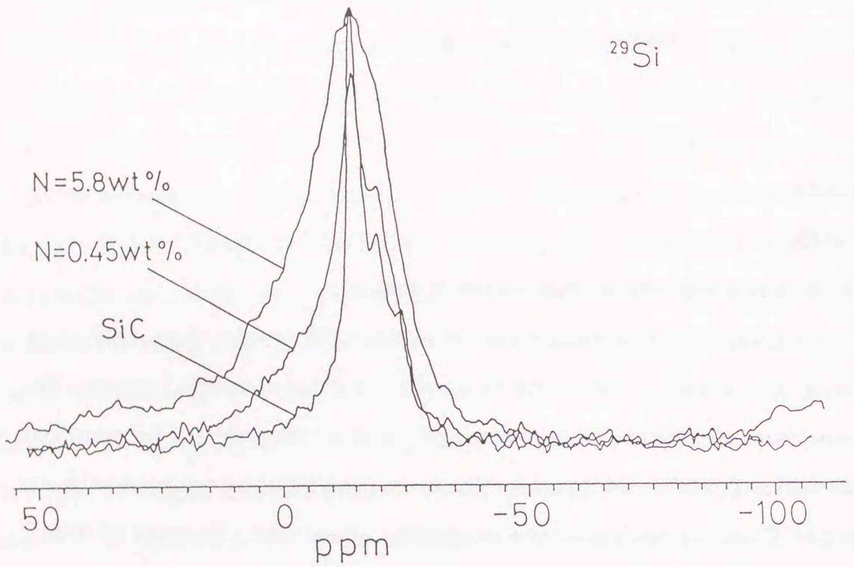

Fig. 4.1 ^{29}Si NMR spectrum of ultrafine SiC powder synthesized by laser and the change of ^{29}Si NMR spectra by introducing nitrogen into SiC powder. The spectra were taken at the following condition;

SiC; a pulse delay (PD) of 400 s, line broadening (LB) of 20 Hz and 148 scans.

N = 0.45 wt%; PD = 60 s, LB = 10 Hz, 200 scans

N = 5.8 wt%; PD = 400 s, LB = 50 Hz, 168 scans

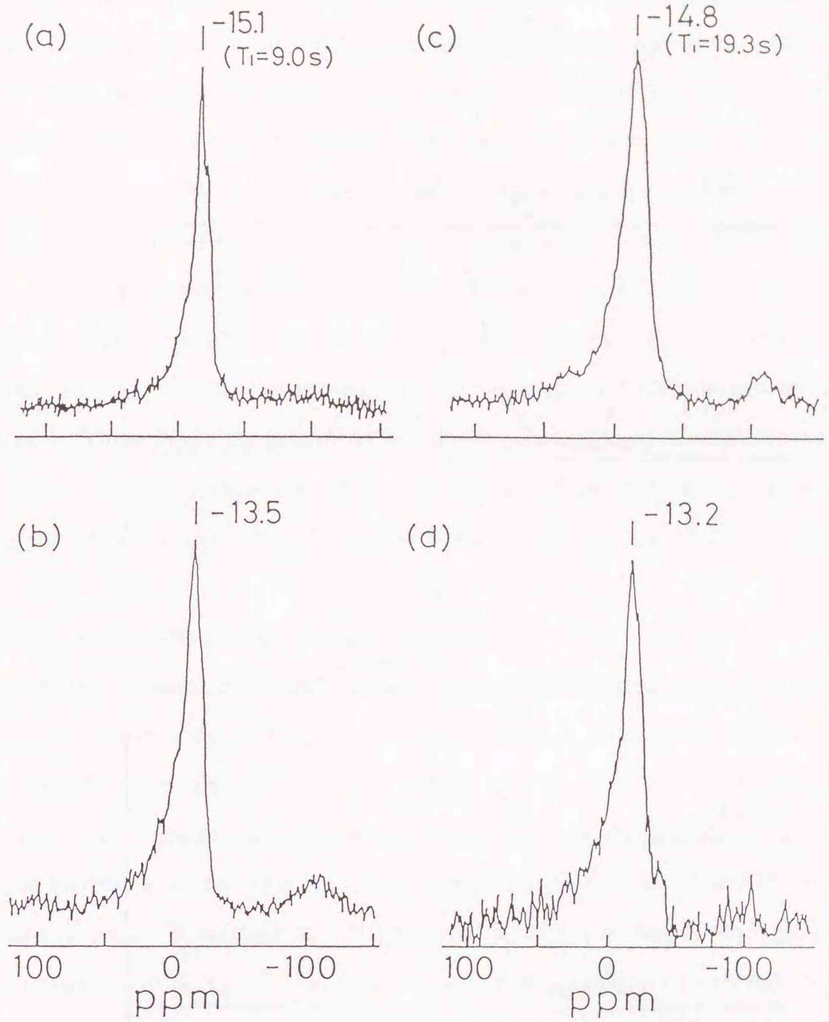

Fig. 4.2 ^{29}Si NMR spectra of low N content SiC–Si_3N_4 composite powders synthesized using a laser.

(a) N = 0.45 wt%, C = 27.0 wt%, PD = 60 s, LB = 10 Hz, 200 scans

(b) N = 2.6 wt%, C = 27.2 wt%, PD = 400 s, LB = 50 Hz, 269 scans

(c) N = 5.8 wt%, C = 25.3 wt%, PD = 400 s, LB = 50 Hz, 168 scans

(d) N = 10.3 wt%, C = 19.5 wt %, PD = 400 s, LB = 50 Hz, 168 scans

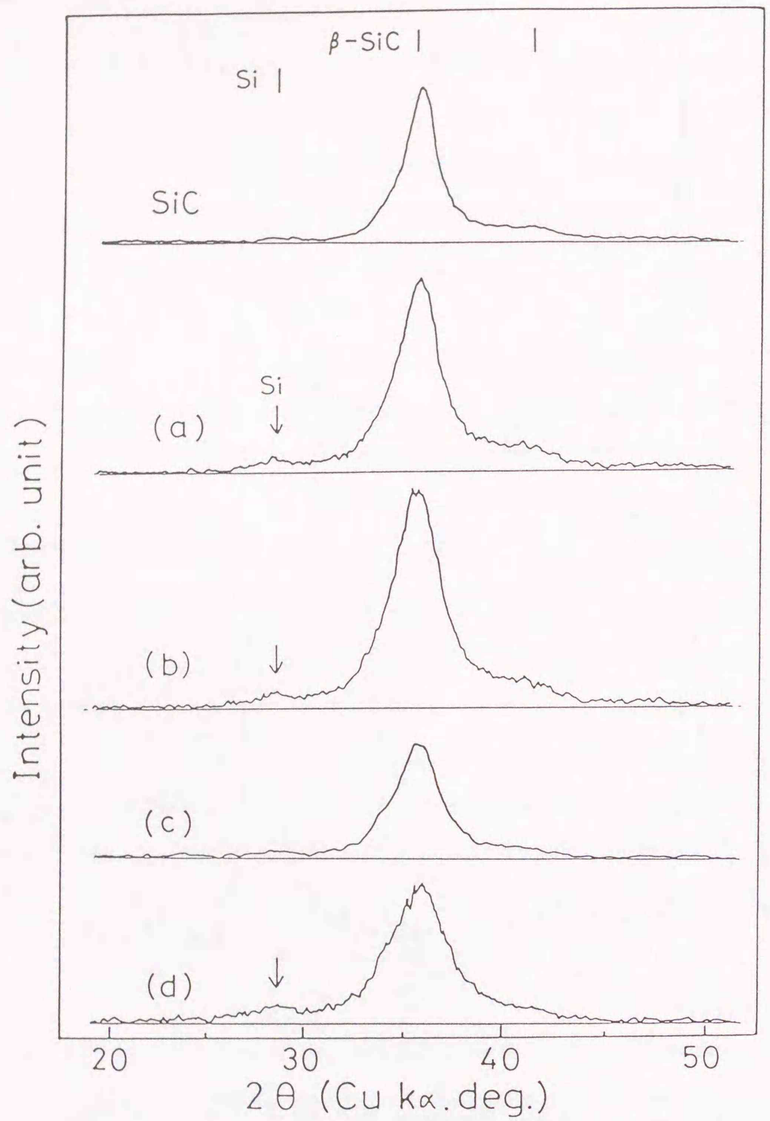

Fig. 4.3 X-ray diffraction patterns of SiC ultrafine powder and low nitrogen content $SiC-Si_3N_4$ composite powders synthesized using a laser.
(a) N = 0.45 wt%, C = 27.0 wt% (b) N = 2.6 wt%, C = 27.2 wt% (c) N = 5.8 wt%, C = 25.3 wt% (d) N = 10.3 wt%, C = 19.5 wt%

broad peak of Si was observed in powders of various N contents (Fig. 4.3 (a),(b),(d)). The NMR spectrum of $SiC-Si_3N_4$ composite powder with nitrogen content of 0.45 wt% (Fig. 4.2 (a)) was similar to that of ultrafine SiC powder (Fig. 4.1). It exhibited a main peak at −15.1 ppm and one shoulder peak at −19.9 ppm, while the ultrafine SiC showed two shoulder peaks. The component of low magnetic field (between −5 and +30 ppm) increased compared to the case of ultrafine SiC powder. In the case of the powders with nitrogen content of 2.6, 5.8, 10.3 wt% (Fig. 4.2 (b),(c),(d)), the NMR spectra were very similar to each other. They exhibited a main peak between −14.8 and −13.2 ppm and had broad components at low magnetic field (between −5 and +30 ppm). These NMR spectra of the composite powders showed small broad peaks around −100 ppm, which came from silica of the surface oxide layer. The T_1 values of the NMR peaks were 9.0 s for 0.45 wt% nitrogen content and 19.3 s for 5.8 wt%.

4.4.1.2 Composite particles of high N content

Figure 4.4 shows ^{29}Si NMR spectra of high nitrogen content $SiC-Si_3N_4$ powders. Figure 4.5 shows their XRD patterns. Crystalline Si_3N_4 phase clearly appeared above 19.5 wt%. The XRD pattern of the powder of Fig. 4.5(a) showed a broad β−SiC pattern including very small amorphous component, which was observed as a base line increase at a very wide range from about 20 to 45 degrees. The NMR spectrum showed a main broad peak at −19.3 ppm and a small shoulder at −46.7 ppm, which corresponds to Si_3N_4 [6]. The low magnetic field component (between −5 and 30 ppm) became very small. The XRD pattern of the powder of Fig. 4.5(b) was the mixture of broad β−SiC pattern, crystalline Si_3N_4, small Si peak and a small amount of amorphous component. The NMR spectrum showed a broad peak at −18.7 ppm and a relatively sharp peak at −48.3 ppm (FWHM, approximately 10 ppm). In addition, it contained a small peak at −80.8 ppm and around −110 ppm, which corresponded to elementary silicon and silica, respectively. As the nitrogen content increased and reached 28.0 wt% (Fig 4.5(c)), crystalline Si_3N_4 increased and SiC

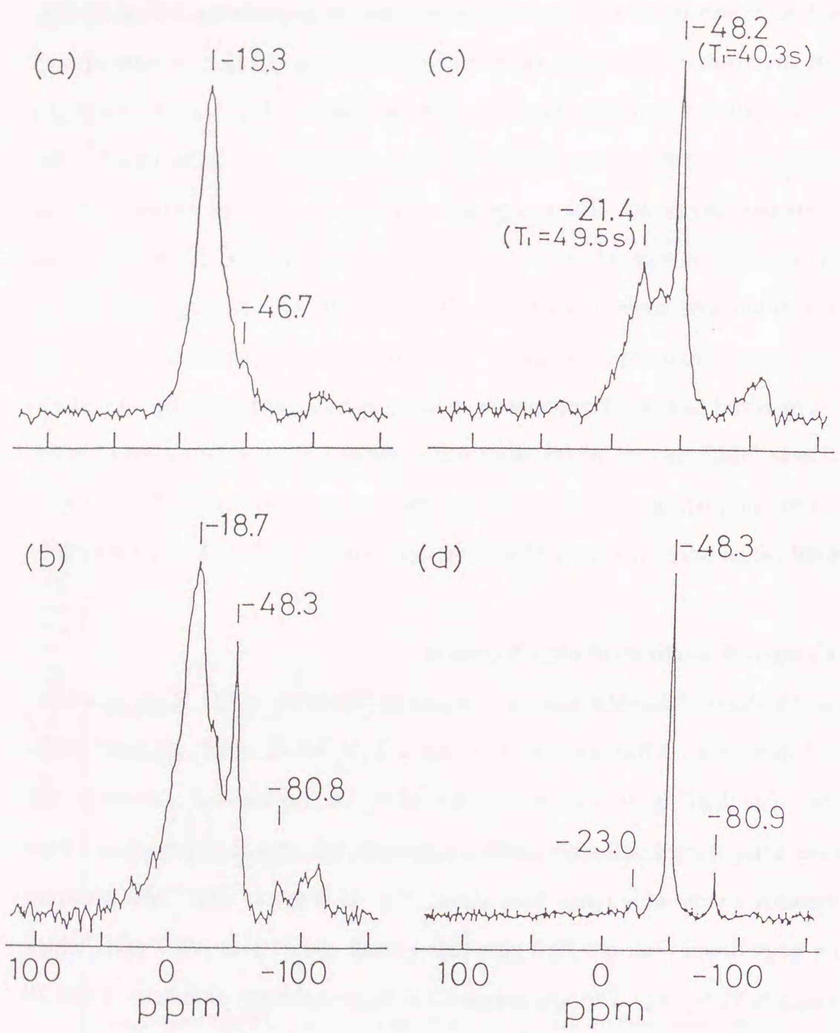

Fig. 4.4 ^{29}Si NMR spectra of high nitrogen content SiC–Si_3N_4 composite powders synthesized using a laser.

(a) N = 13.1 wt%, C = 17.9 wt%, PD = 300 s, LB = 50 Hz, 160 scans

(b) N = 19.5 wt%, C = 11.5 wt%, PD = 400 s, LB = 50 Hz, 200 scans

(c) N = 28.0 wt%, C = 6.7 wt%, PD = 400 s, LB = 50 Hz, 100 scans

(d) N = 30.9 wt%, C = 2.8 wt%, PD = 300 s, LB = 10 Hz, 60 scans

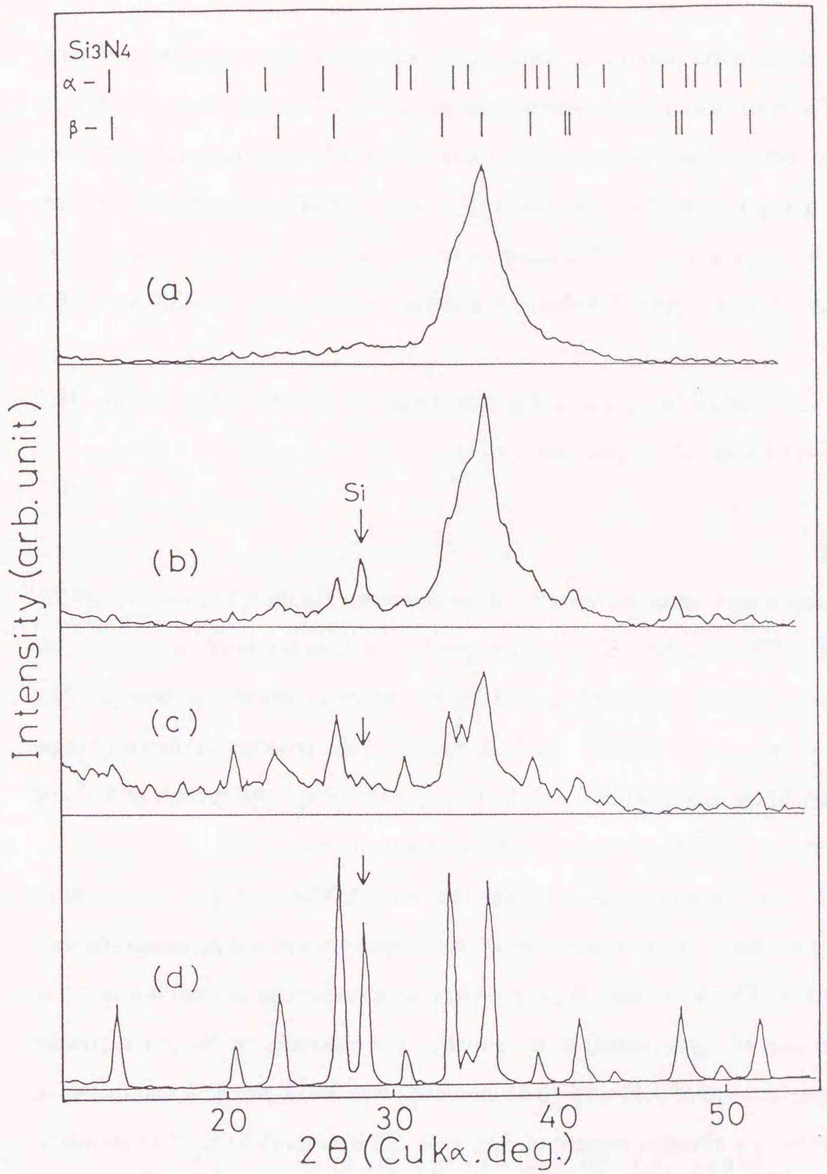

Fig. 4.5 X–ray diffraction patterns of high nitrogen content SiC–Si_3N_4 composite powders.

(a) N = 13.1 wt%, C = 17.9 wt% (b) N = 19.5 wt%, C = 11.5 wt%, (c) N = 28.0 wt%, C = 6.7 wt% (d) N = 30.9 wt%, C = 2.8 wt%

decreased in the XRD pattern. In addition, an amorphous phase was observed more clearly. The NMR spectrum showed that the peak at −21.4 decreased and the peak at −48.2 ppm increased and became a little sharper (FWHM, approximately 6.3 ppm). When the nitrogen content was 30.9 wt% (Fig. 4.5(d)), XRD pattern was the mixture of sharp α–Si_3N_4 and β–Si_3N_4 diffraction pattern and Si. The NMR spectrum showed a sharp peak at −48.3 ppm (FWHM, 3.6 ppm) and small peaks at −23.0 and −80.9 ppm.

The T_1 values of the two peaks in Fig. 4.4(c) were estimated to be 40.3 s for −48.2 ppm, and −49.5 s for −21.4 ppm, respectively.

4.3.2 ESR

ESR spectra were taken for these ultrafine powders. Figure 4.6 shows the typical ESR spectra of SiC and SiC–Si_3N_4 composite ultrafine powders synthesized using the laser. These powders showed strong ESR signals, which indicated that these powders had many paramagnetic defects. The ESR spectra of the powders exhibited a single line shape without any satellites and shoulders, even though the spectra of SiC and low nitrogen content SiC–Si_3N_4 were somewhat asymmetric.

Table 4.1 lists the g value, peak to peak line width (ΔHpp) and spin concentration (Ns). No correlation could be drawn between nitrogen content and paramagnetic spin concentration. The Ns of SiC–Si_3N_4 powders were smaller by at least one order of magnitude than nitrogen content of the powder. For example, the Ns of the powder with nitrogen content of 0.45 wt% (0.66 atomic%) was 0.037 atomic% and the Ns of the powder with a nitrogen content of 30.9 wt% (45.8 atomic%) was 0.13 atomic%. This fact revealed that most of the nitrogen in the composite powders was present in a nonparamagnetic form.

4.4 Discussion

4.4.1 NMR

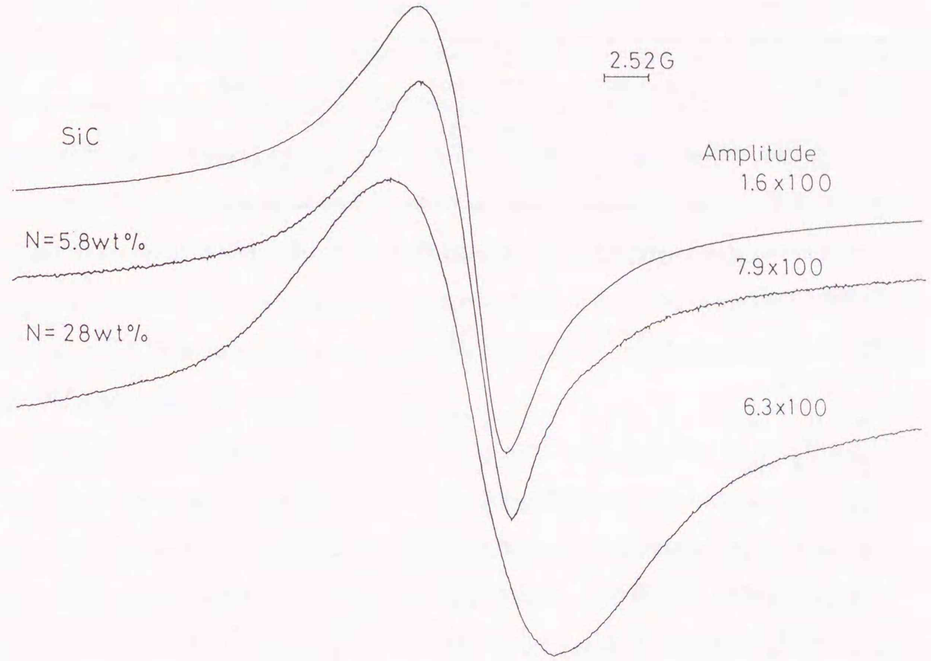

Fig. 4.6 Typical ESR spectra of SiC and SiC–Si_3N_4 ultrafine composite powders synthesized using a laser. microwave power: 0.2 mW, modulation: 100 kHz, 0.4 G temperature: 303 K

Table 4.1 g value and spin concentration and peak to peak line width of ESR spectra of SiC and SiC–Si_3N_4 composite powders

Sample	g value	Spin conc. (spins/g)	Peak to peak line width Δ Hpp, (G)
SiC (commercial)	2.0026	1.0×10^{18}	4.6
SiC	2.0027	1.1×10^{19}	5.1
SiC–Si_3N_4			
N = 0.45 wt%	2.0030	1.1×10^{19}	5.4
N = 5.8 wt%	2.0025	1.9×10^{18}	4.9
N = 11.0 wt%	2.0026	4.8×10^{18}	5.6
N = 13.1 wt%	2.0026	3.4×10^{18}	5.0
N = 19.5 wt%	2.0025	8.9×10^{17}	8.5
N = 28.0 wt%	2.0025	1.9×10^{19}	8.5
N = 30.9 wt%	2.0025	3.9×10^{19}	10.5

4.4.1.1 SiC and composite particles of low N content

Carduner et al. [11] have studied seven commercial β–SiC powders. From the results of Carduner, it seemed that there were typically two kinds of powders. One kind of powder showed broader NMR spectra (FWHM 5 to 6 ppm) with peak maxima at about –18 to –19 ppm. The other kind of powder showed a relatively narrow peak (FWHM 0.8 ppm) with peak maxima at –16 ppm. They showed that the existence of stacking faults broadened the spectra and shifted the peak position toward a high magnetic field. But this laser synthesized SiC powder seemed to be different type from those reported by Carduner, because it showed a relatively broad (FWHM, approximately 3.0 ppm) peak at –15.9 ppm. This laser synthesized SiC powder consisted of very fine particles and the mean crystalline size was 4.4 nm. This powder might have many defects besides stacking faults, or contain amorphous phase. Crystal imperfections as well as amorphous phase seemed to broaden the NMR spectrum [5]. The very similar spectra were observed in polymer derived SiC [17] and SiC based materials [18].

The spin–lattice relaxation time, T_1 was estimated to be 18.8 s for the ultrafine SiC powder. In general, NMR relaxation time is dependent on molecular motion, but in the case of solid systems molecular motion is not vigorous enough to be efficient. Therefore, silicon carbide generally has long T_1 values. The longest T_1 value of 35 ± 4 min was reported for highly pure 6H–SiC [4]. The laser synthesized ultrafine SiC as well as SiC–Si_3N_4 composite ultrafine powders showed very short T_1 values. The ultrafine powders had many paramagnetic defects, which are shown in the ESR results. Because the relaxation probably occurred via paramagnetic centers [4,12], these ultrafine powders showed short T_1 values.

It was interesting to obtain MAS–NMR spectra at different relaxation delays, because it was expected that the species in the vicinity of paramagnetic centers would show faster relaxation time. The information on distribution or local structure in the vicinity of paramagnetic centers might be obtained by taking MAS–NMR spectra at

shorter pulse delays. The NMR spectra of the powder of 5.8 wt% nitrogen content (T_1 = 19.3 s) were measured at PD = 400, 20, 5 seconds. These NMR spectra were exactly the same and no difference was observed. Further investigation is needed to get the information about the local structure in the vicinity of paramagnetics by NMR measurements at shorter pulse delays.

It was expected that a relationship between Ns and T_1 might be observed, because it was considered that spin–lattice relaxation would occur via paramagnetic centers. However, no distinct relationship between them was observed. The spin concentration of our laser synthesized powder was in the range from 8.9 x 10^{17} to 3.9 x 10^{19} spins/g. All the Ns of powders, even 8.9 x 10^{17} spins/g, might be too high to exhibit the different effects on T_1.

As illustrated in Fig. 4.1, the low magnetic field component was increased by introducing nitrogen. The mean crystalline sizes of SiC in these composite powders were in the range from 2.4 to 4.3 nm and they were almost the same size as that of ultrafine SiC powder. Therefore, the degree of broadening by small crystalline size was expected to be the same as that of SiC ultrafine powder. The low magnetic field component in NMR spectra suggested that there were Si atoms with structures different from those of SiC.

The chemical shift value of low magnetic field component was different from those of SiC, Si_3N_4, SiO_2 and Si. It was difficult to determine the structure around Si atoms, with a low magnetic field shift, by comparing the chemical shift with those of the standard inorganic materials. This is because there are few standard inorganic materials, that are composed of silicon, carbon and nitrogen atoms and have well defined structure.

In the field of organosilicon compound, many ^{29}Si NMR data is available. Thus, the chemical shift of SiC–Si_3N_4 powder was compared with those of organosilicon compounds to determine the local structure around Si atoms in the composite powders. In general, ^{29}Si chemical shift is affected by not only the nearest–neighbor

atoms but also the next–nearest–neighbor atoms. Therefore, it is necessary to take into account both the nearest– and the next–nearest–neighbor atoms for precise interpretation of the ^{29}Si chemical shift. However, since the nearest–neighbor atoms have greater effect on chemical shift than the next–nearest–neighbors, as the first approximation, only the nearest–neighbors were taken into consideration in this study. In β–SiC crystal, the Si atom is surrounded by four C atoms. Therefore, organosilicon compounds, which have a Si atom surrounded by four C atoms, such as $(CH_3)_4Si$ and its substituted compounds, could be used as reference materials. The chemical shift of $(CH_3)_4Si$ was zero, and the chemical shifts of its substituted compounds by the $-N(CH_3)_2$ group were in the range from 5.90 to 6.90 ppm for $(CH_3)_3SiN(CH_3)_2$, from −1.30 to −1.85 ppm for $(CH_3)_2Si(N(CH_3)_2)_2$, from −16.30 to −17.50 ppm for $CH_3Si(N(CH_3)_2)_3$ and from −28.10 to −28.60 for $Si(N(CH_3)_2)_4$ [19]. The chemical shift of ^{29}Si was toward a lower magnetic field, when one of the four carbon atoms around each silicon atom was substituted by a nitrogen atom. When two of the four carbon atoms were substituted by two nitrogen atoms, it shifted again toward a higher magnetic field. Then, it further shifted to higher field, as three and four carbon atoms were substituted by nitrogen. This behavior of the ^{29}Si chemical shift, which is observed in the case of stepwise substitution of SiR_4 type compound by another more electronegative group, is known as the "sagging behavior" [19]. In addition, this "sagging behavior" was predicted by semiempirical and empirical treatments considering the electronegativity of the substituent. Because nitrogen has higher electronegativity than carbon, if one of the four carbon atoms was substituted by nitrogen atom in β–SiC lattice, the ^{29}Si chemical shift was considered to move toward a magnetic field lower than that of a pure β–SiC. Therefore, the low magnetic field component in Fig. 4.1 was considered to come from the silicon atoms surrounded by three carbons and one nitrogen (SiC_3N).

It was known that Si–C(H) units showed the chemical shift in this low magnetic region [20]. It was possible that amorphous Si–C(H) species contributed the tail of

spectra in the low magnetic field. But this contribution of Si–C(H) species was probably small, because C–H and Si–H vibration could not be observed in the FT–PAS spectra of the powders, although direct chemical analysis of residual hydrogen was not carried out.

In order to see some compositional trend regarding the SiC_3N configuration, the integrated intensity was calculated. It was difficult to estimate precisely the degree of the broadening caused by poor crystallinity and the effect of the different next–nearest–neighbor atoms on NMR chemical shift. For instance, nitrogen atoms were considered to bond three or four silicon atoms, as discussed later. The coordination number of nitrogen could affect on ^{29}Si chemical shift, even though that effect was probably low compared to the effect of nearest–neighbor atoms. At the present stage, MAS–NMR cannot distinguish between $SiC_{3/4}N_{1/3}$ and $SiC_{3/4}N_{1/4}$. Babonneau et al [18] quantitatively analyzed the MAS–NMR data of $SiC_{(4-x)}O_x$ (x = 0 to 4) by peak deconvolution. In this study, peak deconvolution was not performed. It was simply assumed that the low magnetic component with the chemical shift from –5 to 30 ppm came from Si atoms with a SiC_3N configuration, and the integrated intensity of that range was measured. Peak deconvolution with some assumed different components may be suitable for discussions on subtle change of spectra, however the compositional trend of spectra would be seen by this simple calculation.

Figure 4.7 shows the change of the integrated intensity ratio of the low magnetic field component with the nitrogen content of the powders. The ratio of SiC_3N increased rapidly with the nitrogen content of the powder and became maximum at around 8 wt% nitrogen content. Then, it decreased with the nitrogen content. The dotted line shows the change of the atomic ratio of Si atom having SiC_3N configuration with nitrogen content, calculated by assuming that C atoms were randomly substituted by N atom in the β–SiC crystal and each N atom shared four Si atoms i.e. $SiC_{3/4}N_{1/4}$. If a N atom shared three Si atoms, i.e., $SiC_{3/4}N_{1/3}$, this dotted line shows the same tendency, but peak position shifts from 8.6 to 11.2 wt%. The

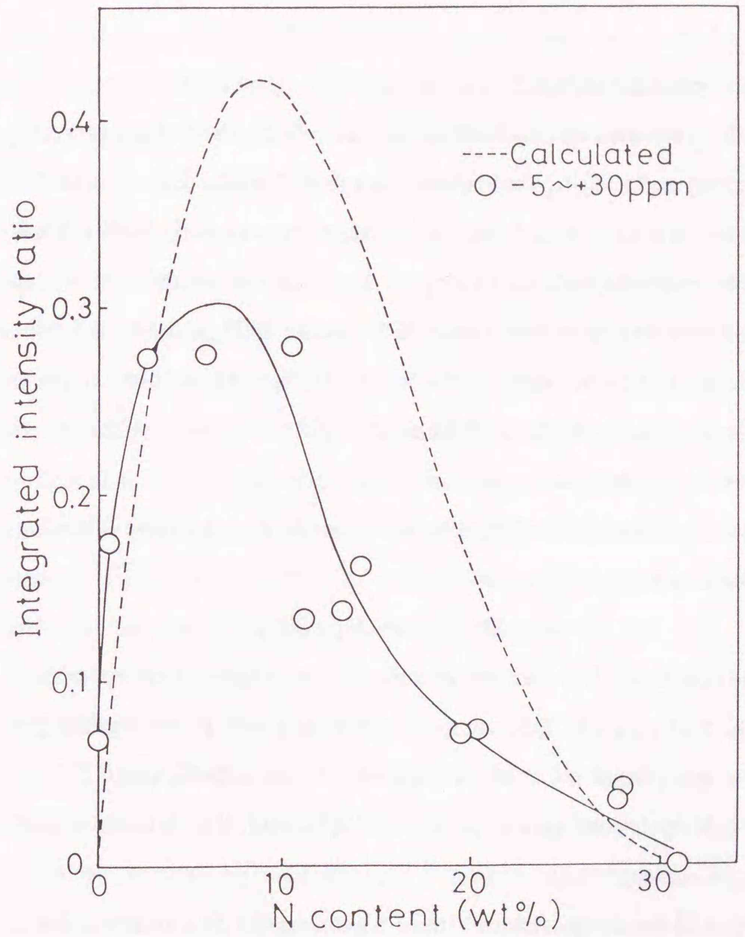

Fig. 4.7 Change of the integrated intensity ratio of the component between –5 and 30 ppm with nitrogen content of the powder. The dotted line shows the calculated atomic ratio of Si atoms with SiC_3N configuration.

integrated intensity ratio of the low magnetic field component showed a behavior similar to the calculated atomic ratio of Si with a SiC_3N configuration. This fact suggests that a SiC_4 unit was changed to $SiC_{3/4}N_{1/4}$ or $SiC_{3/4}N_{1/3}$ by random substitution of C atom for N atom.

4.4.1.2 Composite particles of high N content

Carduner et al. [6] reported that the NMR spectra of α–Si_3N_4 showed two peaks (–46.8 and –48.9 ppm) and β–Si_3N_4 showed one peak (–48.7 ppm). Even though the XRD pattern of the powder of Fig. 4.5(d) included both α– and β–Si_3N_4, the NMR spectrum exhibited only one peak at –48.3 ppm. The mean crystalline sizes of Fig. 4.5 (d) estimated by Scherrer's method were 35 nm for α–Si_3N_4 and 44 nm for β–Si_3N_4. In addition, the three peaks of α– and β–Si_3N_4 exist within 2.1 ppm. Therefore, in this experiment, the three NMR peaks could not be resolved because of the broadening caused by their poor crystallinity.

The chemical shifts of each Si configuration were considered to be in the following order, judging from the sagging behavior.

$$SiC_3N < SiC_4, SiC_2N_2 < SiCN_3 < SiN_4$$

In the case of the powders of high nitrogen content, the low magnetic field component decreased and the high magnetic field component increased with increasing nitrogen content. This suggests that a C–rich configuration such as SiC_3N and SiC_2N_2 decreased and a N–rich configuration such as $SiCN_3$ and SiN_4 increased with increasing nitrogen content.

In order to see some compositional trend regarding the Si configurations, integrated intensity was calculated as in the case of low N content particles. A calculation was carried out by simply assuming the chemical shift range for each silicon carbonitride unit as follows;

SiN_4 unit, –42.5 to –57.5 ppm

SiC_3N unit, –27.5 to –42.5 ppm

SiC_2N_2 unit, –5 to –27.5 ppm

SiC_4 unit, –5 to –27.5 ppm (overlapped with SiC_2N_2)

Figure 4.8 shows the integrated intensity ratio of these chemical shift ranges as a function of nitrogen content. Figure 4.9 shows the atomic ratio of Si atoms having various configurations as a function of nitrogen content, calculated by assuming that C atoms which tetrahedrally coordinated around Si atom, were randomly substituted by the introduced N atoms and each nitrogen shared four silicon atoms. If nitrogen atoms shared three silicon atoms, the calculated ratio of Si atoms would be different from that when nitrogen atoms shared four silicon atoms. For instance, the SiN_4 ratio became 1.0 at 33.3 wt% N content in the case of sharing four silicon, and at 39.9 wt% in the case of sharing three silicon. But the compositional trends were the same. The trends of each integrated intensity ratio in Fig. 4.8 were very similar to the corresponding curves in Fig. 4.9. These results suggested that the N–rich tetrahedral configuration of Si atoms increased in a stepwise manner as the nitrogen content of the powder increased. At the present stage, ^{29}Si MAS–NMR cannot distinguish between N atoms sharing three or four Si atoms. Further investigation should be carried out for more precise interpretation of NMR spectra.

4.4.2. ESR

The g value of ultrafine SiC was 2.0027 and is hardly affected by introducing nitrogen. The following were reported g values for several paramagnetic centers: g = 2.0055 for a Si dangling bond with only Si nearest–neighbors [21–23], g = 2.003 and ΔHpp = 14 G for a Si dangling bond with N nearest–neighbors [22–24], g = 2.0027 and ΔHpp = 6.1 G for C a dangling bond [25,26], g = 2.0024 for nitrogen in diamond [27], g = 2.004 $\pm$ 0.002 for nitrogen in 6H–SiC [28] were reported. These g values were very close to each other except g = 2.0055 for a Si dangling bond with only Si nearest–neighbors. Thus, it is difficult to identify the paramagnetic defect centers only by g values.

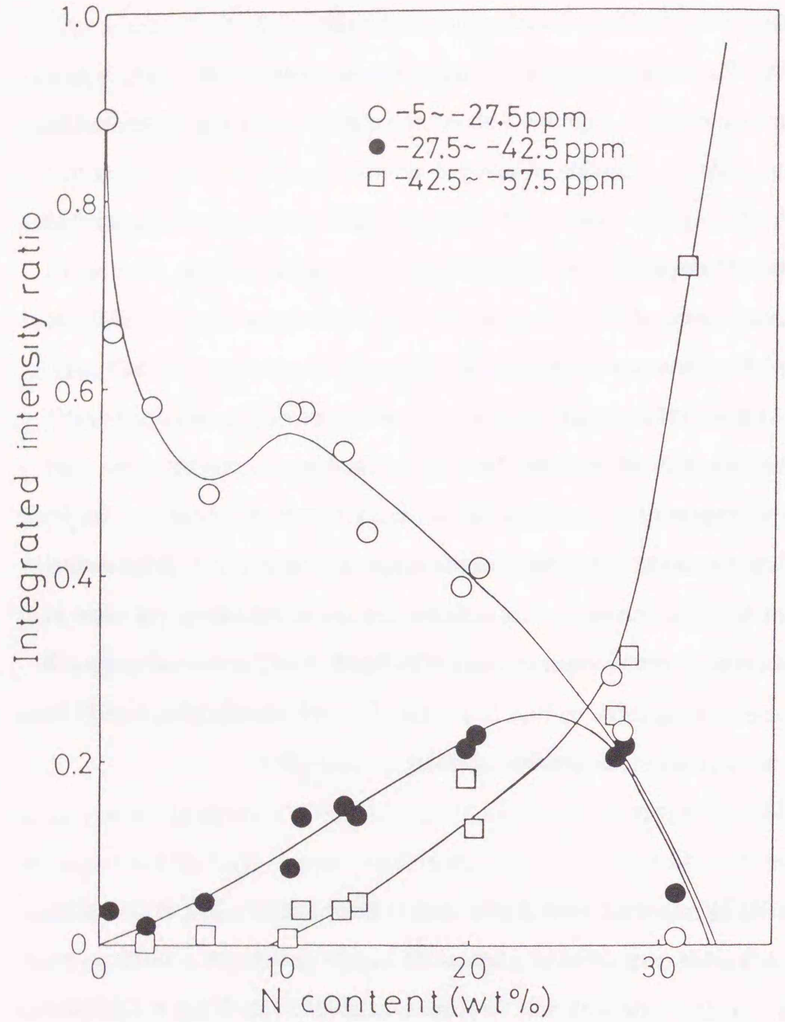

Fig. 4.8 Change of the integrated intensity ratio of various components with nitrogen content of the powder.

○ ; −5 to −27.5 ppm, $SiC_4 + SiC_2N_2$

● ; −27.5 to −42.5 ppm, $SiCN_3$

□ ; −42.5 to −57.5 ppm, SiN_4

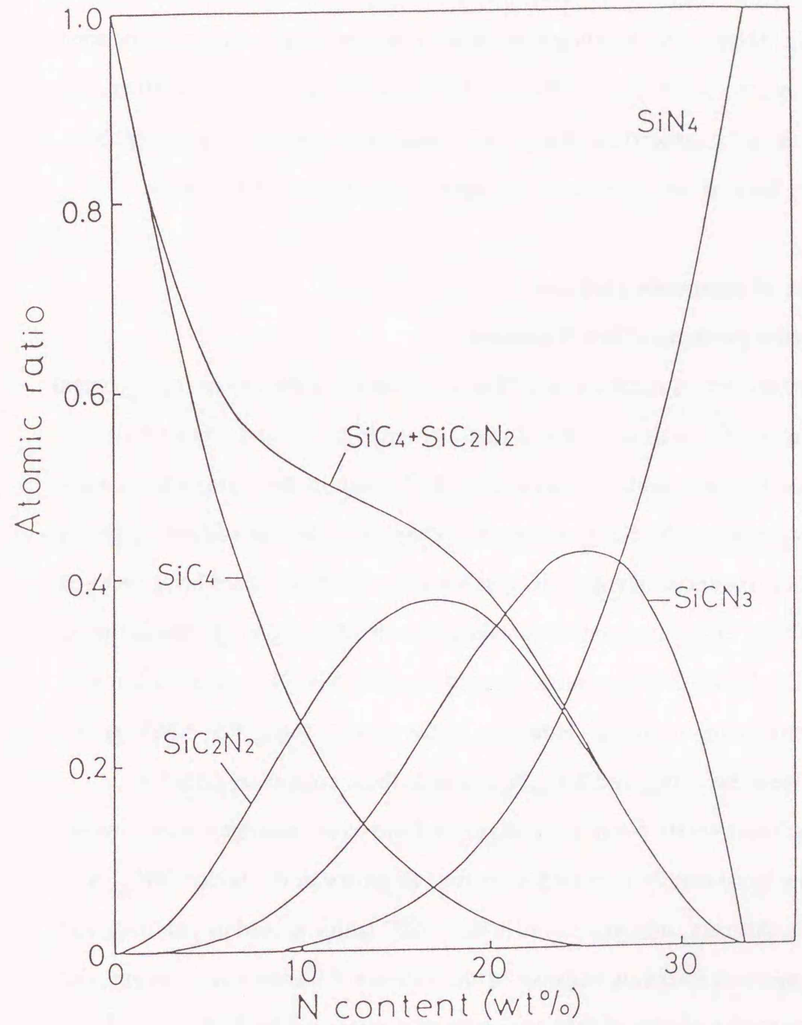

Fig. 4.9 Change of the calculated atomic ratio of Si atoms having various configurations with nitrogen content, assuming that C atoms, tetrahedrally coordinated around Si atom, were randomly substituted by N atoms.

When the nitrogen content exceeded 19.5 wt%, the ΔHpp of ESR spectra became larger and the Ns increased with increasing nitrogen content and Si_3N_4 phase. Those paramagnetic defects seemed to be characteristic of Si_3N_4 phase. Warren et al. [29] reported that the ΔHpp of Si dangling bond with N nearest neighbors was broadened by hyperfine interaction between ^{14}N and the Si dangling bond. Therefore, the increase of the ΔHpp suggested that the paramagnetic center with nitrogen neighbors, such as $\bullet Si(N)_3$, became dominant when nitrogen content exceeded 19.5 wt%.

4.4.3. Structure of composite particles

4.4.3.1 Composite particles of low N content

Transmission electron microscopic (TEM) observation of the low nitrogen content SiC–Si_3N_4 composite particles showed that a particle contained very small SiC crystals, and the lattice constant of crystalline SiC phase in the composite powder drastically decreased with nitrogen content. (chapter 3) It was suggested that a composite particle consisted of small SiC crystals and a grain boundary layer between the crystals and that SiC microcrystals contained dissolved nitrogen by substituting C atoms [14]. The MAS–NMR results showed that the SiC_3N configuration was produced by introducing nitrogen. However, at the present stage, ^{29}Si NMR cannot distinguish between $SiC_{3/4}N_{1/4}$ and $SiC_{3/4}N_{1/3}$ units in these composite particles.

In β–SiC microcrystals containing dissolved nitrogen, nitrogen atoms were considered to be tetrahedrally surrounded by four Si atoms in the lattice ($SiC_{3/4}N_{1/4}$, Fig. 4.10(a)). In this case, nitrogen atoms in the β–SiC lattice should be paramagnetic centers with unpaired electrons because of the valence difference of nitrogen and carbon. However, the results of spin concentration measured by ESR showed that most of the nitrogen atoms in the powder were present in a non–paramagnetic form.

There were two possible non paramagnetic nitrogen forms. One was a trivalent nitrogen bonded to three Si atoms ($SiC_{3/4}N_{1/3}$, Fig. 4.10(b)). The ultrafine SiC particles had many paramagnetic defects. Even though those defects had not been

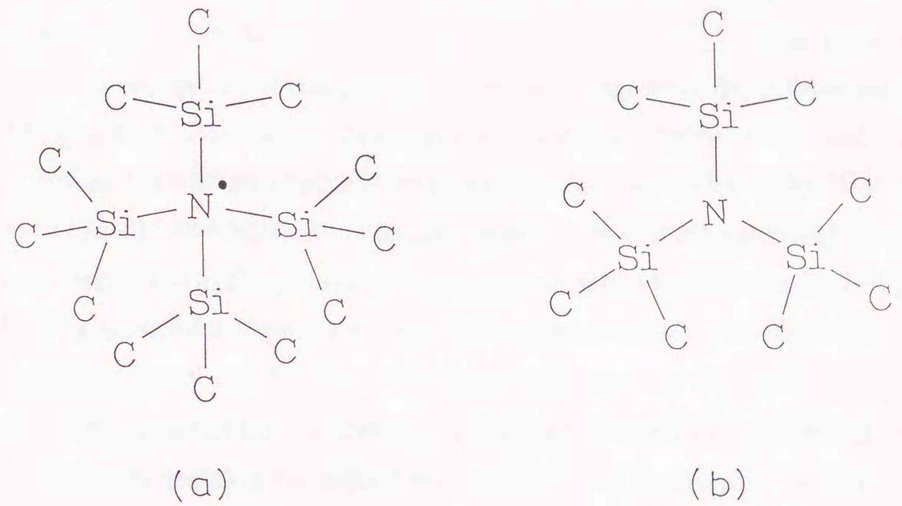

Fig. 4.10 Configuration of nitrogen atoms in the low nitrogen content SiC–Si_3N_4 composite particles.

identified, dangling bonds such as $\bullet C(Si)_3$ were considered to be present in ultrafine particles. If nitrogen atoms substituted the carbon atoms with a dangling bond, nitrogen could exist in a non–paramagnetic trivalent form ($N(Si)_3$). This might be the reason that spin density tended to decrease with increasing nitrogen content in the case of SiC–Si_3N_4 particles of low nitrogen content.

The composite particles showed only a broad SiC pattern, until nitrogen content increased to about 10 wt%. However, trivalent nitrogens were unlikely to be present in the β–SiC crystalline lattice at large amounts up to about 10 wt%, because they greatly distort the tetrahedral SiC lattice. Trivalent nitrogen atoms might exist in the grain boundary layer.

Another possible non paramagnetic form was positively charged nitrogen atom bonded to four Si atoms ($\oplus N(Si)_4$) making pairs of negatively charged defects such as $\ominus Si(C)_3$ or $\ominus C(Si)_3$. In this case, nitrogen atoms could exist in a β–SiC lattice, because nitrogens bonded to four silicons were expected to distort the β–SiC lattice less than trivalent nitrogens. Nitrogen might reduce the paramagnetic defect in the SiC phase, because Ns tended to decrease with increasing nitrogen content until nitrogen content reached to 19.5 wt%.

At the present stage, it seems most likely that nitrogen atoms in the powder partly dissolved into β–SiC crystal as the tetrahedral form bonded to four Si atoms, and were partly present in the grain boundary layer as trivalent forms bonded to three Si atoms.

4.4.3.2 Composite particles of high N content

In the case of SiC–Si_3N_4 composite particles of high N content, XRD results showed that SiC, Si_3N_4, Si and amorphous phases were present in the powder and their relative amount changed according to the nitrogen content of the powder. The previous study (chapter 3) showed that the lattice constants of Si_3N_4 phase in composite particles were different from those of pure Si_3N_4.

The NMR results showed that these particles consisted of SiC, Si_3N_4, and amorphous phases, and contained the configuration of $SiC_{(4-x)/4}N_{x/4}$ or $SiC_{(4-x)/4}N_{x/3}$ with x = 0 to 4. The proportion of N–rich Si configurations such as SiN_4 and $SiCN_3$ increased stepwise with increasing nitrogen content of the powder. As the N–rich configuration increased, the crystalline phase changed from SiC to Si_3N_4 or to an amorphous phase. Finally, the powder with nitrogen content of 30.9 wt% was composed of crystalline Si_3N_4 and Si. SiC phase was not completely pure, and contained nitrogen. Si_3N_4 phase exhibited a different lattice constant from that of pure Si_3N_4, but no direct evidence was found for the presence of C in crystalline Si_3N_4 phase by MAS–NMR.

4.5 Conclusion

The local structure of SiC–Si_3N_4 composite particles was studied by MAS–NMR and ESR. The low N content particles consisted of very small crystalline SiC containing nitrogen. The SiC_3N configuration was created by introducing nitrogen. It was suggested that nitrogen atoms in the low nitrogen content composite particles were partly present in β–SiC microcrystal tetrahedrally surrounded by four Si atoms and partly present in the grain boundary layer between SiC microcrystals in the particles in their trivalent state bonded to three Si atoms.

In the case of high nitrogen content powder, N–rich Si configurations increased with increasing nitrogen content of the powder, and the crystalline phase changed from SiC to Si_3N_4 or amorphous phases.

References

1. E. Oldfield and R. J. Kirkpatrick, "High–Resolution Nuclear Magnetic Resonance of Inorganic Solids.", Science, 227, 1537–44 (1985)
2. G. R. Hatfield and K. R. Carduner, "Review, Solid State NMR: Applications in High Performance Ceramics.", J. Mater. Sci., 24, 4209–19 (1989)
3. G. L. Turner, R. J. Kirkpatrick, S. H. Risbud and E. Oldfield, "Multinuclear Magic–Angle Sample–Spinning Nuclear Magnetic Resonance Spectroscopic Studies of Crystalline and Amorphous Ceramic Materials." Am. Ceram. Soc. Bull., 66(4), 656–63 (1987)
4. D. C. Apperley, R. K. Harris, G. L. Marshall and D. P. Thompson, "Nuclear Magnetic Resonance Studies of Silicon Carbide Polytypes." J. Am. Ceram. Soc., 74(4), 777–82 (1991)
5. K. R. Carduner, R. O. Carter III, M. E. Milberg and G. M. Crosbie, "Determination of Phase Composition of Silicon Nitride Powders by Silicon–29 Magic Angle Spinning Nuclear Magnetic Resonance Spectroscopy.", Anal. Chem. 59, 2794–97 (1987)
6. K. R. Carduner, C. S. Blackwell, W. B. Hammond, F. Reidinger and G. R. Hatfield, "^{29}Si NMR Characterization of α– and β–Silicon Nitride.", J. Am. Chem. Soc., 112, 4676–79 (1990)
7. N. R. Dando and M. A. Tadayyoni, "Characterization of Polyphasic Silicon Carbide Using Surface–Enhanced Raman and Nuclear Magnetic Resonance Spectroscopy.", J. Am. Ceram. Soc., 73(8), 2242–46 (1990)
8. G. R. Finlay, J. S. Hartman, M. F. Richardson and B. L. Williams, "^{29}Si and ^{13}C Magic Angle Spinning N.M.R. Spectra of Silicon Carbide Polymorphs.", J. Chem. Soc., Chem. Commun., 1985, 159–61 (1985)
9. J. R. Guth and W. T. Petuskey, "Silicon–29 Magic Angle Sample Spinning Nuclear Magnetic Resonance Characterization of SiC Polytypes.", J. Phys. Chem., 91, 5361–64 (1987)

10. J. S. Hartman, M. F. Richardson, B. L. Sherriff and B. G. Winsborrow, "Magic Angle Spinning NMR Studies of Silicon Carbide: Polytypes, Impurities, and Highly Inefficient Spin–Lattice Relaxation.", J. Am. Chem. Soc., 109, 6059–67 (1987)
11. K. R. Carduner, S. S. Shinozaki, M. J. Rokosz, C. R. Peters and T. J. Whalen, "Characterization of β–Silicon Carbide by Silicon–29 Solid–State NMR, Transmission Electron Microscopy, and Powder X–ray Diffraction." J. Am. Ceram. Soc., 73(8) 2281–86 (1990)
12. G. W. Wagner, B. K. Na and M. A. Vannice, "High–Resolution Solid–State NMR of ^{29}Si and ^{13}C in β–Silicon Carbides.", J. Phys. Chem., 93, 5061–64 (1989)
13. D. J. O'Donnell, T. T. P. Cheung, G. F. Schuette and M. Sardashti, "Solid–Sample ^{11}B Nuclear Magnetic Resonance and X–ray Photoelectron Spectroscopy Study of Boron–Doped β–Silicon Carbide.", J. Am. Ceram. Soc., 74(8), 2025–28 (1991)
14. M. Suzuki, Y. Maniette, Y. Nakata and T. Okutani, "Synthesis of Silicon Carbide–Silicon Nitride Composite Ultrafine Particles Using a CO_2 Laser", J. Am. Ceram. Soc., 76(5), 1195–200 (1993)
15. M. Suzuki, Y. Nakata, T. Okutani and A. Kato, "Preparation of SiC Ultrafine Particles by Using a CO_2 Laser", Seramikkusu Ronbun–shi, 97, 972–75 (1989)
16. G. C. Levy and I. R. Peat, "The Experimental Approach to Accurate Carbon–13 Spin–Lattice Relaxation Measurements", J. Magn. Resonance 18, 500–21 (1975)
17. K. E. Inkrott, S.M. Wharry and D. J. O'Donnell, "Silicon –29 Solids NMR–MAS Characterization of Non–Oxide powders and Fibers", Mater. Res. Soc. Symp. Proc., 73, 165–71 (1986)
18. F. Babonneau, G. D. Soraru and J. D. Mackenzie, "^{29}Si MAS–NMR Investigation of the Conversion Process of a Polytitanocarbosilane into SiC–TiC Ceramics", J. Mater. Sci., 25, 3664–70 (1990)

19. H. Marsmann, "^{29}Si-NMR Spectroscopic Results"; pp65-235 in NMR Basic Principles and Progress Vol.17, Oxygen-17 and Silicon-29, Edited by P. Diehl, E. Fluck and R. Kosfeld. Springer-Verlag, Berlin, 1981

20. G. D. Soraru, F. Babonneau and J. D. Mackenzie, "Structural Concepts on New Amorphous Covalent Solids" J. Non-Cryst. Solids, 106 256-61 (1988)

21. S. Hasegawa, N. Furuta, T. Takeshita, T. Inokuma and Y. Kurata, "Phosphorous and Nitrogen Doping into Polycrystalline SiC Films Prepared by Plasma-Enhanced Chemical Vapor Deposition at 700°C.", J. Appl. Phys. 72(4), 1374-77 (1992)

22. A. Morimoto, Y. Tsujimura, M. Kumeda and T. Shimizu, "Properties of Hydrogenated Amorphous Si-N Prepared by Various Methods.", Jpn. J. Appl. Phys, 24(11), 1394-98 (1985)

23. W. L. Warren, F. C. Rong, E. H. Poindexter, J. Kanicki and G. J. Gerardi, "Low-Temperature Electron Spin Resonance Investigation of Silicon Paramagnetic Defects in Silicon Nitride.", Appl. Phys. Lett., 58(21), 2417-19 (1991)

24. D. T. Krick, P. M. Lenahan and J. Kanicki, "Electrically Active Point Defects in Amorphous Silicon Nitride: An Illumination and Charge Injection Study.", J. Appl. Phys., 64(7), 3558-63 (1988)

25. A. Morimoto, T. Miura, M. Kumeda and T. Shimizu, "Glow Discharge a-$Si_{1-x}C_x$:H Films Studied by ESR and IR Measurements.", Jpn. J. Appl. Phys., 21(2), L119-L121 (1982)

26. I. Watanabe and K. Sugata, "ESR in Diamond Thin Films Synthesized by Microwave Plasma Chemical Vapor Deposition.", Jpn. J. Appl. Phys., 27(10), 1808-11 (1988)

27. W. V. Smith, P. P. Sorokin, I. L. Gelles and G. J. Lasher, "Electron-Spin Resonance of Nitrogen Donors in Diamond.", Phys. Rev., 115(6), 1546-52 (1959)

28. L. S. Dang, K. M. Lee, G. D. Watkins and W. J. Choyke, "Optical Detection of Magnetic Resonance for an Effective-Mass-like Acceptor in 6H-SiC.", Phys. Rev. Lett., 45(5), 390-94 (1980)

29. W. L. Warren, F. C. Rong, E. H. Poindexter, G. J. Gerardi and J. Kanicki, "Structural Identification of the Silicon and Nitrogen Dangling-Bond Centers in Amorphous Silicon Nitride.", J. Appl. Phys., 70(1), 346-54 (1991)

CHAPTER 5

SYNTHESES OF SILICON CARBIDE–SILICON NITRIDE COMPOSITE ULTRAFINE PARTICLES USING A RADIO-FREQUENCY PLASMA

CHAPTER 5

Synthesis of Silicon Carbide–Silicon Nitride Composite Ultrafine Particles Using a Radio–Frequency Plasma

5.1 INTRODUCTION

Nanometer–sized composite ceramics may have superior properties compared to monolithic ceramics. Silicon carbide–silicon nitride ($SiC–Si_3N_4$) composite powders were synthesized by various method such as furnace method [1], laser–induced gas–phase reaction method [2], d.c.plasma method [3] and hybrid plasma method [4]. For the nanometer–sized composite material processing, it is important and desirable to obtain the powders which have well controlled and uniform composition and structure.

In chapter 3 and chapter 4, the synthesis of $SiC–Si_3N_4$ composite ultrafine particles using a CO_2 laser was studied. The results of X–ray photoelectron spectroscopy (XPS), lattice constant measurement and electron energy loss spectroscopy (EELS) have indicated that Si, C, and N atoms were intimately mixed in the composite particles. Then, ^{29}Si magic angle spinning nuclear magnetic resonance (MAS–NMR) and electron spin resonance (ESR) spectroscopy were applied to clarify the local structure of the $SiC–Si_3N_4$ particles. The MAS–NMR results revealed that four C atoms around Si atom in β–SiC was substituted stepwise by N atom as the N content of the composite powder increased.

R. F. plasma method is also suitable for the production of non–oxide composite ultrafine particles, and it provides many interesting conditions such as ultrahigh temperature for reaction as discussed in chapter 1. In this chapter, the synthesis of $SiC–Si_3N_4$ composite ultrafine particles by R. F. plasma was studied.

Two plasma reactors and R. F. generators were used; one was made of quartz glass tube and had a relatively low out put power R. F. generator, the other was made of water–cooled quartz glass tube and had a high out put power R. F. generator. In the case of quartz glass reactor with a low power R. F. generator, $SiC–Si_3N_4$ ultrafine

particles were synthesized from chlorosilanes. In the case of water-cooled quartz glass tube reactor with a high power R. F. generator, they were synthesized from monosilane. The structure of SiC-Si_3N_4 particles was studied by X-ray diffraction (XRD), transmission electron microscope (TEM) and X-ray photoelectron spectroscopy (XPS). In addition, ^{29}Si MAS-NMR was applied to the SiC-Si_3N_4 particles synthesized using a high power R. F. generator to clarify their local structure.

5.2 Experimental Procedure

5.2.1 Synthesis of silicon carbide - silicon nitride composite particles using a low power R. F. generator

Figure 5.1 shows the schematic view of R. F. plasma torch with a low power R. F. generator. The torch was made of a quartz glass tube of 45 mm O.D. with triple walls. Ar gas was introduced to the tangential direction at both outer and inner tubes to stabilize the plasma. The flow rates of Ar gas were 8 l/min for the outer tube, 5 l/min for the inner tube, and 0.3 l/min for the center tube. Plasma was generated by applying R. F. voltage to the work coil. The output of the R. F. generator was 4 MHz, 1.9 kW.

SiC-Si_3N_4 composite fine powders were synthesized by injecting chlorosilanes ($SiCl_4$, $SiHCl_3$, SiH_2Cl_2), NH_3 and C_2H_4 into the tail flame of the plasma. Chlorosilanes and NH_3 react easily at room temperature to produce solid imide. Therefore, double walled nozzle was used to mix these reactant gases immediately before the plasma, preventing from the undesirable solid imide production. $SiCl_4$ and $SiHCl_3$ are liquid at room temperature and have high vapor pressure, so Ar gas was used as the carrier gas to the torch. The reactant gases were introduced to the plasma at the distance of L = 5 mm directly under the work coil. The temperature of the plasma was estimated to be in the range of 2100-2400 K at L = 5 mm, by inserting a high melting point metal wire inside the plasma. Considerable amount of generated

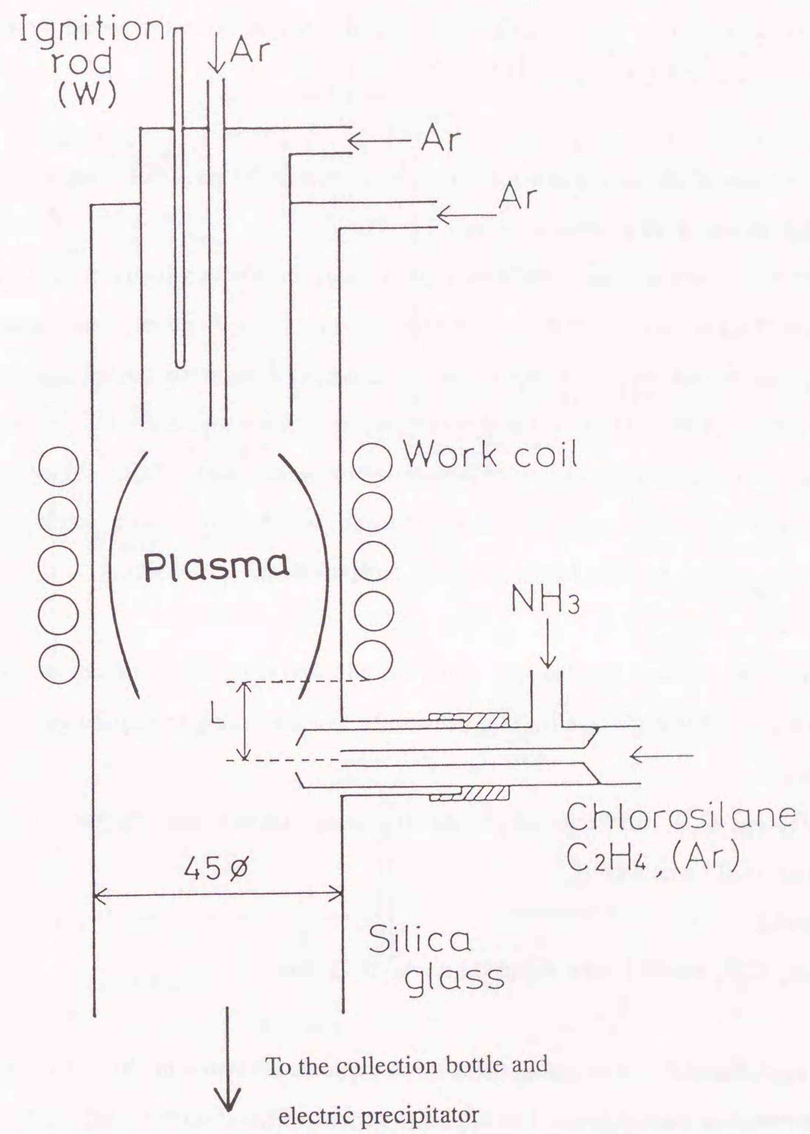

Fig. 5.1 Schematic view of R. F. plasma torch with a low power R. F. generator.

powders adhered to the wall of the quartz glass tube, and were collected as the samples. Powders were also collected from the collection bottle and electric precipitator, which were connected to the quartz glass tube. Powders contained NH_4Cl as by–products. Since NH_4Cl is sublimed at 610 K, it was removed by the heat treatment at 623 K for 1hr in Ar flow.

5.2.2 Synthesis of silicon carbide – silicon nitride composite particles using a high power R. F. generator

Figure 5.2 shows the schematic view of the plasma torch with a high power R. F. generator. This torch consisted of water cooled 42mm inner diameter–quartz glass tube, ring slit with 0.1mm slit width, water cooled copper plate, water cooled stainless steel chamber (500 x 500 x 500 mm) and torch head from which plasma gas was introduced. The maximum output of R.F. generator was 15 kW, 4 MHz. Since the properties of the powder might be influenced by the way how to inject reactant gas, the reactant gas was injected by the following three methods:

Method 1.

SiH_4 was injected into the Ar plasma, and NH_3 and C_2H_4 were injected to the plasma tail flame through the ring slit with H_2 as a quenching and carrier gas.

Method 2.

SiH_4 and C_2H_4 were injected into the Ar plasma, and NH_3 was injected to the plasma tail flame with H_2.

Method 3.

SiH_4, C_2H_4 and NH_3 were injected into $Ar–N_2$ plasma.

The experimental conditions of these three methods are listed in Table 5.1. The product powders were deposited on the inner surface of the stainless steel chamber and were collected as the samples.

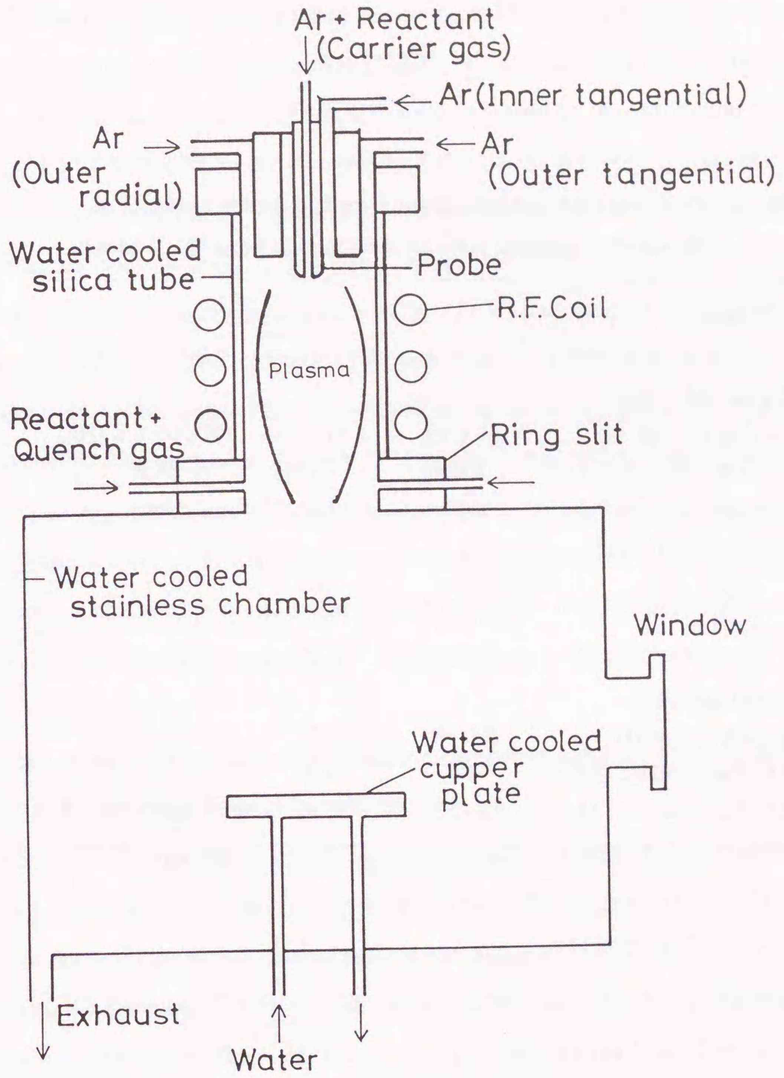

Fig. 5.2 Schematic view of R. F. plasma torch with a high power R. F. generator.

Table 5.1 Experimental Conditions of three method for the synthesis of $SiC-Si_3N_4$ ultrafine particles using a high power R. F. plasma

Method	1	2	3
Plasma gas (l/min)			
Outer radial gas	30 (Ar)	30 (Ar)	38 (Ar) + 3 (N_2)
Outer tangential gas	8 (Ar)	8 (Ar)	5 (Ar)
Inner tangential gas	2 (Ar)	2 (Ar)	2 (Ar)
Reactant gas (l/min)			
SiH_4	0.1	0.1	0.05
C_2H_4	0.76–1.2	0.1	0.03
NH_3	0.5–3.2	0.5–5.0	0.2
Carrier gas (Ar)	5	5	3
Quenching gas (H_2)	25, 40	40	---
R.F. Plate voltage (kV)	4.6	4.8	4.5
R.F. Plate current (A)	2.2–2.3	2.2	1.5

5.2.3 Characterization of the powder

The composition (C, N, O) of the powder was determined by C analyzer and N/O analyzer. The surface area was determined by one point BET method and crystalline phase was determined by X–ray diffraction (XRD). The lattice constants of β–SiC were measured from the β–SiC (311) line and were corrected by the diffraction line of highly pure Si (99.99%) powder that was mixed with the $SiC-Si_3N_4$ composite powder as an internal standard. The mean crystalline size of SiC was estimated by Scherrer's method from the β–SiC (111) line. The particle morphology and structure were observed by transmission electron microscope (TEM) and selected area electron diffraction (SAED). The chemical state of Si was studied by X–ray photoelectron spectroscopy (XPS). Solid–state ^{29}Si MAS–NMR spectra were acquired at 53.7 MHz using a JNM–GX270 spectrometer (JEOL). The samples were packed into 17 mm x 5 mm diameter zirconia rotars with polyimide endcaps. The spinning speed was between 5.7 and 6.2 kHz. The spectra were obtained following 90° pulse (4.5μs). All the chemical shifts were quoted relative to the signals for tetramethylsilane, although secondary external reference (poly–dimethylsilicone, –22 ppm) was used.

5.3 Synthesis of silicon carbide – silicon nitride composite particles using a low power R. F. generator from chlorosilanes

Table 5.2 lists the composition, surface area and crystalline phase of the powders synthesized from chlorosilanes using a low power R. F. generator. XRD measurement showed that an amorphous peak in the range of 20–25° (Cu, Kα) was observed in all the samples. Crystalline SiC, Si and Si_3N_4 phases besides amorphous phase were observed when the C_2H_4 flow rate was low. As the C_2H_4 flow rate increased, the crystalline phase became SiC only. The same tendency was observed in the cases of $SiCl_4$, $SiHCl_3$, and SiH_2Cl_2.

The composition of the particles depended on the reactant gas flow rate. The total C content of the powder increased as the C_2H_4 flow rate increased. These powders

Table 5.2 The composition, surface area and crystalline phase of the SiC–Si_3N_4 powders synthesized from chlorosilanes using a low power R. F. generator.

Sample No.	Reactant Chlorosilane	Gas C_2H_4 (SCCM)	Gas NH_3 (SCCM)	Composition C (wt%)	Composition O (wt%)	Composition N (wt%)	Surface Area (m^2/g)	Crystalline Phase
1	SiH_2Cl_2 10SCCM*	10	250	2.1	7.9	27.7	100.0	SiC, Si, Si_3N_4, Amo.
2	SiH_2Cl_2 10SCCM	20	250	4.0	6.8	29.9	76.3	SiC, Amo.**
3	SiH_2Cl_2 10SCCM	30	250	5.0	6.7	28.9	85.2	SiC, Amo.
4	$SiHCl_3$ 40mg/min	30	250	5.4	11.4	28.5	120.8	SiC, Amo.
5	$SiHCl_3$ 40mg/min	20	100	7.1	8.8	28.4	82.1	SiC, Amo.
6	$SiHCl_3$ 40mg/min	30	100	12.8	7.7	26.7	92.7	SiC, Amo.
7	$SiCl_4$ 40mg/min	8	100	3.7	14.4	25.3	61.8	SiC, Si, Si_3N_4, Amo.
8	$SiCl_4$ 40mg/min	20	100	14.1	9.1	23.2	95.0	SiC, Amo.
9	$SiCl_4$ 40mg/min	25	100	8.1	10.5	18.7	106.1	C, SiC, Amo.

*SiH_2Cl_2 = 10 SCCM = 10 standard cm^3/min = 45mg/min, **Amo.=Amorphous

also contained oxygen of 6–15 wt%, since the powders were handled in the air and the powder surface were oxidized. The tendency was found that oxygen content of the powder synthesized from SiH_2Cl_2 was smaller compared with those from $SiHCl_3$ and $SiCl_4$. This tendency was clearer in the case of Si_3N_4 production. Si_3N_4 powder synthesized from SiH_2Cl_2–NH_3 contained about 10 wt% oxygen, while those from $SiHCl_3$– or $SiCl_4$–NH_3 contained about 20 wt%. Si_3N_4 powders synthesized from $SiHCl_3$ and $SiCl_4$ oxidized more easily in the air, since their reactivity of these molecules are low and the reaction can not be completed up to inorganic Si_3N_4 leaving the bonds of N–H, Si–H, Si–Cl.

The powders synthesized from SiH_2Cl_2 contained less oxygen as impurity and were obtained with highest yield among all the chlorosilanes investigated in this study. Therefore, the SiH_2Cl_2–C_2H_4–NH_3 system was studied in detail. Table 5.3 lists the flow rate of reactant gases, and the composition, surface area, and crystalline phase of the powders. The crystalline phase showed the same tendency as in Table 5.2. Figure 5.3 shows the change of the total C and N content of the powder with C_2H_4 and NH_3 flow rate. Total C content increased as the C_2H_4 flow rate increased. When the NH_3 flow rate was 250 standard cm^3/min, the C content of the powder slightly increased, as the flow rate of C_2H_4 increased. When the C_2H_4 flow rate was 40 standard cm^3/min, the C content of the powder was 6.8 wt%. The C content of the powder was found to increase when NH_3 of 100 standard cm^3/min was diluted by injecting 150 standard cm^3/min of Ar. When NH_3 flow rate was small, total C content increased more rapidly as the C_2H_4 flow rate increased. On the other hand, total N content did not depend on the flow rate of C_2H_4, but solely on the flow rate of NH_3, and increased with increasing in the NH_3 flow rate. Figure 5.3 indicates that the composition of the powder can be controlled by changing the flow rate of reactant gas.

Figure 5.4 shows the TEM photographs of the fine particles synthesized with various flow rates of C_2H_4, NH_3 and with a constant flow rate of SiH_2Cl_2. These powders consisted of particles of 0.02–0.2 μm in size. In the case of low flow ratio of

Table 5.3 Reactant gas flow rate and composition, surface area, crystalline phase of the powder synthesized from SiH_2Cl_2.

Sample No.	Reactant Gas SiH_2Cl_2	C_2H_4	NH_3	Composition C	O	N	Surface area	Crystalline phase
	(standard cm^3/min)			(wt%)			(m^2/g)	
1	10	10	250	2.1	7.9	27.7	100.0	SiC, Si, Si_3N_4, Amo.
2	10	20	250	4.0	6.8	29.9	76.3	SiC, Amo.**
3	10	30	250	5.0	6.7	28.9	85.2	SiC, Amo.
10	10	40	250	6.8	8.6	29.5	84.8	SiC, C, Amo.
11	10	5	*100	6.0	20.8	10.3	46.6	Si, Si_3N_4, SiC, Amo.
12	10	10	*100	8.7	10.4	20.7	56.4	SiC, Si_3N_4, Si, Amo.
13	10	15	*100	13.5	12.4	17.0	69.5	SiC, Si, Amo.
14	10	20	*100	15.5	10.3	8.9	80.0	SiC, Amo.

* 150 standard cm^3/min Ar was added to 100 standard cm^3/min NH_3

** Amo. = amorphous

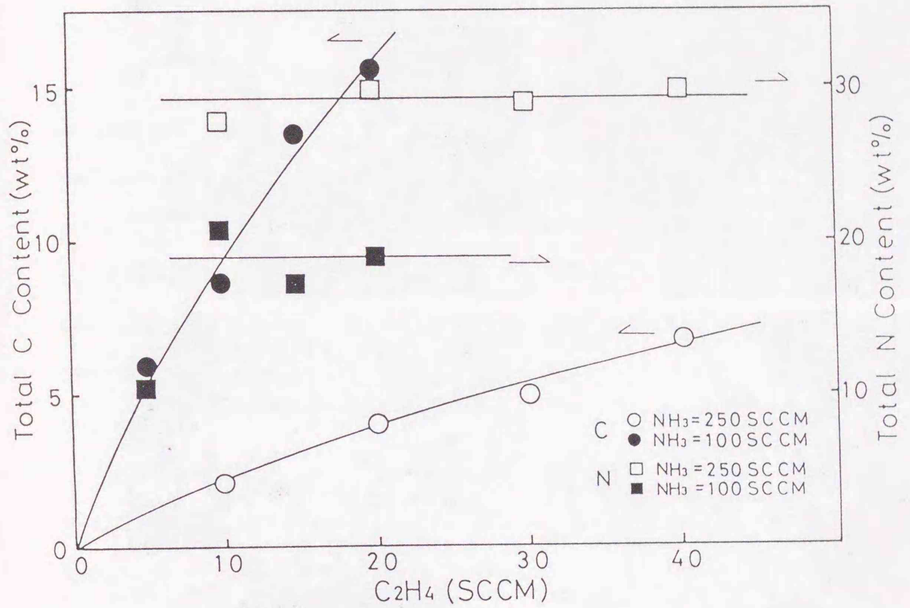

Fig. 5.3 The change of the total C and N content of the powder with C_2H_4 and NH_3 flow rate.

SCCM = standard cm^3/min

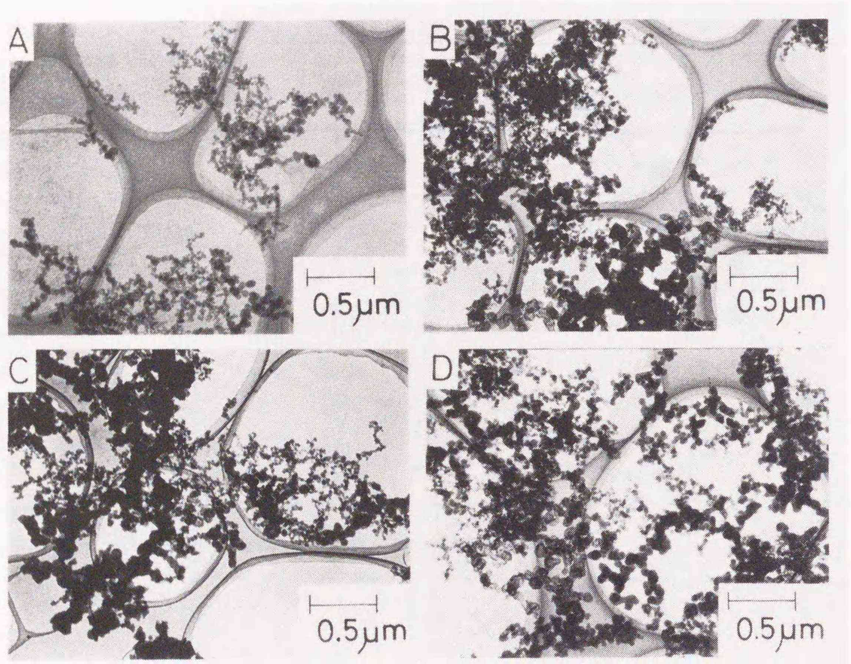

Fig. 5.4 TEM photographs of the fine particles synthesized with various flow rate of C_2H_4, NH_3 and with a constant flow rate of SiH_2Cl_2.

SiH_2Cl_2; 10 standard cm^3/min

(A) C_2H_4 = 10, NH_3 = 250 standard cm^3/min

(B) C_2H_4 = 40, NH_3 = 250 standard cm^3/min

(C) C_2H_4 = 10, NH_3 = 100 standard cm^3/min

(D) C_2H_4 = 15, NH_3 = 100 standard cm^3/min

C_2H_4 (A), the particles were smaller in size (0.02 – 0.1 μm) and spherical in shape, and many of them were uniform. As the C_2H_4 flow ratio increased, large particles (around 0.2 μm) with various kind of characteristic shape appeared. Typically four kind of characteristic shaped particles were observed by TEM; that is small (0.02 – 0.1 μm) and spherical particles, spherical particles (about 0.1 μm), angular particles (0.1 – 0.2 μm) and almost spherical but somewhere hexagonal particles as shown in Fig. 5.5 and 5.6. The selected area electron diffraction (SAED) observation was carried out to find out what these particles were.

Figure 5.5 and 5.6 show the TEM photographs and SAED patterns on some characteristic shaped particles. The SAED patterns showed that smaller and spherical particles (a) of about 0.02 μm were amorphous. Spherical particles (b) of about 0.1 μm were consisted of mainly Si, and a small quantity of cubic SiC. Angular particles (c) of 0.1–0.2 μm were β–SiC. Particles (d) of 0.1–0.05 μm which were almost spherical but somewhere hexagonal were carbon. The mixing of Si, C and N atoms in one particle could not be clearly found by the SAED observation, Although the composition of the amorphous particles were not clear,.

The XPS measurement on some samples was carried out to study the chemical state of elements in the powders. The XPS measurement can discriminate between the bond status of SiC, Si_3N_4, SiO_2 and others from their chemical shift. Figure 5.7 and 5.8 show the typical Si2p and C1s XPS spectra and the results of peak deconvolution. Si2p peak of XPS spectra was broad, and could be deconvoluted into three components of SiC, Si_3N_4 and SiO_2. The area intensity ratio of these components varied according to the composition of the powders. Cls peak of XPS spectra could be deconvoluted into SiC, graphite, and hydrocarbon, and the area intensity ratio of these components also varied according to the composition of the powders. N1s XPS spectra exhibited rather wide half width, but its peak position showed the existing of only Si_3N_4 and did not change with the composition of the powders. These results implied that the powders synthesized in this study were the mixtures of SiC, Si_3N_4, Si,

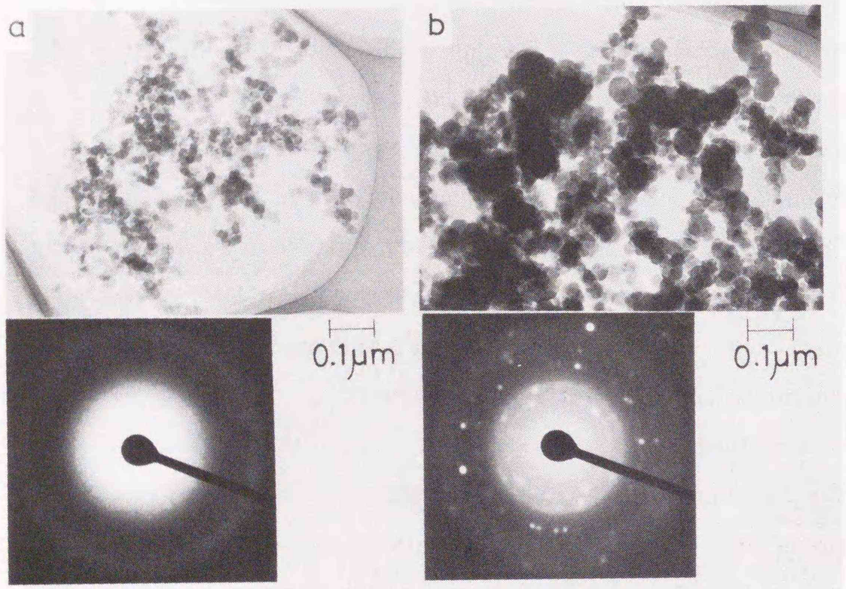

Fig. 5.5 TEM photographs and SAED patterns of various kind of the characteristic shaped particles observed in the composite powders.
(a) amorphous, (b) Si and small amount of SiC

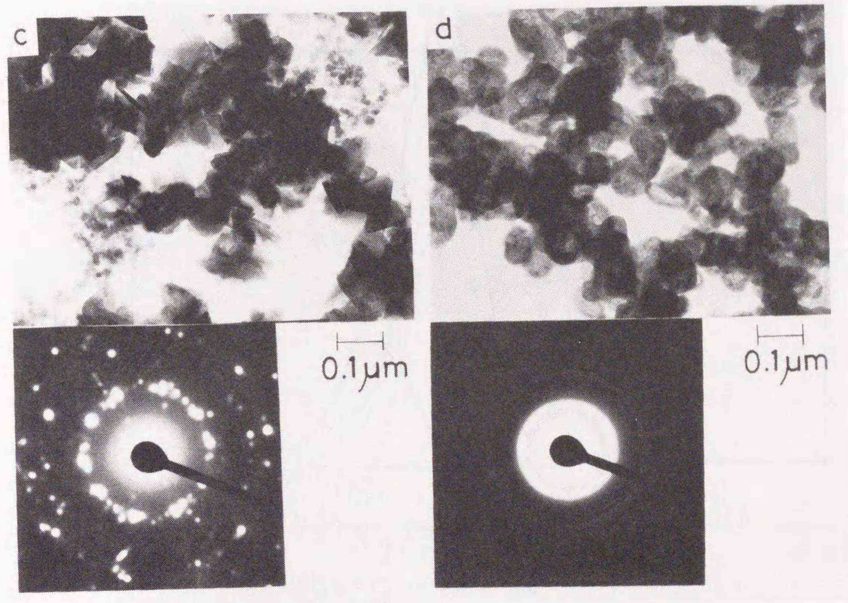

Fig. 5.6 TEM photographs and SAED patterns of various kind of the characteristic shaped particles observed in the composite powders.
(c) β–SiC, (d) C

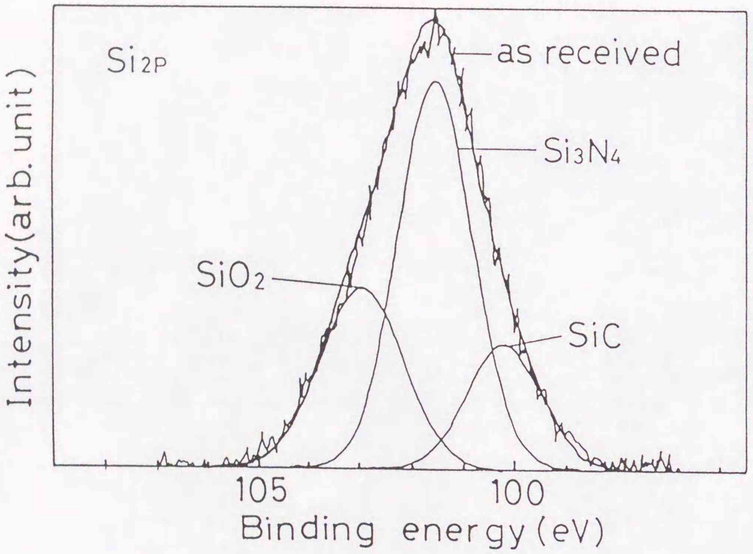

Fig. 5.7 Typical Si2p XPS spectrum of the SiC–Si_3N_4 composite particles (sample no. 3) and the result of peak deconvolution.

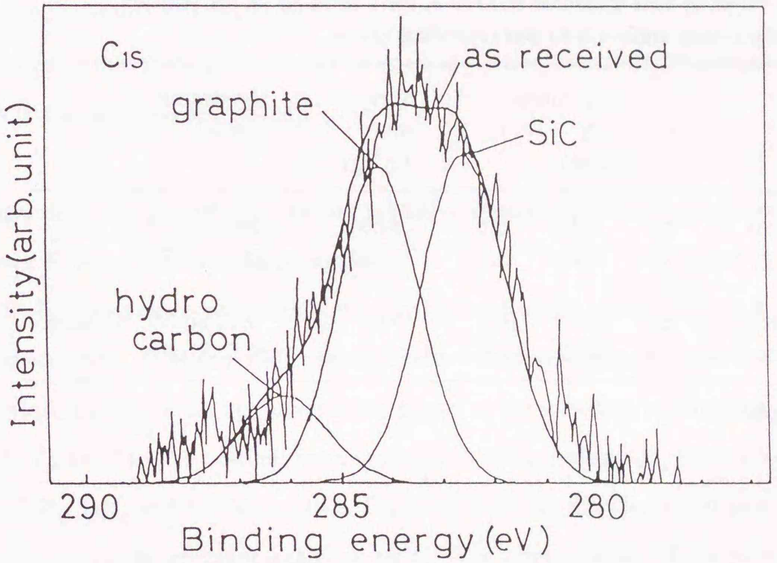

Fig. 5.8 Typical C1s XPS spectrum of the SiC–Si_3N_4 composite particles (sample no. 3) and the result of peak deconvolution.

Table 5.4. The effect of heat treatment at 1773 K for 1 hr in Ar on the powder composition, surface area and crystalline phase.

Sample No.	Composition (wt%) C	N	O	Surface area (m^2/g)	Crystalline phase
10 (as received)	6.8	29.5	8.6	84.8	SiC, C, Amo.*
(1773K, 1hr, Ar)	3.6	29.0	2.2	5.0	Si_3N_4, SiC
12 (as received)	8.7	20.7	10.4	56.4	SiC, Si_3N_4, Si, Amo.
(1773K, 1hr, Ar)	9.0	21.7	2.6	8.7	SiC, Si_3N_4

* Amo. = amorphous

C and amorphous particles. However, the composition and chemical state of the amorphous particles were not clear.

Some powders were heat-treated at 1773 K for 1 hr in Ar. Table 5.4 shows the effect of heat-treatment on the powders. Their surface area and the particle size were reduced by the treatment. The N content of the powder did not change by the heat treatment, but O content was reduced. Reduction in C content was observed in the samples, which showed isolated C in XRD, although no change in the C content was seen in other samples. The amorphous phase was disappeared by the heat treatment and became crystalline SiC and Si_3N_4.

It is expected that these powders can be used as starting materials for composite ceramics containing both SiC and Si_3N_4.

5.4 Synthesis of silicon carbide – silicon nitride composite particles using a high power R. F. generator from monosilane

SiC–Si_3N_4 composite particles were synthesized using a high power R. F. generator from SiH_4, C_2H_4 and NH_3. Table 5.5 lists the reactant gas flow rate and the composition, surface area, and crystalline phase of the powders synthesized by method 1 (Table 5.1). The powders were synthesized at a constant SiH_4 flow rate and various C_2H_4, NH_3 and H_2 flow rates. Figure 5.9 shows the change of powder composition with the reactant gas flow ratio. The composition of the powder depended on C_2H_4, NH_3 and H_2 flow rates. N content of the powders synthesized at H_2 = 40 l/min was higher than those at H_2 = 25 l/min. This result indicated that the increasing of quenching rate promoted nitridation reaction. Figure 5.10 shows the typical change of the X-ray diffraction (XRD) pattern with powder composition. When the C content of the powder was high, the XRD pattern was similar to that of β-SiC, but somewhat different, as diffraction lines of 34.0° and 38.4° are not observed in the case of β-SiC. This XRD pattern can be interpreted in two ways. One was the β-SiC contained small amount of α-SiC. The other was β-SiC phase with much

Table 5.5 Reactant gas flow rate and composition, surface area and crystalline phase of the SiC–Si_3N_4 composite ultrafine particles synthesized by method 1 using a high power R. F. generator.

Sample No.	Reactant gas				Composition			Surface area	Crystalline phase
	Probe	Ring slit			C	N	O		
	SiH_4 (l/min)	C_2H_4	NH_3 (l/min)	H_2	(wt%)			(m^2/g)	
1	0.1	0.76	0.5	25	26.9	7.7	1.7	65.5	SiC
2	0.1	0.76	1.0	25	21.6	11.8	1.5	56.7	SiC
3	0.1	0.76	1.5	25	14.8	18.0	2.2	52.7	SiC(w*), Amo.*
4	0.1	0.76	2.0	25	8.2	27.2	2.4	52.8	SiC(vw*), Amo.
5	0.1	0.76	2.5	25	2.9	34.2	1.9	58.3	SiC(vw), Amo.
6	0.1	0.76	3.0	25	2.3	36.2	1.9	59.1	SiC(vw), Amo.
7	0.1	0.76	0.5	40	19.7	13.5	2.0	71.9	SiC
8	0.1	0.76	1.0	40	14.0	19.7	2.0	60.6	SiC(w), Amo.
9	0.1	0.76	2.0	40	4.5	33.6	3.9	78.0	Amo.
10	0.1	0.76	3.0	40	1.4	36.4	2.2	91.1	SiC(vw), Amo.
11	0.1	1.2	0.5	40	24.0	10.7	1.8	84.6	SiC
12	0.1	1.2	0.8	40	18.8	16.4	2.2	72.2	SiC(w), Si(vw), Amo.
13	0.1	1.2	1.6	40	11.9	23.2	2.7	74.5	SiC(w), Amo.
14	0.1	1.2	3.2	40	5.3	33.3	3.5	87.8	Si(vw), Amo.

*w=weak, vw=very weak, Amo.=amorphous

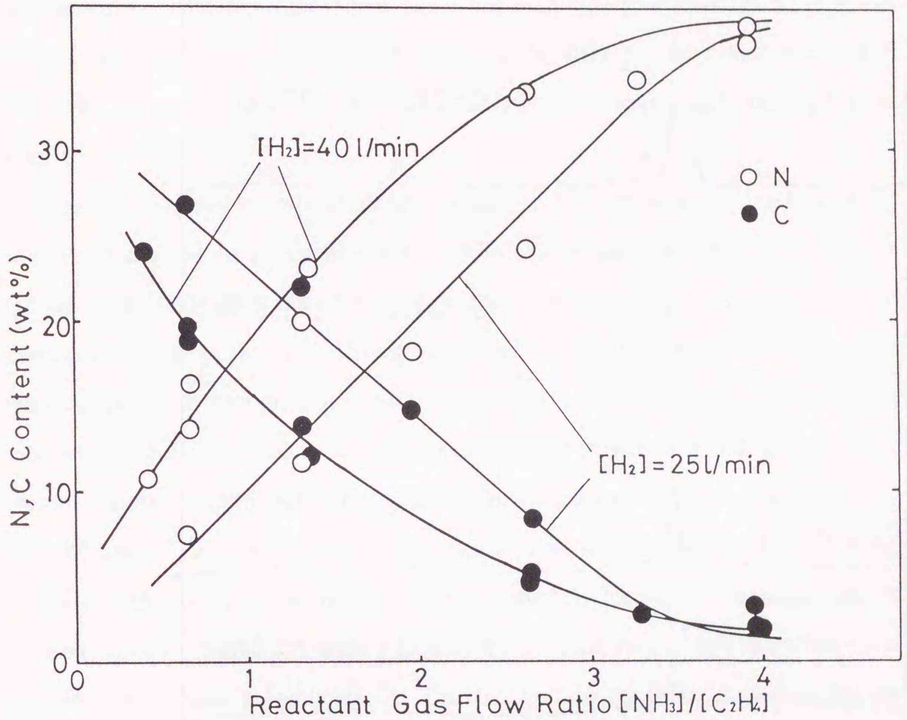

Fig. 5.9 The change of powder composition with the reactant gas flow ratio.

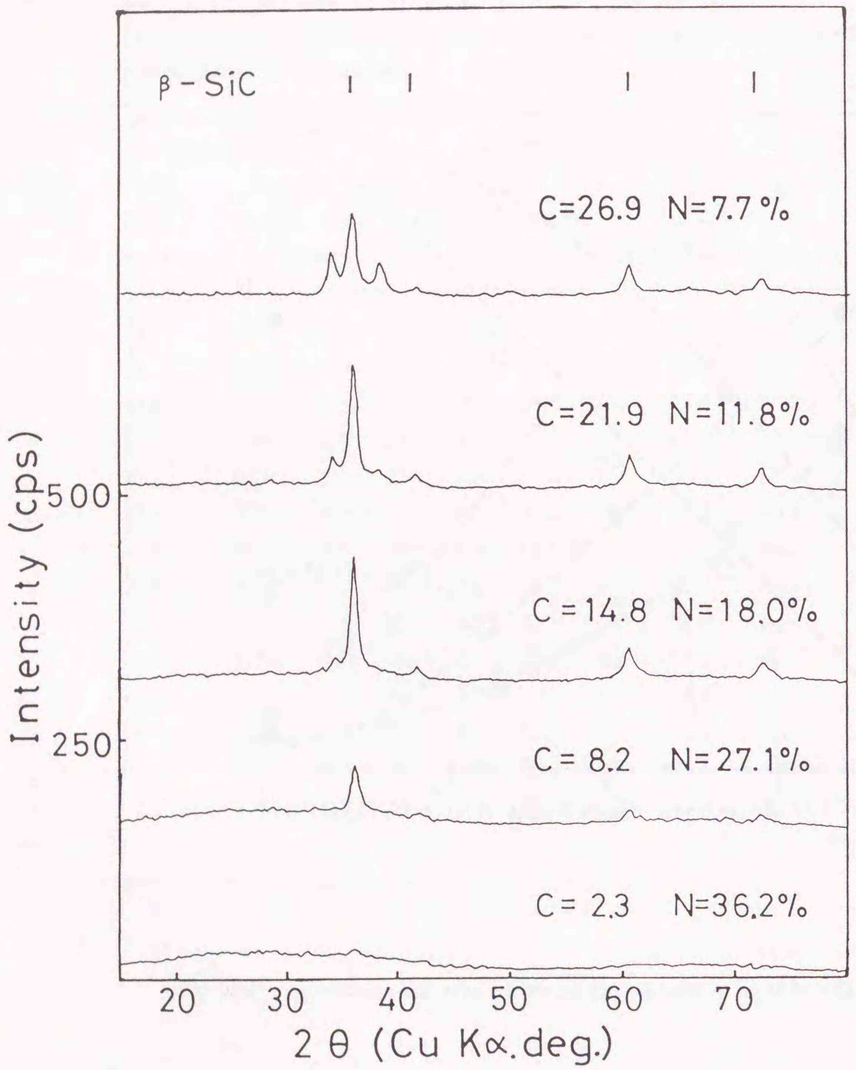

Fig. 5.10 The typical change of the XRD pattern with powder composition.

stacking faults, since Tateyama et al. [5] reported that SiC containing much stacking fault showed a similar XRD pattern to that of the mixture of β–SiC and small amount of α–SiC. The mean crystalline sizes of SiC determined by Scherrer's method were in the range from 11 to 17 nm. As the C content decreased and N content increased, the relative intensity of crystalline SiC decreased and amorphous phase appeared. When the composition of the powder was 2.3 wt% C and 36.2 wt% N, the powder was almost amorphous. Amorphous phase was more easily observed at H_2 flow rate of 40 l/min than at 25 l/min. Contents of C and N of the powders were changed in very wide range from few percent to about 30 wt% by changing NH_3 and C_2H_4 flow rate.

Figure 5.11 shows the typical TEM photographs of the powder. In the case of H_2 = 25 l/min, the powder consisted of the particles whose size was in the range of 0.01–0.4 μm. At low NH_3 flow rate (Fig. 5.11 (A)), the powder consisted of the angular and comparatively large particles (0.1–0.4 μm) and spherical particles. SAED pattern showed spots and ring pattern of SiC. At high NH_3 flow rate (Fig. 5.11 (B)), the number of angular particles decreased and most particles became spherical and SAED pattern became close to amorphous. The same tendency was observed in the case of H_2 = 40 l/min. The particle size was smaller at H_2 = 40 l/min than at H_2 = 25 l/min. It was considered that grain growth was suppressed by increasing quenching rate in the case of H_2 = 40 l/min. Figure 5.12 shows the typical bright–field and dark–field images of the powder (sample no. 1). The dark field image (SiC_{111}) showed that the small crystalline SiC were dispersed in the particles. The crystalline size was in the range from a few nm to 80 nm. The mean crystalline size might be almost the same size as that obtained by Scherrer's method (13 nm).

Figure 5.13 shows Si2p XPS spectra of the powders synthesized by method 1 and those of the mixtures of commercial SiC and Si_3N_4 powders. Si2p XPS spectra of the powder synthesized by method 1 showed almost single peak and the peak position agreed with that of Si_3N_4, regardless of their composition. For instance, the Si2p peak

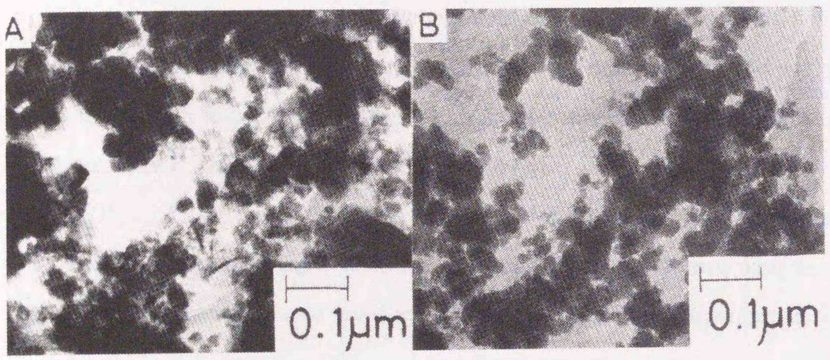

Fig. 5.11 The typical TEM photographs of the powder synthesized by method 1 using a high power R. F. generator.

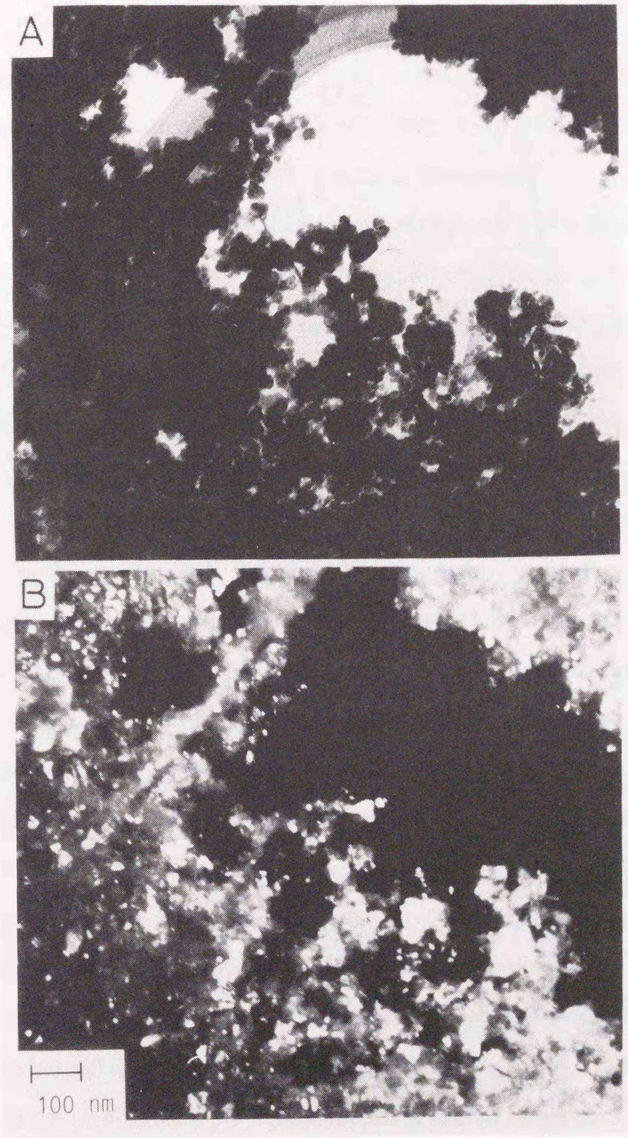

Fig. 5.12 Typical bright-field and dark-field images of the powder synthesized by method 1. (sample no. 1, C = 26.9 wt%, N = 7.7 wt%)

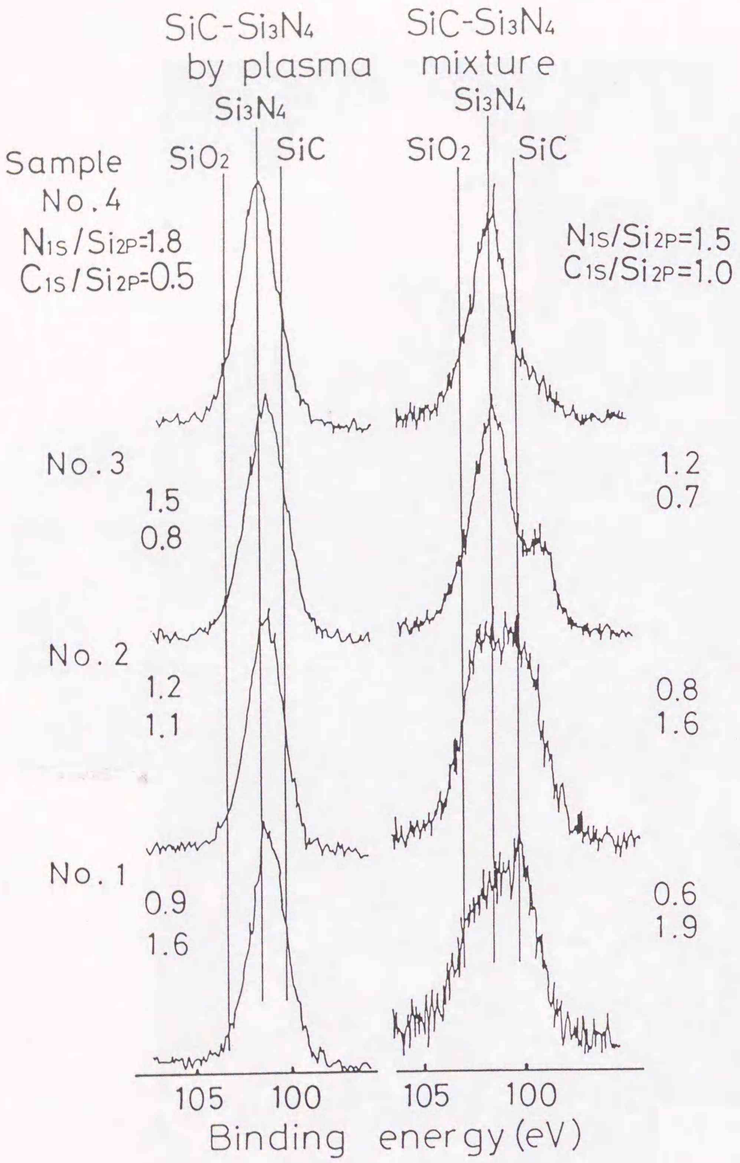

Fig. 5.13 Si2p XPS spectra of the SiC–Si_3N_4 composite powders synthesized by method 1 and of the mixtures of commercial SiC and Si_3N_4 powders.

position of sample no. 1 was very close to that of Si_3N_4, even though its composition was 7.7 wt% N and 26.9 wt% C. On the other hand Si2p XPS spectra of the mixture of SiC and Si_3N_4 showed two peaks corresponding to SiC and Si_3N_4. Thus, the chemical state of Si atoms in the powders synthesized by R.F. plasma were different from the simple mixture of SiC and Si_3N_4. These results were quite similar to the case of laser synthesized composite powders. (Chapter 3) In these powders, Si, N and C atoms were mixed each other and to form Si–C–N particles.

Figure 5.14 shows the change of the lattice constant of β–SiC phase with N content of the powder. The lattice constant decreased linearly with increasing N content of the powder. The same tendency was found in the case of laser synthesized SiC–Si_3N_4 ultrafine particles. In the case of plasma synthesized powder, the decreasing rate of lattice constant was considerably small compared to the case of laser synthesized powder. The decrease of lattice constant suggested that nitrogen dissolved into β–SiC lattice by substituting carbon.

Table 5.6 lists the reactant gas flow rate, and composition, surface area and crystalline phase of the powder synthesized by method 2. The powder was synthesized at a constant SiH_4, C_2H_4 flow rate and various NH_3 flow rates. The composition of the powder depended on the NH_3 flow ratio. Compared with powders produced by method 1, the powders produced by method 2 contained more nitrogen. The result of XRD showed these powders contained SiC, Si and amorphous phase. Figure 5.15 shows the example of TEM photograph of the powders synthesized by method 2. The particle size was in the range of 0.01–0.3 μm by TEM observation and the powder contained more spherical particles compared with those by method 1.

Figure 5.16 shows Si2p XPS spectra of the powders synthesized by method 2. These spectra exhibited the main peak with a binding energy of Si_3N_4. While Si2p XPS spectrum of the powder with 5.9 wt% carbon was almost single peak, Si2p XPS spectra of the powders with more than 8.6 wt% carbon had the shoulder peak at the position corresponding to SiC. This result indicated that some part of the powder or

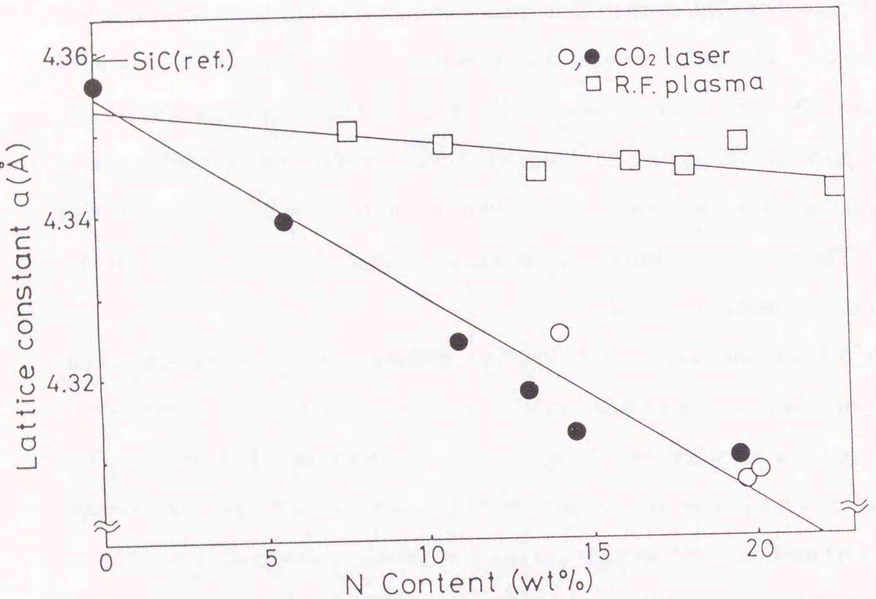

Fig. 5.14 The change of the lattice constant of β–SiC phase with N content of the powder.

Table 5.6 Reactant gas flow rate, composition, surface area and crystalline phase of the $SiC–Si_3N_4$ composite powders synthesized by method 2.

Sample No.	Reactant gas				Composition			Surface area	Crystalline phase
	Probe	Ring slit			C	N	O		
	SiH_4 (l/min)	C_2H_4 (l/min)	NH_3 (l/min)	H_2	(wt%)			(m^2/g)	
15	0.1	0.1	0.5	40	13.6	19.0	2.3	76.9	SiC(w*), Si(w), Amo*.
16	0.1	0.1	1.0	40	8.6	26.8	2.2	90.7	SiC(w), Si(w), Amo.
17	0.1	0.1	2.0	40	5.9	33.8	2.3	90.6	SiC(vw*), Si(vw), Amo.
18	0.1	0.1	5.0	40	5.7	36.1	3.3	108.8	SiC(vw), Si(vw), Amo.

*w = weak, vw = very weak, Amo. = amorphous

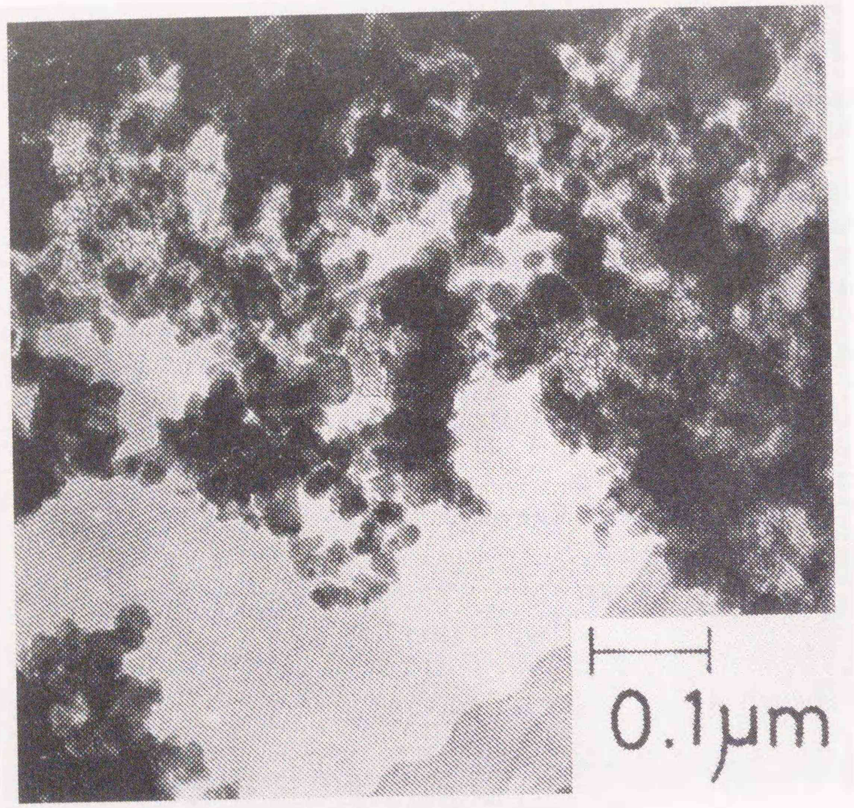

Fig. 5.15 The example of TEM photograph of the SiC–Si_3N_4 composite powders synthesized by method 2.

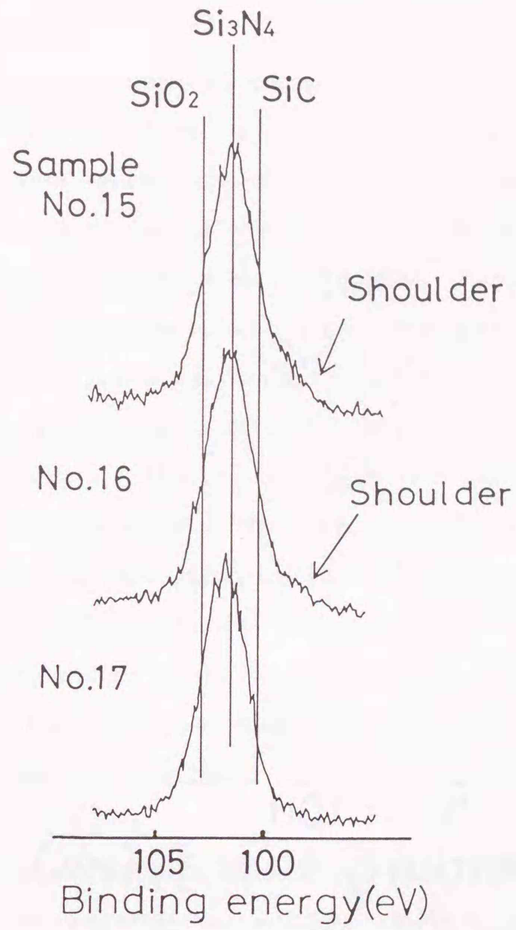

Fig. 5.16 Si2p XPS spectra of the SiC–Si_3N_4 composite powders synthesized by method 2.

sample no. 15; C = 13.6 wt%, N = 19.0 wt%

sample no. 16; C = 8.6 wt%, N = 26.8 wt%

sample no. 17; C = 5.9 wt%, N = 33.8 wt%

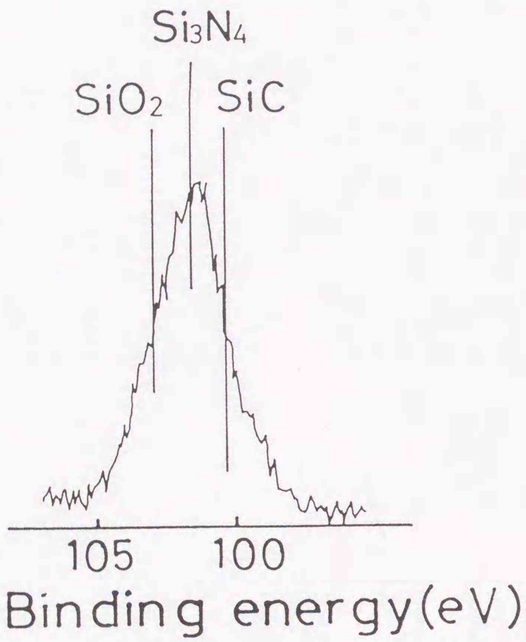

Fig. 5.17 Si2p XPS spectra of the SiC–Si_3N_4 composite powders synthesized by method 3.

particle was in the same chemical state as SiC, although XPS measurement can not distinguish a SiC sole particle from a SiC part of composite particles. But this results suggested that the powders synthesized by method 1 had different composite structure from those by method 2.

The powder was synthesized by injecting SiH_4, NH_3 and C_2H_4 into the Ar–N_2 plasma (method 3). The tail flame was not quenched by neither NH_3 nor H_2. In this method, plasma flame was rather unstable and much reactant could not be injected. Composite powder was synthesized by injecting the gas mixture of 0.05 l/min SiH_4, 0.03 l/min C_2H_4 and 0.2 l/min NH_3 to the Ar–N_2 plasma. Other conditions are listed in table 5.1. The powder, whose surface area was 42.9 m^2/g and composition of C = 14.6, N = 11.0, O = 3.6 wt% was obtained at the condition listed in Table 5.1. Crystalline phases were consisted of SiC and Si. The particle size was in the range of 0.02–0.5 μm according to TEM observation. Fig 5.17 shows the Si2p XPS spectra of the powder synthesized by method 3. The peak position of Si2p spectrum showed the binding energy of Si_3N_4. But this Si2p spectrum was somewhat broad and different from those of the powders obtained by method 1 and 2. The broadening of Si2p spectrum suggested that the powder had both SiC and Si_3N_4 components. These results suggested that the composite structure of the particles could depend on the way how the reactant gases were injected.

5.5 Characterization of SiC–Si_3N_4 composite powder by ^{29}Si MAS–NMR

^{29}Si MAS–NMR measurement was carried out to clarify the local structure of the typical composite particles synthesized using a high power R. F. generator by method 1. Table 5.7 lists the measured composite powders by ^{29}Si MAS–NMR.

Figure 5.18 shows the ^{29}Si NMR spectra of low N content powders. When N content of the powder was 7.7 wt% (Fig. 5.18(a)), the spectra was broad and situated between +30 to –50 ppm. The peak position was –19.1 ppm and differed from that of highly crystalline β–SiC (16 ppm). Carduner et al [6] reported that the fine β–SiC

Table 5.7 The list of composite powders measured by ^{29}Si–MAS–NMR.

Sample No	Reactant gas Probe SiH_4 (l/min)	Ring slit C_2H_4 (l/min)	NH_3	H_2	Composition C (wt%)	N	O	Crystalline phase	Mean crystalline size of SiC (nm)
1	0.1	0.76	0.5	25	26.9	7.7	1.7	SiC	13
2	0.1	0.76	1.0	25	21.9	11.8	1.5	SiC	--
3	0.1	0.76	1.5	25	14.8	18.0	2.2	SiC(w*), Amo.*	17
4	0.1	0.76	2.0	25	8.2	27.2	2.4	SiC(vw*), Amo.	15
5	0.1	0.76	2.5	25	2.9	34.2	1.9	SiC(vw), Amo.	--
6	0.1	0.76	3.0	25	2.3	36.2	1.9	SiC(vw), Amo.	--

*w = weak, vw = very weak, Amo. = amorphous

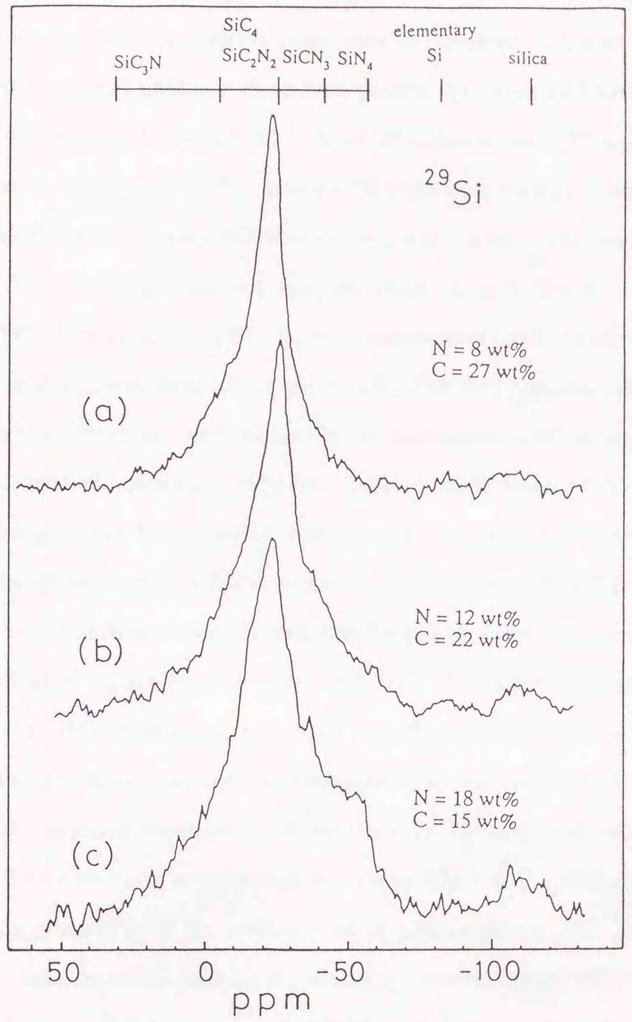

Fig. 5.18 ^{29}Si MAS–NMR spectra of low N content powders.

(a) C = 26.9, N = 7.7 wt% (sample no. 1), 176 scan, line broadening (LB) = 50 Hz, (b) C = 21.9 , N = 11.8 wt% (sample no.2), 192 scan, LB = 50 Hz, (c) C = 14.8, N = 18.0 wt% (sample no.3), 200 scan, LB = 50 Hz.

powder, having many stacking faults, exhibited broad spectra with a peak around −19 ppm. They also reported that the broadening of NMR spectra was caused by poor crystallinity. These powders consisted of very small crystals, therefore, these NMR spectra were broadened by poor crystallinity and many stacking faults. The spin lattice relaxation time, T_1 was estimated to be 20.4 sec for −19.1 ppm peak of Fig. 5.18 (a) by non linear inversion recovery (IR) method. This T_1 value was almost in the same range as those of the laser synthesized powder (chapter 4). When N content of the powder was 11.8 wt% (Fig. 5.18(b)), the peak position shifted to −23.6 ppm. In addition, high magnetic field component (around −40 ppm) increased. When N content of the powder reached 18.0 wt% (Fig. 5.18(c)), the peak position was −21.8 ppm and high magnetic field component increased further. As N content of the powder increased, surface oxide silica (around −105 ppm) increased. In chapter 4, it was assigned that the low magnetic field component between +30 and −5 ppm were from Si atoms with SiC_3N configuration. These NMR spectra contained low magnetic field component (+30 to −5 ppm) and their proportions were between 15 and 18 %. This results suggested that the composite particles have SiC_3N configuration. It was also assigned in chapter 4 that the component between −5 and −27.5 ppm were from SiC_4 and SiC_2N_2 configurations, that the component between −27.5 and −42.5 ppm was from $SiCN_3$, and that the component between −42.5 to −57.5 ppm was from SiN_4. The NMR spectra suggested that there existed SiC_3N, SiC_4, SiC_2N_2, $SiCN_3$, SiN_4 configurations in the powders and N−rich configurations such as $SiCN_3$ and SiN_4 increased with increasing N content of the powder. They also suggested that the powders were not the simple mixture of SiC and Si_3N_4 and that Si, C, N atoms were intimately mixed in the powders.

Figure 5.19 shows the ^{29}Si NMR spectra of high N content composite powder. The spectrum of the powder with N content of 27.1 wt% (Fig. 5.19(a)) was situated between +10 and −70 ppm. In addition, it contained the component around −80 ppm (elementary Si) and around −110 ppm (silica). The spectrum of the powder with 36.2

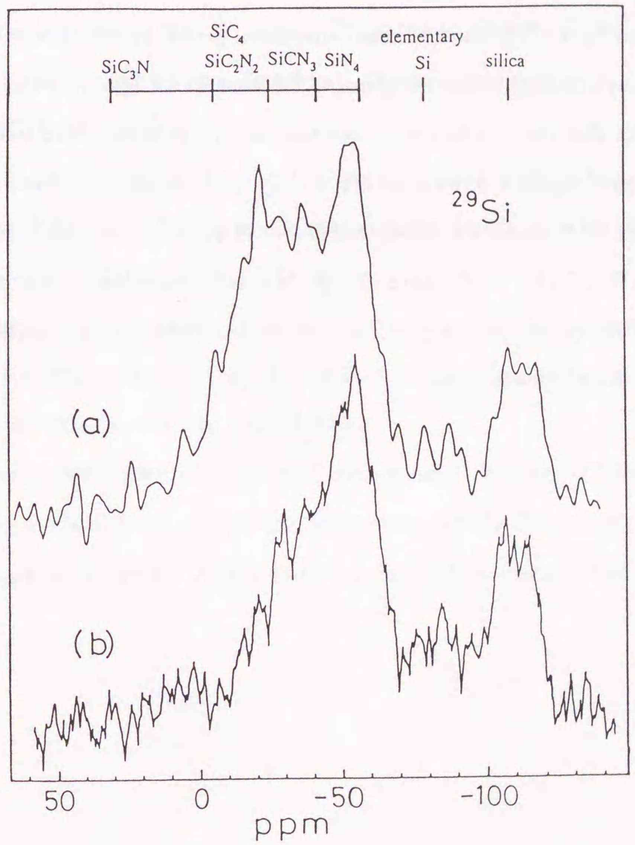

Fig. 5.19 ^{29}Si MAS−NMR spectra of high N content powders.
(a) C = 8.2, N = 27.2 wt% (sample no. 4), 200 scan, LB = 50 Hz,
(b) C = 2.3, N = 36.2 wt% (sample no. 6), 200 scan, LB = 50 Hz.

wt% N content was similar to Fig. 5.18 (a), but contained more component around −50 ppm. Because the component between −42.5 and −57.5 ppm was considered to indicate SiN_4 configuration, and the component between +5 and −42.5 ppm suggested that various kind of Si configuration (SiC_xN_{4-x}, x = 1 to 4) existed in the powders. Since XRD showed that these powder contained amorphous and small amount of β−SiC phase, these high N content powders are considered to consist of amorphous Si_3N_4 and amorphous Si−C−N phase and small amount of β−SiC phase. These NMR spectra exhibited much surface oxide component. Because NMR spectra were taken about two years after that the powders were synthesized, the powders were oxidized in the air. The high N content powders were mainly amorphous, therefore, these amorphous powders were easily oxidized, while low N content powders were not oxidized so much (Fig. 5.18). In the case of high N content powders, it was rather difficult to analyze the spectra precisely, because of the oxidation of the powder and the broadening due to amorphous phase.

Reference

1. J. Hojo, H. Maeda and A. Kato, "Preparation of Composite Particles of SiC − Si_3N_4 System by Vapor Reaction Method", Yogyo Kyokaishi, 95(1), 45−47 (1987)
2. G. W. Rice, "Laser Synthesis of Si/C/N Powders from 1,1,1,3,3,3−Hexamethyldisilazane", J. Am. Ceram. Soc., 69, C183−85 (1986)
3. J. Hojo, M. Nakamine and A. Kato, "Preparation of SiC−Si_3N_4 Composite Particles by Plasma Gas Phase Reaction.", Ceramic Transactions I, Am. Ceram. Soc. Inc., 277−84 (1988)
4. H. J. Lee, K. Eguchi and T. Yoshida, "Preparation of Ultrafine Silicon Nitride, and Silicon Nitride and Silicon Carbide Mixed Powders in a Hybrid Plasma.", J. Am. Ceram. Soc., 73(11), 3356−62 (1990)
5. H. Tateyama, N. Sutou and N. Murakawa, "Quantitative Analysis of Stacking faults in the structure of SiC by X−ray Powder Profile Refinement Method" Seramikkusu Ronbun−shi, 96, 1003 (1988)
6. K. Carduner, S. Shinozaki, M. Rokosz, C. Peters and T. Whalen, "Characterization of β−Silicon Carbide by Silicon−29 Solid−state NMR, Transmission Electron Microscopy, and Powder X−ray Diffraction" J. Am. Ceram. Soc., 73, 2281 (1990)

CHAPTER 6

SYNTHESES OF SILICA–ALUMINA ULTRAFINE PARTICLES USING A RADIO–FREQUENCY PLASMA AND ITS CATALYTIC CHARACTERISTICS

CHAPTER 6

Synthesis of Silica–Alumina Ultrafine Particles Using a Radio–Frequency Plasma and Its Catalytic Characteristics

6.1 Introduction

In the previous chapters, the synthesis and structure of SiC–Si_3N_4 composite particles were studied. The ceramics composite ultrafine powders are expected to use as excellent starting powders for the fabrication of ceramics composite. On the other hand, one of the most promising applications of ultrafine particles is for catalyst. In this chapter, the catalytic characteristics of ultrafine particles was studied.

For this purpose silica–alumina ($SiO_2 \cdot Al_2O_3$) was chosen as a model catalyst, since it is very popular and well known catalyst. The isomerization of 1–butene was employed as a model reaction. $SiO_2 \cdot Al_2O_3$ ultrafine particles were synthesized by argon – oxygen radio frequency plasma and the relationship between the synthesis conditions and catalytic activity and selectivity was studied as a fundamental study for the application of ultrafine particles as catalyst. Gani et al [1] have also synthesized $SiO_2 \cdot Al_2O_3$ particles by using radio frequency plasma torch and have investigated their phase transition and glass formation. But their catalytic action has not been investigated.

6.2 Experimental procedures

The schematic diagram of the single flow, vortex stabilized R. F. plasma torch is shown in Fig. 6.1. It consisted of a 24 mm outside diameter silica tube surrounded by a work coil supplied with a current at 4 MHz at powers up to 2.5 kW. Argon and oxygen mixed gas was introduced from the tangential gas inlet to produce a helical flow which stabilized plasma. The usual operating conditions were: 15 l/min Ar and 1 l/min O_2 plasma gas, at a power input of approximately 2 KW. $SiO_2 \cdot Al_2O_3$ particles were synthesized by injecting $SiCl_4$–$AlBr_3$ mixed gas into the tail flame of a argon–

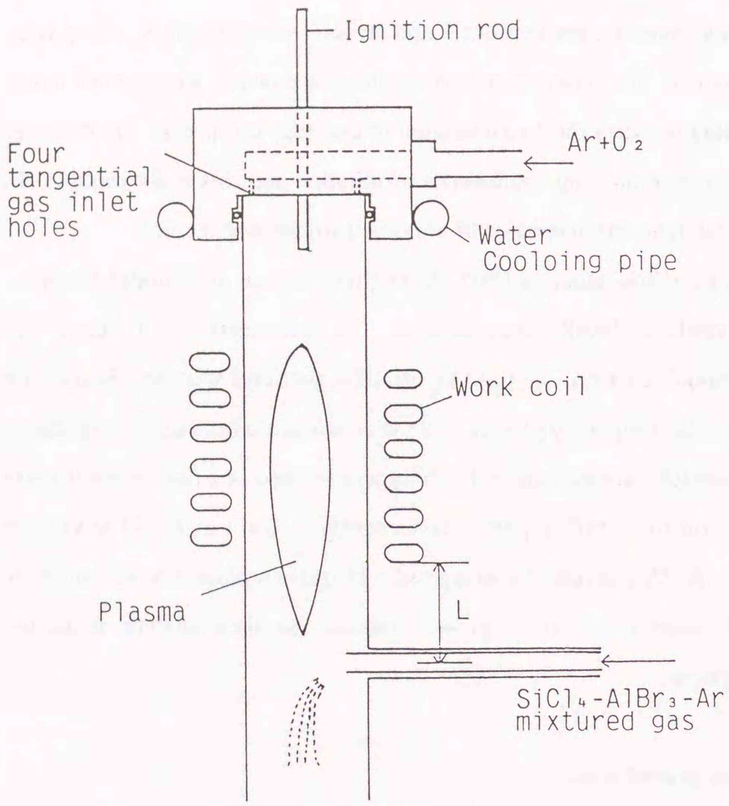

Fig. 6.1 Schematic diagram of R. F. plasma torch.

oxygen plasma torch. Two injecting points were chosen, and their respective distances (L) from the bottom of the work coil were 30 mm and 65 mm. The supplying rate of mixed halide gas was in the range of 200 to 500 mg/min with a 200 to 400 ml/min argon as a carrier gas. Si and Al molar ratio of the mixed halide gas was changed to obtain the $SiO_2 \cdot Al_2O_3$ powders with different composition. The product powders adhered to the inner wall of silica tube and were collected as a sample. A considerable amount of powder was exhausted outside with a carrier gas flow, since any other apparatus such as electric precipitator was not used.

$SiO_2 \cdot Al_2O_3$ powders were also synthesized by spraying isopropanol solution of methyltrimethoxysilane ($CH_3(CH_3O)_3Si$) and aluminum tri-sec-butoxide ($(C_4H_9O)_3Al$) into the tail flame of a argon-oxygen plasma torch using a nebulizer with 2 or 2.5 l/min argon gas flow. The solution was sprayed into the plasma at L = 30 mm.

The catalytic activity and selectivity were examined by the pulse method for the isomerization of 1-butene. The schematic diagram of the apparatus is shown in Fig. 6.2. The 0.1 ml of 1-butene was injected to the 5 to 20 mg catalyst which was previously activated at 673 K for 1 hr in He atmosphere. The product was once trapped by liquid nitrogen trap, until the conversion reaction completed. Then, the liquid nitrogen was removed and the product was heated and introduced to the gas chromatography. The conversion of 1-butene and the molar ratio of cis-2-butene to trans-2-butene of products were measured by gas chromatography. The amount of chemisorbed pyridine on the catalyst was measured by gas chromatography in the range from room temperature to 593 K. The surface area and pore volume of the powders were measured by BET method. The phases present in the powders were determined by X-ray diffraction (XRD). Al_2O_3 content was estimated by chemical analysis. The size and the shape of the particles were observed by transmission electron microscope (TEM, H-800NA, Hitachi). The samples for TEM were prepared using a dispersion method. A dilute dispersion of the powder in an alcohol

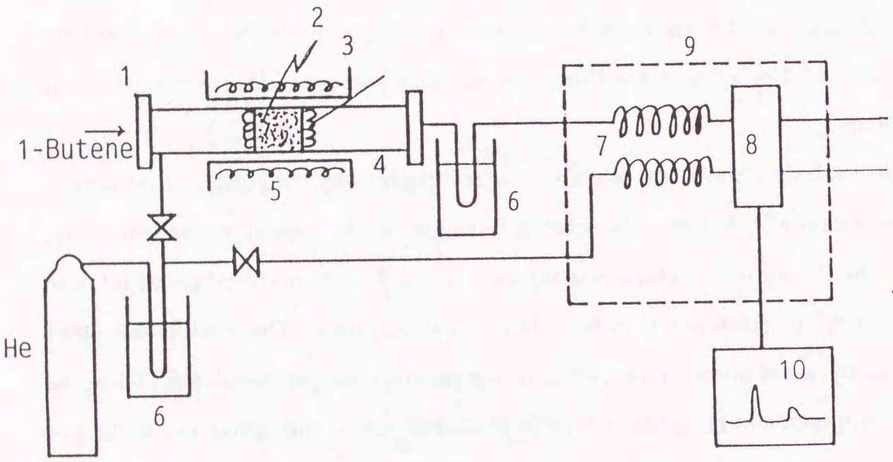

Fig. 6.2 Schematic diagram of the pulse reactor.

1: Injection port, 2: Sample, 3: Silica wool, 4: Pulse reactor, 5: Furnace, 6: Liquid N_2 trap, 7: Chromatographic column, 8: Detector (TCD), 9: Constant temperature bath, 10: Integrator & recorder.

1–butene pulse: 0.1 ml, Column: Porapak S (2 m) + Q (3 m), 3 mmϕ, Column temperature: 393 K, Detector temperature: 423 K, Carrier gas: He, 30 ml/min.

or an alcohol/water mixture was homogenized by an ultrasonic probe. Then, the drop of dispersion was placed on a carbon coated polyvinyl formal film supported on a copper grid. The mean particle size was determined by measuring the diameter of at least 400 particles in TEM photographs.

6.3 Results and Discussion

The composition, surface area and crystalline phase of the powders synthesized from mixed halide gas are summarized in Table 6.1 and 6.2. Those of the particles synthesized by spraying method are summarized in Table 6.3, and those of commercial catalysts used as a comparison are summarized in Table 6.4.

The X–ray diffraction pattern of the powders, whose composition was less than 35.8 wt% Al_2O_3, showed a broad amorphous peak between d = 0.37 to 0.42 nm. As Al_2O_3 content increased, small γ– or δ–Al_2O_3 peak appeared as well as an amorphous peak. Figure 6.3 shows the typical TEM photograph of SiO_2·Al_2O_3 ultrafine particles. TEM observation showed that the powders consisted of basically spherical particles. The particle sizes were in the range from 10 to 200 nm and larger particles were spherical and well dispersed, while the small particles whose size is in the range from 10 to 30 nm were not well dispersed, compared to the large particles. The particles synthesized at L = 30 mm showed a larger particle size and smaller surface area than those synthesized at L = 65 mm. For example, the mean particle size of UFP–10 synthesized at L = 30 mm was 34.8 nm and that of UFP–18 at L = 65 mm was 21.5 nm. The specific surface area calculated by its mean particle size was somewhat smaller than those measured. The difference is considered to be due to the presence of small pores.

Both temperatures of the center of plasma at L = 30 and 65 mm, which were roughly estimated by a melting point of a metal wire such as Pt and Mo inserted in the plasma, was in range from 2043 K to 2883 K, and could not be distinguished due to the roughly estimation. However, it was expected that the temperature at L = 65 mm

Table 6.1 Composition, surface area and crystalline phase of SiO_2•Al_2O_3 ultrafine particles synthesized at L = 30 mm

Sample	Content of Al_2O_3 (wt%)	Specific surface area (m^2/g)	Crystalline phase
UFP–1	0.4	123.8	Amorphous
UFP–2	0.6	77.3	Amorphous
UFP–3	2.2	108.6	Amorphous
UFP–4	4.9	149.7	Amorphous
UFP–5	6.3	64.5	Amorphous
UFP–6	9.5	71.0	Amorphous
UFP–7	12.5	55.1	Amorphous
UFP–8	15.2	118.6	Amorphous
UFP–9	17.2	96.0	Amorphous
UFP–10	29.3	57.8	Amorphous
UFP–11	35.8	62.1	Amorphous
UFP–12	60.2	37.2	Amorphous + γ or δ –Al_2O_3
UFP–13	61.4	55.1	Amorphous + γ or δ –Al_2O_3

Table 6.2 Composition, surface area and crystalline phase of SiO_2•Al_2O_3 ultrafine particles synthesized at L = 65 mm

Sample	Content of Al_2O_3 (wt%)	Specific surface area (m^2/g)	Crystalline phase
UFP–14	0.0	152.7	Amorphous
UFP–15	0.9	189.5	Amorphous
UFP–16	1.2	168.1	Amorphous
UFP–17	2.8	177.5	Amorphous
UFP–18	3.1	158.3	Amorphous
UFP–19	3.3	182.2	Amorphous
UFP–20	4.6	127.0	Amorphous
UFP–21	43.2	52.8	Amorphous + γ or δ –Al_2O_3

Table 6.3 Composition, surface area and crystalline phase of SiO_2•Al_2O_3 ultrafine paticles synthesized by spraying method at L = 65 mm.

Sample	Content of Al_2O_3 (wt%)	Specific surface area (m^2/g)	Crystalline phase
UFP–22	16.4	119.8	Amorphous
UFP–23	28.8	132.6	Amorphous

Table 6.4 Composition, surface area and crystalline phase of SiO_2•Al_2O_3 commercial catalysts

Sample	Content of Al_2O_3 (wt%)	Specific surface area (m^2/g)	Crystalline phase
Commercial–1	27.0	421.6	Amorphous
Commercial–2	9.9	505.6	Amorphous
Commercial–3	11.3	400.6	Amorphous
Commercial–4	24.1	288.3	Amorphous

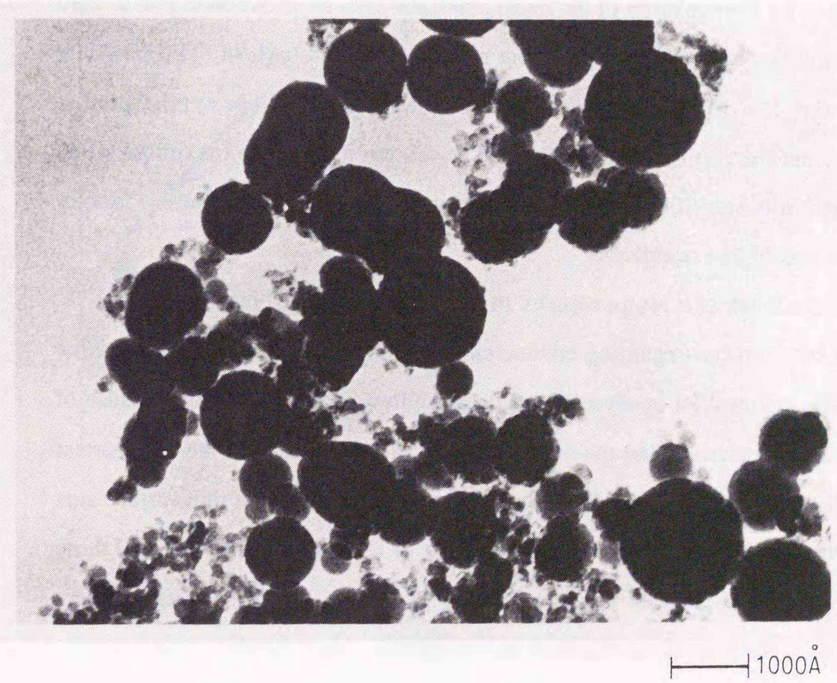

Fig. 6.3 Typical TEM photograph of SiO_2·Al_2O_3 ultrafine particles.
(UFP–7, synthesized at L = 30 mm, Al_2O_3 content 12.5 wt%)

was lower than that at 30 mm. It was considered that the particles synthesized at L = 65 mm stayed in the high temperature region for very short time compared to L = 30, so much so that the particle growth did not occur markedly and their size was small.

Figure 6.4 shows the relationship between Al_2O_3 content and the selectivity C/T of the catalyst. The cis–trans ratios of the produced 2–butene were measured at various conversion by changing the reaction temperature. The selectivity (C/T) of the catalyst was estimated by extrapolation of the linear cis–trans ratio vs. conversion plot to zero conversion. The C/T values were in the range from 1.18 to 1.94. The powders synthesized at L = 30 mm showed superior selectivity than those synthesized at L = 60 mm and the commercial catalysts. The selectivity became maximum when Al_2O_3 content was near 30 wt%. The powders synthesized by spraying at L = 30 mm showed the next higher selectivity.

Table 6.5 shows the temperatures in which 10 mg catalyst showed 50 % conversion of 1–butene regarding commercial catalysts and representative ultrafine particles. The commercial catalysts showed the highest catalytic activity, because of its enormous surface area, and the activity decreased in the order of the commercial catalysts, L = 65, L = 30 (spray), L = 30 mm. But the conversion per unit surface area of the commercial catalysts were the same as those of UFP–18 and UFP–23 and those of UFP–7 and UFP–10 were somewhat lower. The SiO_2 ultrafine particles were inactive even at the reaction temperature of 463 K.

Figure 6.5 shows the amount of chemisorbed pyridine per unit surface area of the catalyst (Np). At room temperature, commercial–4 and UFP–18 showed the same Np and commercial–2 and UFP–7 showed the same Np. Np decreased as the temperature increased in all the case, but UFP–18, which was synthesized at L = 65 mm, adsorbed more pyridine than others in the high temperature region above 373 K, and showed slight decrease as the temperature increased. This result suggested that UFP–18 had many strong acid sites. It is remarkable that UFP–18 had many strong

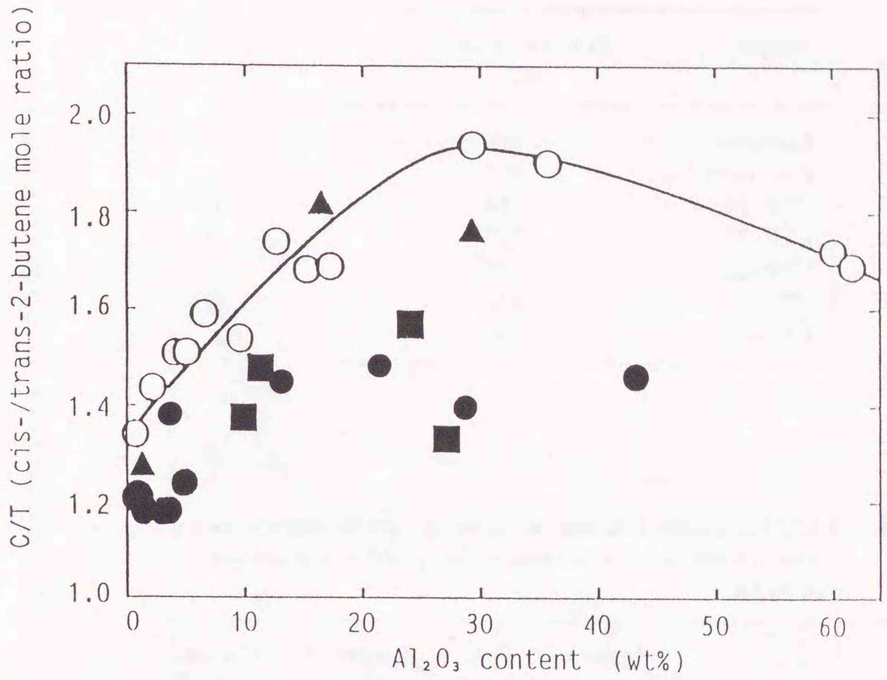

Fig. 6.4 Relationship between Al_2O_3 content and the selectivity (cis–/trans–2–butene molar ratio) of the catalysts.

○ : SiO_2·Al_2O_3 ultrafine particles synthesized at L = 30 mm

● : SiO_2·Al_2O_3 ultrafine particles synthesized at L = 65 mm

▲ : SiO_2·Al_2O_3 ultrafine particles synthesized by spraying

■ : SiO_2·Al_2O_3 commercial catalysts

Table 6.5 Reaction temperature at 50 wt% conversion on use of 10 mg of various catalysts

Sample	Reaction temperature (K)
Commercial–2	308
Commercial–4	315
UFP–18	319
UFP–23	322
UFP–22	336
UFP–7	346
UFP–10	359

Table 6.6 C/T (cis–/trans–2–butene molar ratio), specific surface area, pore volume, amount of chemisorbed pyridine and content of Al_2O_3

Sample	C/T	Specific surface area (m^2/g)	Pore volume (cm^3/g)	Amount of chemisored pyridinc ($mmol/m^2$)	Content of Al_2O_3 (wt%)
UFP–7	1.74	37.2	0.0399	0.00221	12.5
UFP–10	1.94	57.8	0.0466	0.00139	29.3
UFP–18	1.18	158.3	0.0827	0.00270	3.1
Commercial–2	1.38	505.6	0.615	0.00205	9.9
Commercial–4	1.57	288.3	0.388	0.00275	24.1

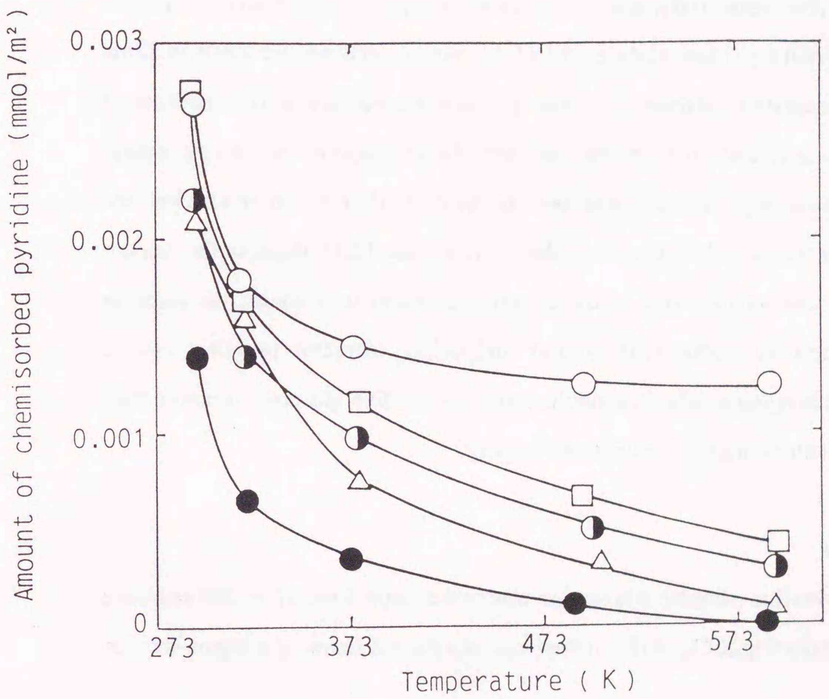

Fig. 6.5 Amount of chemisorbed pyridine vs. temperature.

○ : UFP–18, ◑ : UFP–7, ● : UFP–10,

□ : Commercial–4, △ : Commercial–2

acid sites, even though its Al_2O_3 content was very low (3.1 wt%). Such catalysts may be effective for the reactions which need strong acid sites at high temperature. On the other hand, Np of UFP–7 was almost the same as those of commercial catalysts and Np of UFP–10 was the lowest. It was considered that the particles synthesized at L = 65 mm had many frozen defects because they stayed in the high temperature region for very short time, then were subjected to rapid cooling.

The composition, selectivity, specific surface area, pore volume and amount of chemisorbed pyridine per unit surface area of the typical catalysts are listed in Table 6.6 for the representative catalysts. Ultrafine particles showed low activity because of its small surface area and pore volume, but they showed superior selectivity, except for UFP–18 whose Al_2O_3 content was low. In the case of platinum and nickel, the catalytic activity was found to depend on the particles size. [2,3] Because the amount of acid site per unit surface area of the ultrafine particles was almost the same as those of commercial products, if smaller $SiO_2 \cdot Al_2O_3$ ultrafine powders can be synthesized by changing synthesis conditions such as reactive gas concentration, they are expected to exhibit high selectivity and activity.

6.4 Conclusions

1) $SiO_2 \cdot Al_2O_3$ ultrafine particles whose size was in the range from 10 to 200 nm were synthesized by injecting $SiCl_4$–$AlBr_3$ mixed gas into the tail flame of a argon–oxygen R. F. plasma.

2) The characteristics of particles were different according to the injection point of reactant gas.

3) $SiO_2 \cdot Al_2O_3$ ultrafine particle synthesized in the present study showed superior selectivity but at the most equal activity per unit surface area as the commercial catalysts.

4) $SiO_2 \cdot Al_2O_3$ ultrafine particles were also synthesized by spraying isopropanol solution of $CH_3(CH_3O)_3Si$ and $(C_4H_9O)_3Al$ at L = 30 mm into the tail flame of

plasma. Their catalytic activities were intermediate between the $SiO_2 \cdot Al_2O_3$ powders synthesized from gaseous mixture of $SiCl_4$–$AlBr_3$ at L = 60 and 30 mm.

References

1) M. S. J. Gani and R. McPherson, "Glass Formation and Phase in Plasma Prepared Al_2O_3–SiO_2 Powders" J. Mater. Sci., 12, 999 (1977).

2) P. W. McKee, "Catalytic Activity and Sintering of Platinum Black. I. Kinetics of Propane Cracking" J. Phys. Chem., 67, 841 (1963).

3) A. Ueno, H. Suzuki and Y. Kotera, "Particle–size Distribution of Nickel Dispersed on Silica and Its Effect on Hydrogenation of Propionaldehyde" J. C. S. Faraday trans. I, 79, 127 (1983).

CHAPTER 7

GENERAL CONCLUSION

CHAPTER 7

GENERAL CONCLUSION

In this thesis, the syntheses of composite ultrafine particles by laser–induced gas–phase reaction method and plasma method were studied. Silicon carbide – silicon nitride ($SiC–Si_3N_4$) composite ultrafine particles were synthesized by laser–induced gas–phase reaction method and by plasma method and their local structures were studied by ^{29}Si–MAS–NMR and ESR.

$SiC–Si_3N_4$ composite ultrafine particles were synthesized using a CO_2 laser from SiH_4, C_2H_4, and NH_3. $SiC–Si_3N_4$ composite powders with different composition were obtained at various reactant gas flow rate. $SiC–Si_3N_4$ composite particles were not the simple mixture of SiC and Si_3N_4. The β–SiC phase in the particles dissolved a large amount of nitrogen and the Si_3N_4 phase in the composite particles also dissolved carbon. The MAS–NMR results showed that the powder contained the Si configuration of $SiC_{(4-x)/4}N_{x/4}$ or $SiC_{(4-x)/4}N_{x/3}$ with x = 0 to 4 depending on their composition. The proportion of N–rich Si configuration such as SiN_4 and $SiCN_3$ increased stepwise with nitrogen content of the powder. Since SiC and Si_3N_4 strongly exhibit covalent bond nature, it is rather difficult to dissolved each other. The $SiC–Si_3N_4$ composite particles obtained by this research were very unique and such a unique material was obtained probably due to quick heating and quenching process of laser–induced gas–phase reaction method.

$SiC–Si_3N_4$ composite ultrafine particles were also synthesized by R. F. plasma method. In the case of the synthesis of $SiC–Si_3N_4$ particles using low power plasma from chlorosilanes, the powders were the mixture of SiC, Si_3N_4, Si, C, and amorphous phase and the mutual solubility of Si, C, and N was not clearly observed. However, in the case of the synthesis of $SiC–Si_3N_4$ composite particles using high power plasma from monosilane, the mutual solubility of Si, C, and N was observed. SiC phase in the particles dissolved nitrogen and MAS–NMR results showed that there

were various kind of Si configuration (SiC_xN_{4-x}, X = 1 to 4). Even though structure of the composite particles by plasma were not the same as those by laser, such a atomically mixing was probably due to quick heating and quenching process of R. F. plasma.

Silica – alumina ($SiO_2 \cdot Al_2O_3$) composite ultrafine particles were synthesized by plasma method and their catalytic activity was studied as a fundamental study on the application of ultrafine particles. The $SiO_2 \cdot Al_2O_3$ ultrafine particles showed superior selectivity and equal activity per unit surface area as the commercial $SiO_2 \cdot Al_2O_3$ catalysts. The possibility of ultrafine particles catalyst was shown in this research.